Observational Study on Thermal and Non-thermal X-rays from Shell-like Supernova Remnants

OZAKI Masanobu

Contents

1 Introduction **5**

2 Review of SNRs **7**

2.1 Supernova Explosion 7

2.1.1 Type Ia supernova 7

2.1.2 Type II supernova 8

2.2 Shell-like and Crab-like supernova remnants 9

2.3 Radiative processes in shell-like SNR 11

2.3.1 Shock wave 11

2.3.2 Sedov solution 13

2.3.3 Emission from optically-thin thermal plasma 14

2.3.4 Non-thermal emission 15

2.4 Particle acceleration by a pulsar 18

2.4.1 Pair plasma inside the light cylinder 18

2.4.2 Pulsar wind 19

2.5 Origin of Cosmic Rays 19

3 Review of SN1006 **21**

3.1 Historical records 21

3.2 Previous Observation 22

3.3 Previous Interpretations or Models of X-ray emission 25

3.3.1 Non-thermal model 25

3.3.2 Thermal model 26

4 Review of IC 443 **29**

4.1 Previous Observations 29

4.2 Interpretations for hard X-ray emission 31

5 Instruments **33**

5.1 Ginga . . . 33

5.1.1 LAC . . . 35

5.2 ASCA . . . 39

5.2.1 XRT . . . 41

5.2.2 GIS . . . 46

5.2.3 SIS . . . 50

6 SN1006 Study With Ginga **57**

6.1 Observations and Data reduction . . . 57

6.2 Results . . . 59

6.2.1 Lupus Region . . . 59

6.2.2 SN 1006 . . . 62

7 SN1006 Study with ASCA **67**

7.1 Observations . . . 67

7.2 Data Reduction . . . 67

7.2.1 Data Filtering . . . 67

7.2.2 Data Combining . . . 68

7.3 Analysis and Results . . . 70

7.3.1 General property . . . 70

7.3.2 Interior emission . . . 77

7.3.3 Rim emission . . . 82

8 IC443 Study with ASCA **93**

8.1 Observations . . . 93

8.2 Data Reduction . . . 95

8.3 Results . . . 95

8.3.1 General property . . . 95

8.3.2 Hard component . . . 95

8.3.3 Soft component . . . 99

9 Discussion **107**

9.1 SN 1006 . . . 107

9.1.1 Interior emission . . . 107

9.1.2 Power-law emission . . . 110

9.2 IC 443 115
9.2.1 Soft component 115
9.2.2 Hard component 116

10 Conclusions **121**

Acknowledgements **123**

References **125**

Chapter 1

Introduction

Abundances of heavy elements and evolution of thin thermal plasma produced by strong shock in supernova remnants (SNRs) are among the major subjects of interest in current X-ray astronomy. Studies on the metal abundances provide a key for the nucleosynthesis in stellar evolutions and supernova explosions, which are the dominant sources of heavy elements in the universe. The SNR plasma has a longer time scale evolution than any of the laboratory plasma, due to their extremely low density. Therefore, we are able to study a time-sliced plasma data: snapshots of the various stages of the evolution and relaxation of thin thermal plasma.

In addition to these major subjects, another aspect of SNRs would be a possible origin of cosmic ray production and acceleration. For the observational study of the cosmic ray acceleration, electromagnetic radiation from accelerated charged particles would be more useful than the cosmic particle itself, because the latter loses information on the source direction due to the Lorentz force in the magnetized interstellar space of our galaxy.

The electromagnetic radiation from the charged particle has a wide range from radio to gamma rays, with radiation processes such as synchrotron, bremsstrahlung, inverse-Compton scattering and nuclear reactions that produce gamma rays. However, such radiations from SNRs without the pulsar have been scarcely studied, except for the synchrotron emission from electrons of energy below $\sim$GeV.

In the X-ray band, the dominant radiation from supernova remnants is the optically-thin thermal plasma with a temperature of ~ 1 keV. In several remnants, additional components that extend up to ~ 10 keV and are possibly of non-thermal origin have also been detected. However, details of the hard X-rays have not yet been well studied due to the interference from bright thin-thermal X-rays.

A breakthrough was provided by the wide X-ray band imaging spectroscopy with ASCA and

partly by the higher-energy observation with Ginga.

Ginga has a large effective area detector with sensitivity up to 35 keV which enable us to observe the hard components in a higher energy range than expected from the thin thermal plasma, typically less than a few keV in temperature. On the other hand, ASCA has an imaging capability of the spatial resolution of 3–5 arcmin with the highest energy resolution so far, which can distinguish the hard components from the soft thermal emission, both spectroscopically and spatially, in the 0.5–10 keV band.

In this work, we analyzed the data for the two shell-like supernova remnants, SN 1006 and IC 443, observed with these satellites. The former has been reported to exhibit an enigmatic spectrum of a strong power-law continuum coupled with very weak lines, while the latter has been known to have a strong thin thermal emission of center-filled morphology, with possible evidence of additional hard components. This paper is the first to report that the hard components in these SNRs are spatially separated from the thin thermal plasmas: the hard components are confined in shell-like regions, while the plasmas are distributed evenly in the whole SNRs.

Chapter 2

Review of SNRs

2.1 Supernova Explosion

In observation, supernovae (SN) are classified into two types according the absence (Type I) or presence (Type II) of the hydrogen line during the outburst.

Most of type I have the silicon optical emission line, and are sub-classified as type Ia, which is actually one of the major classes of SN. Light curves for all of the SN Ia are very similar to each other, showing a rapid rise to maximum brightness at around $M_B = -18.2 + 5 \log h$ (Cadonau, Sandage and Tammann 1985), where h is the Hubble constant in units of 100 km s^{-1}Mpc^{-1}. SN Ia stay at maximum for only a short time, fading by 3 mag in just 30 days, and after about 50 days, start to decrease less rapidly at a nearly constant rate of 0.015 mag day^{-1}.

SN II are found only in spiral galaxies, preferentially in the spiral arms, where star formations are currently active, and hence, are the sites of massive stars. They comprise an inhomogeneous group showing at least two distinct light curves. One group exhibits a halt or a 'plateau' in the post-maximum phase (SN II-P), producing a nearly constant luminosity between days 30–80; the other exhibits little or no plateau, and its luminostiy declines linearly after the maximum with a rate of 0.05 mag day^{-1} (SN II-L). Generally, SN II show peak magnitudes of about $M_B = -17.5 + 5 \log h$.

2.1.1 Type Ia supernova

The absence of the hydrogen line in SN Ia implies that the progenitor probably has no hydrogen envelope. The current model of SN Ia is assumes the carbon deflagration of an accreting C+O white dwarf: the explosion mechanism is a thermonuclear explosion of the electron-degenerate white dwarf core.

The scenario in which a closed binary system leads to a SN Ia explosion is as follows: a closed

binary system consisting of two intermediate-mass stars ($M < 8M_{\odot}$) evolves to transforms the primary star into a white dwarf composed of carbon and oxygen (a C+O white dwarf), after a mass transfer with Roche-lobe overflow to the secondary star. Then the secondary star evolves, and begins to transfer the hydrogen-rich envelop to the white dwarf.

If the accretion rate is small enough ($\dot{M} <\sim 1 \times 10^{-8} M_{\odot}\mathrm{yr}^{-1}$), most of the accumulated hydrogen is ejected from the white dwarf with a flash produced by the ignition of the hydrogen shell. Since the mass of the white dwarf does not increase, no supernova event occurs. However, in the case of a higher mass transfer than $\sim 3 \times 10^{-6} M_{\odot}\mathrm{yr}^{-1}$, the accreting matter becomes too hot to be accumulated on the white dwarf, and is lost from the system eventually. For the intermediate accretion rate of $1 \times 10^{-8} M_{\odot}\mathrm{yr}^{-1} < \dot{M} < 3 \times 10^{-6} M_{\odot}\mathrm{yr}^{-1}$, accreted hydrogen burns with moderate helium flashes and no significant ejection of hydrogen. Therefore the C+O white dwarf mass increases to the Chandrasekhar limit. When the white dwarf mass becomes $1.4M_{\odot}$ and the central density reaches $\sim 3 \times 10^{9}$ g cm^{-3}, explosive carbon ignition begins at the center of the white dwarf.

Immediately after the ignition, the C+O present in the whole white dwarf burns explosively to iron-peaked elements while releasing large amounts of nuclear energy, under the central temperature of about $\sim 10^{10}$ K. As a result of the large energy release, the boundary between the burned and unburned layers becomes convectively unstable, and the hot internal materials are mixed into the outer layer of fresh carbon. Thus, a carbon-burning front propagates outward on the time scale of convection (carbon deflagration). Since the speed of the deflagration wave is less than the speed of sound, the white dwarf can expand during the propagation of the deflagration wave. Behind the deflagration wave, the materials undergoe explosive nuclear burning of silicon, oxygen, neon and carbon, depending on the peak temperature. In the inner layer, nuclear reactions are rapid enough to synthesize iron-peaked elements, mostly ^{56}Ni. When the deflagration wave arrives at the outer layers, the density it encounters has already decreased due to the expansion of the white dwarf. At such low densities, the peak temperature is not high enough to cause silicon burning, hence only Ca, Ar, S, and Si may be produced. In the outermost layers, the deflagration wave is faded, hence C and O remain unburned. In the standard carbon deflagration model, $0.6M_{\odot}$ of ^{56}Ni is produced with the total explosion energy of 1.3×10^{51} erg. This huge energy causes a total explosion of the whole white dwarf, leaving no compact star inside.

2.1.2 Type II supernova

Sine SN II exhibit prominent hydrogen lines, they may have large hydrogen envelopes before the explosion. SN II are explained by the gravitational collapse of evolved, massive stars. This scenario

was confirmed by the detection of burst of neutrinos from SN 1987A, because a neutrino burst is generated during the collapse of an iron core to a neutron star; the iron core is formed only in a massive, evolved star.

In massive stars, at the end of silicon burning, iron cores of about $1.4M_{\odot}$ are formed in the center surrounded by layers of the ashes of elements from the preceding burning, with the low-density hydrogen envelope as the outermost layer. The mass fraction of helium plus heavier elements to the original mass of the star ranges from 1/4 (at $10M_{\odot}$) to 1/2 (at $50M_{\odot}$).

As the temperature of the iron core increases to $\simeq 10^{10}$ K, endothermic decomposition of ^{56}Fe occurs, since no nuclear energy can be provided from iron. Accordingly, the core can not be self-supporting and starts to collapse gravitationally. During the collapse, electrons increase its density, and are finally squeezed into the nuclei, producing heavier, neutron-rich isotopes and homogeneous neutron matter.

When the central density exceeds the density of the atomic nucleus (2.7×10^{14} g cm^{-3}), roughly half of the core still continues to collapse with supersonic speed, then bounces back to produce an outgoing shock wave. If enough energy is provided to the shock, most of the mass of the star explodes with a kinetic energy near 10^{51} erg. The collapsed core becomes either a neutron star or black hole. As the shock passes through the shells of silicon and oxygen just outside the core, the rising temperature leads to an explosive nuclear fusion; this produces a significant fraction of the heavy elements from silicon to zinc. The shock finally loses energy during propagation in the outer shell, leaving the helium shells unburned. Consequently, the abundances of SN II are largely affected by those of the envelope, which depend on the mass of the progenitor.

2.2 Shell-like and Crab-like supernova remnants

The huge explosive energy of a SN makes a relic for a long time in interstellar space. This is usually found in the radio wavelength and is called as a supernova remnant (SNR).

From their appearance, SNRs can be classified into two types: 'shell-like' and 'prelions'. Examples of the former are Cassiopeia A (Cas A), Cygnus Loop and SN 1006. The prototype of the latter is the Crab nebula, and therefore, prelions are also called a 'Crab-like' SNR.

The energy source of the shell-like SNRs is a shock wave propagating either in the interstellar medium (ISM), circumstellar medium (CSM) or the ejecta. According to the age (or evolutional stage of the shock wave), the shell-like SNR can be divided into three phases: the free expansion, the adiabatic (or 'Sedov') and the radiative phases.

When a supernova explodes, the ejecta expands into ISM or CSM, and forms discontinuity

surfaces, where the shock waves stand in the ISM (CSM) and the ejecta (McKee, 1974), which are designated as forward and reverse shocks, respectively. The reverse shock is propagated inward through the ejecta, but the expansion velocity of the ejecta, which is determined from the Doppler shift of lines, is typically $\sim 10,000$ km s^{-1}, and is still much larger than the sound velocity. Therefore, the shock actually moves outward with respect to fixed coordinates. Accordingly, two nesting shock-wave shells appear, both expanding with time.

Behind the shock front, the temperatures of ions quickly increases depending on the shock velocity. Then the ion energy is transferred to electrons rather slowly until the temperatures of electrons and of the ions are finally equalized. The electron temperature thus becomes high enough to emit X-rays by a bremsstrahlung process, together with emission lines by electron collisional ionization or by excitation of ions.

At the free expansion phase, the mass of the ejecta swept-up by the reverse shock exceeds that of the ISM (CSM) swept-up by the forward shock, hence the emission measure from the ejecta is larger than the ISM (CSM). In this phase, the X-ray spectrum is predominantly due to the emission from the ejected elements.

When the mass of the swept-up interstellar gas becomes larger than that of the ejecta, the SNR enters the adiabatic phase. The radiation energy is much smaller than the total kinetic energy, hence we can regard that the energy of gas (kinetic + thermal) is conserved during this phase or adiabatic expansion. The expansion can thus be described by the theory of adiabatic blast waves (Sedov 1959; Landau and Lifshitz 1959). The radius of the shock front R is

$$R \simeq 13(W_0/10^{51})^{1/5} N_1^{-1/5} t_4^{2/5} \text{ pc}, \tag{2.1}$$

where W_0, N_1, and t_4 are the kinetic energy released in the explosion, the interstellar density, and the time since the explosion in units of 10^4 years, respectively. The velocity of the shock is $v = 2R/5t$ and the temperature behind the shock is

$$T \simeq 8 \times 10^9 (W_0/10^{51})/N_1 R^3 \tag{2.2}$$

(Gorenstein, Harnden and Tucker 1974). This phase lasts until the radiative energy loss becomes large compared to the kinetic energy. This occurs when the radius of the SNR is equal to R_C, given by Cox (1972)

$$R_C \simeq 25(W_0/10^{51} N_1)^{5/17} N_1^{-2/17} \text{ pc}. \tag{2.3}$$

As the shock wave expands in time, due to the increasing mass of the swept-up matter, the shock speed and, consequently, the temperature behind the shock decreases. Thus, radiation is shifted to longer wavelengths in time.

When the SNR radius becomes greater than R_C, the radiation energy is not negligible compared to the kinetic energy: the radiative energy is so large that the pressure behind the shock drops, leading to a decrease in the shock velocity and a compression of the swept gas into a dense, relatively cool (10^4–10^5 K) shell.

In contrast to the shell-like SNRs, Crab-like SNRs are powered by neutron stars. Neutron stars are spinning rapidly, and gradually slowing down by supplying energy to the surrounding nebulae.

The spectra of Crab-like SNRs can be described by a single power-law from radio to X-ray band. Accordingly, all of the radiations are believed to be synchrotron emissions, although details of the particle acceleration mechanism still remain unclear.

2.3 Radiative processes in shell-like SNR

2.3.1 Shock wave

In the coordinates co-moving with the shock front, the shock wave is described by the following differential equations: in the case of the ideal gas, the conservations of mass, momentum and energy flux are described as

$$\frac{\partial \rho}{\partial t} + \frac{\partial}{\partial x}(\rho v) = 0 \tag{2.4}$$

$$\frac{\partial}{\partial t}(\rho v) + \frac{\partial}{\partial x}(P + \rho v^2) = 0 \tag{2.5}$$

$$\frac{\partial}{\partial t}\{\rho(\frac{1}{2}v^2 + E)\} + \frac{\partial}{\partial x}\{Pv + \rho(\frac{1}{2}v^2 + E)v + Q\} = 0 \tag{2.6}$$

where ρ, v, P, E and Q are the density, streaming velocity, pressure, energy per unit mass and heat flux density, respectively. Applying these equations to the upstream and the downstream of the shock wave (figure 2.1), we get

$$\rho_1 v_1 = \rho_2 v_2 \tag{2.7}$$

$$\rho_1 v_1^2 + P_1 = \rho_2 v_2^2 + P_2 \tag{2.8}$$

$$v_1[P_1 + \rho_1(\frac{1}{2}v_1^2 + E_1)] = v_2[P_2 + \rho_2(\frac{1}{2}v_2^2 + E_2)] \tag{2.9}$$

where subscripts 1 and 2 correspond to upstream and downstream, respectively. With Bernoulli's theorem and the notation of the sound velocity, equation (2.9) is further transformed to

$$\frac{1}{2}v_1^2 + \frac{\gamma}{\gamma - 1}\frac{P_1}{\rho_1} = \frac{1}{2}v_2^2 + \frac{\gamma}{\gamma - 1}\frac{P_2}{\rho_2} \tag{2.10}$$

where γ is specific-heat ratio. With equations (2.7), (2.8) and (2.10), we get Rankine-Hugoniot relations,

$$\frac{\rho_2}{\rho_1} = \frac{v_1}{v_2} = \frac{(\gamma - 1)P_1 + (\gamma + 1)P_2}{(\gamma + 1)P_1 + (\gamma - 1)P_2} \tag{2.11}$$

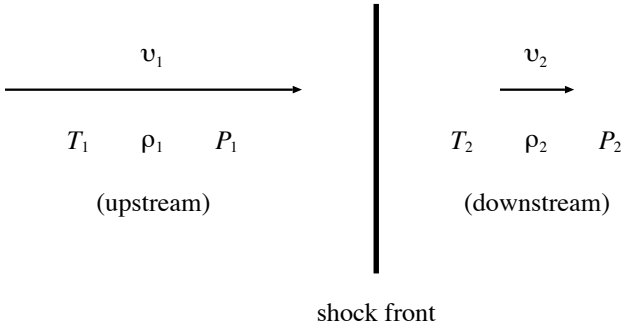

Figure 2.1: Discontinuity at the shock wave

$$\frac{T_1}{T_2} = \frac{a_1^2}{a_2^2} = \frac{P_1}{P_2}\frac{(\gamma-1)P_1+(\gamma+1)P_2}{(\gamma+1)P_1+(\gamma-1)P_2}. \tag{2.12}$$

For the velocities of the gas across the shock front, we have

$$v_1^2 = \frac{1}{2\rho_1}\{(\gamma-1)P_1+(\gamma+1)P_2\} \tag{2.13}$$

$$v_2^2 = \frac{1}{2\rho_1}\frac{\{(\gamma+1)P_1+(\gamma-1)P_2\}^2}{(\gamma-1)P_1+(\gamma+1)P_2}. \tag{2.14}$$

In the extreme case of a strong shock: $P_1 \ll P_2$,

$$\frac{\rho_2}{\rho_1} = \frac{v_1}{v_2} = \frac{\gamma+1}{\gamma-1}. \tag{2.15}$$

Under this condition, the velocities can be written as

$$v_1 = \sqrt{\frac{1}{2}(\gamma+1)\frac{P_2}{\rho_1}} \tag{2.16}$$

$$v_2 = \sqrt{\frac{1}{2}\frac{(\gamma-1)^2 P_2}{(\gamma+1)\rho_1}}. \tag{2.17}$$

In the observer's coordinates where the shock velocity $v_s = v_1$, the post-shock velocity is $v_p \equiv v_1 - v_2$, while the post-shock pressure P_p becomes

$$v_p = \frac{2v_s}{\gamma+1} \tag{2.18}$$

$$P_p = \frac{2\rho_1 v_s^2}{\gamma+1}. \tag{2.19}$$

Using the equation of the state, we get the relation between v_s and the post shock temperature T_p as

$$kT_p = P_p\frac{\mu}{\rho_2} \tag{2.20}$$

$$= \frac{2(\gamma-1)}{(\gamma+1)^2}\mu v_s^2, \tag{2.21}$$

where μ is the mean atomic weight. In the case of the monoatomic gas, $\gamma = 5/3$, so that

$$kT_p = \frac{3}{16}\mu v_s^2. \tag{2.22}$$

2.3.2 Sedov solution

The propagation of the blast wave exited by a supernova explosion can be described as that of the shock induced by a large amount of energy release in a short time at one point, which was induced by Sedov (1959).

If the strong shock: $P_2/P_1 \ll (\gamma+1)/(\gamma-1)$, the evolution of the shock can be described only with the explosion energy E, the pre-shock density ρ_1, the time since the explosion t, and the radius R. A non-dimensional parameter ξ can be defined as

$$\xi = r\left(\frac{\rho_0}{Et^2}\right)^{1/5}, \tag{2.23}$$

then the distance of the shock front from the explosion center is written as

$$R = \xi_0\left(\frac{Et^2}{\rho_1}\right)^{1/5}, \tag{2.24}$$

where ξ_0 can be determined from the equation of the energy conservation (Landau and Lifshitz 1959) and $\xi_0 = 1.17$ for gas with $\gamma = 5/3$.

From equation (2.24), we get the shock velocity as

$$v_s = \frac{dR}{dt} = \frac{2}{5}\xi_0\left(\frac{E}{\rho_1}\right)^{1/5} t^{-3/5}. \tag{2.25}$$

Application to the shell-like SNR

If the ejecta or the ambient ISM (CSM) is exploded at the speed of v_0, we get the initial velocity of the induced shock in the ISM (CSM) as

$$v_s = \frac{\gamma+1}{2}v_0 = \frac{4}{3}v_0 \tag{2.26}$$

from equation (2.18). The last term is attained in case of ideal monoatomic gas. The shock propagates following the equation (2.24) and making the post-shock density $\rho_2 = (\gamma+1)/(\gamma-1)\ \rho_1 = 4\rho_1$. As a result, the shock propagates sweeping matters, whose thickness ΔR and temperature T can be calculated as

$$4\pi R^2 \Delta R\, \rho_2 = \frac{4}{3}\pi R^3 \rho_1 \tag{2.27}$$

$$\longrightarrow \Delta R = \frac{1}{12}R, \tag{2.28}$$

and

$$kT = \frac{3}{16}\mu v_s^2 \propto t^{-6/5}. \tag{2.29}$$

2.3.3 Emission from optically-thin thermal plasma

Electron heating with the shock

Immediately after the shock, ions and electrons are separately heated to high temperatures depending on their mass: the shock gives the velocity of $3/4\,v_s$ to the plasma particle, hence the attainable energy of electron $1/2\,m_e(3/4v_s)^2$ is roughly 2000 times smaller than that of the ion gas $1/2\,m_i(3/4v_s)^2$. Afterwards, the electrons in the post-shock region are gradually heated by the energy transfer from ions. Energy (temperature) transfer rate from ions to electrons, both in the Maxwellian velocity distributions with temperatures of T_i and T_e, respectively, is given as,

$$-\frac{dT_e}{dt} = \frac{T_e - T_i}{\tau_{\rm eq}} \tag{2.30}$$

where $\tau_{\rm eq}$ is the equipartition time constant. If energy is transfered through Coulomb collisions, $\tau_{\rm eq}$ is given by (Spitzer 1962)

$$\tau_{\rm eq} = \frac{3m_e m_i k^{3/2}}{8(2\pi)^{1/2} n_e e^4 \ln\Lambda}\left(\frac{T_i}{m_i} + \frac{T_e}{m_e}\right)^{3/2}\ s, \tag{2.31}$$

where $\ln\Lambda$ is the Coulomb logarithm.

Masai (1994) estimated the equipartition process analytically and found the post-shock temperature T_e to be

$$T_e \approx 0.21(\ln\Lambda)^{2/5}(n_{\rm e}t)^{2/5}T_s^{2/5}\ {\rm K} \tag{2.32}$$

for $t < 0.1t_{\rm s}$, where $t_{\rm s}$ is the equipartition time constant given as

$$t_{\rm s} = \frac{3m_{\rm p}(kT{\rm s})^{3/2}}{8(2\pi)^{1/2}e^4 m_{\rm e}^{1/2} n_{\rm e}\ln\Lambda}. \tag{2.33}$$

Significantly higher temperature of electrons than that of the initial value of $\approx m_e/m_i\ T_s$, are attained at extremely shorter time scale than t_s: $T_e \approx 0.1T_s$ and $0.3T_s$ for $t \approx 10^{-3}t_s$ and $10^{-2}t_s$, respectively.

Nonequilibrium ionization

In case of an optically-thin thermal plasma in collisional ionization equilibrium (CIE), the X-rays are dominated by the line emission if the electron temperature is lower than 10^7 K and $Z \geq Z_\odot$; by contrast, an ionizing plasma (non-quilibrium ionization: NEI) generally keeps strong line emission at higher temperature while CIE plasma shows weaker line emission.

In the NEI, 2γ-decay and free-bound processes, as well as line emission also become important. Ignoring the multiple ionization or the Auger transition, we get the collisional ionization rate

equation for an element with atomic number Z as

$$\frac{dn_z}{dn_e t} = S_{z-1}n_{z-1} - (S_z + \alpha_z)n_z + \alpha_{z+1}n_{z+1}, \tag{2.34}$$

where S_z and α_z represent the rate coefficients for ionization of ion from charge z to $z+1$, and for recombination from ion of charge z to $z-1$, respectively, while n_z and n_e are the number densities of the ions with charge z and the electrons. Starting from low initial ionization states, electrons in the outermost orbit are stripped (ionized) to inner orbits as time passes. Due to electron shielding effects, higher ionization states have deeper effective potentials, hence exhibit higher energy fluorescent lines than those found in lower ionization states. Thus, we can obtain information on the degree of ionization from the line energy. At the ionization parameters larger than $\sim 10^{12} n_e^{-1}$ s, no significant line energy shift from that of CIE is found in the wide range of electron temperatures and atomic numbers (Masai 1994).

Thermal Bremsstrahlung

The continuum emission from optically thin thermal plasma is described by the thermal bremsstrahlung spectrum;

$$\frac{dW}{dV\,dt\,d\nu} = \frac{2^5\pi e^6}{3mc^3}\left(\frac{2\pi}{3km}\right)^{1/2} T^{-1/2} Z^2 n_e n_i e^{-h\nu/kT} \overline{g}_{ff}(T,\nu), \tag{2.35}$$

or also given in CGS units as

$$\varepsilon_\nu^{ff} \equiv \frac{dW}{dV\,dt\,d\nu} = 6.8\times 10^{-38} Z^2 n_e n_i T^{-1/2} e^{-h\nu/kT} \overline{g}_{ff}(T,\nu), \tag{2.36}$$

where $\overline{g}_{ff}(T,\nu)$ is the velocity-averaged Gaunt factor. For energies at $10^{-4} < h\nu/kT < 1$, $\overline{g}_{ff}(T,\nu)$ is in the range 1 to 5. The $\overline{g}_{ff}$ values for high energies at $h\nu/kT \gg 1$ are virtually of no importance, since the spectrum cuts-off at these energies. Thus, we get a reasonable estimate within an error of a few factors, by setting $\overline{g}_{ff}(T,\nu)$ to unity. Thus, the dependence of ε_ν^{ff} on ν is

$$\varepsilon_\nu^{ff} \propto \begin{cases} 1 & (h\nu \le kT) \\ e^{-h\nu/kT} & (h\nu \ge kT); \end{cases} \tag{2.37}$$

Accordingly, the continuum flux is nearly constant to the energy of a given electron temperature.

2.3.4 Non-thermal emission

The radio spectra of shell-like SNRs are generally described by a power-law of spectral energy index $\simeq 0.5$. The power-law shape suggests the existence of the electrons with a power-law distribution. As the acceleration mechanism, the Fermi acceleration in the shock (first-order Fermi acceleration) is widely supported.

Fermi acceleration in a shock wave

Suppose that upstream and downstream velocities of the nonrelativistic shock are, respectively, v_u and v_d, and that a relativistic particle of the kinetic energy E_0 passes along the flow from upstream to downstream and vice versa. A particle scattered back elastically in the downstream changes its energy to $E_{0'}$ from the initial value of E_0 as

$$E_{0'} \simeq \gamma_d^2(1-\beta_d)^2 E_0, \tag{2.38}$$

where $\beta_d \equiv v_d/c$ and $\gamma_d \equiv \sqrt{1-\beta_d^2}$ ($\simeq 1$ if $\beta \ll 1$, i.e. the shock is nonrelativistic). Conversely, the energy change of a particle scattered in the upstream is given with the same notations as

$$E_1 \simeq \gamma_u^2(1+\beta_u)^2 E_{0'} \tag{2.39}$$

$$\simeq (1+2\beta_u)(1-2\beta_d)E_0, \tag{2.40}$$

where the suffixes u and d represent the values in upstream and downstream, respectively. Since $\beta_u > \beta_d$, the particle obtains the energy from the shock fluid during the round-trip between the two regions.

This process can be considered as the adiabatic compression of a particle by two flows: in a moving coordinate where $\beta_u > 0$ and $\beta_d < 0$, we can easily understand this acceleration mechanism. Thus, a nonrelativistic particle also can gain the energy.

In a 3-dimensional case, the velocities of the particles scattered back have various directions, so the mean energy gain is eventually reduced. Bell (1978) showed the mean energy after n round trips is

$$E_n = E_0 \exp\left\{\frac{4}{3}n(\beta_u - \beta_d)\right\}. \tag{2.41}$$

In the Fermi acceleration, the actual scattering mechanism is essential. In the SNR shock, the interstellar magnetic field frozen to the plasma in the downstream is randomized by turbulence, therefore a charged particle is elastically and randomly scattered many times: they do 'random walk'. Accordingly, some fraction of the particles coming from the upstream, for example, may return upstream. In the upstream, the returning particles excite the MHD waves. Thus, the magnetic field in the upstream plasma is bent by the Alfvén wave, hence some particles are scattered back again downstream.

We simply assume that the scatters make particles relax to a nearly isotropic angular distribution (*diffusive* approximation). Then the turbulence and the Alfvén wave make mean particle velocity equal to the stream velocity, so that all the upstream particles come back to the shock. In the downstream, Bell (1978) showed that the escape probability η can be described as

$$\eta = 4\frac{v_d}{v_p}, \tag{2.42}$$

under the assumption that the particles are injected at the shock into the downstream at a constant rate and that the downstream is extending to $\gg v_p/v_d$ times of the mean free path, where v_p is the particle velocity.

Thus, the probability for the particle to make $\geq n$ times round trips is

$$P_n = (1 - 4\beta_d)^n \tag{2.43}$$

in a relativistic case.

Using equations (2.41) and (2.43), we can obtain the differential energy spectrum of the accelerated particles:

$$N(E) \propto \frac{dP_n}{dE_n} \tag{2.44}$$

$$\propto E^{-\frac{\beta_u+2\beta_d}{\beta_u-\beta_d}}. \tag{2.45}$$

For a strong shock in the ideal monoatomic gas, $\beta_d = 1/4\ \beta_u$, we have

$$N(E) \propto E^{-2}. \tag{2.46}$$

Synchrotron emission

The total power per frequency emitted from a moving electron in the magnetic field of strength B is

$$P(\omega) = \frac{\sqrt{3}\, q^3 B \sin\alpha}{2\pi m c^2} F\left(\frac{2mc}{3qB\gamma^2 \sin\alpha}\omega\right), \tag{2.47}$$

where $-q$ and m are the charge and the mass of the electron, respectively, and α is the pitch angle, while $\gamma \equiv 1/\sqrt{1 - v^2/c^2}$ and the function $F(x)$ is

$$F(x) \equiv x \int_x^\infty K_{5/3}(\xi)\, d\xi, \tag{2.48}$$

where $K_{5/3}(\xi)$ is the modified Bessel function. $F(x)$ has a peak at $x = 0.29$, so the synchrotron emission has a peak at

$$\omega = 0.29 \frac{3qB}{2mc}\gamma^2 \sin\alpha. \tag{2.49}$$

For relativistic electrons with a power-law energy distribution function with the form of

$$N(\gamma)d\gamma = C\gamma^{-p}\, d\gamma, \tag{2.50}$$

where C is the constant, the total power per unit frequency is

$$P_{\rm tot}(\omega) = \frac{\sqrt{3}\, q^3 C B \sin\alpha}{2\pi m c^2 (p+1)} \Gamma\left(\frac{p}{4} + \frac{19}{12}\right) \Gamma\left(\frac{p}{4} - \frac{1}{12}\right) \left(\frac{mc\omega}{3qB\sin\alpha}\right)^{-(p-1)/2}. \tag{2.51}$$

In astrophysical cases, it is often assumed that the electron velocity is isotropic and that the magnetic field is randomly oriented. Thus the spectrum averaged over the pitch-angle is convenient:

$$I(E) = \frac{\pi q^2 C h^{s-2}}{\sqrt{3}\, sc} \Gamma\left(\frac{3s+8}{6}\right) \Gamma\left(\frac{3s-2}{6}\right) \left(\frac{3qB}{8mcE}\right)^s \text{ photons sec}^{-1}\text{erg}^{-1}, \tag{2.52}$$

where $s = (p+1)/2$ and h are the photon spectral index and the Planck's constant.

Using equation (2.51) and the value $p = 2$ as shown in (2.46), the energy spectral index of the synchrotron emission from the electrons accelerated in the shock is estimated to be 0.5: a typical value observed from shell-like SNRs in radio wavelength.

2.4 Particle acceleration by a pulsar

The mechanism of particle acceleration by a rotating neutron star (pulsar) can be roughly regarded as two cases. The first is related to a pair (electron-positron) creation plasma inside the light cylinder, where the corotation velocity is smaller than the light velocity, hence the magnetic field line from a neutron star may co-rotate. The other is MHD acceleration outside the light cylinder.

2.4.1 Pair plasma inside the light cylinder

The dipole magnetic field $\boldsymbol{B}$ and vector potential $\boldsymbol{A}$ (in Coulomb and Euler gauges) at a vector position of $\boldsymbol{r}$ from a neutron star with the magnetic moment $\boldsymbol{\mu}$ are given by

$$\boldsymbol{B} = \frac{3(\boldsymbol{r}\cdot\boldsymbol{\mu})\boldsymbol{r} - \boldsymbol{\mu}}{r^5}, \ \boldsymbol{A} = \frac{\boldsymbol{\mu}\times\boldsymbol{r}}{r^3}. \tag{2.53}$$

In the simplest case of a rigidly rotating and perfectly conductive neutron star, the scalar potential is written as

$$\phi = -\frac{(\boldsymbol{\Omega}\times\boldsymbol{r})\cdot\boldsymbol{A}}{c} = \frac{\Omega r \sin\theta\, A_\varphi}{c}, \tag{2.54}$$

where Ω and (r, θ, φ) are the angular velocities of the star and the spherical polar coordinates in reference to the rotation axis, respectively. For an oblique rotator,

$$\phi = \frac{\mu\Omega}{cr}(\sin^2\theta\, \cos\alpha + \sin\theta\cos\theta\sin\varphi\sin\alpha) \tag{2.55}$$

where α is the angle between the magnetic moment and the rotation axis.

Due to the strong electric field thus created, electrons and ions at the surface of the neutron star are strongly accelerated and move along the strong magnetic field line toward the ambient space. Since the magnetic field line is not straight but are curved, the electrons emit gamma rays; high-energy gamma rays are converted to electron-positron pairs. The pairs are then accelerated by the electric field and again radiate curved gamma rays. By repeating this cycle, large numbers of electrons and positrons are created. The particles created on the magnetic-field lines move along the lines out of the light cylinder; these are called the pulsar winds.

2.4.2 Pulsar wind

Although the Crab-like SNRs are believed to be powered by the rotational energy of the central pulsar, there is no consensus on how to link the pulsar to the nebular synchrotron emission, how the energy supplied by pulsar is distributed between the magnetic dipole radiation and a relativistic stellar wind, nor on the composition of elements in the plasma escaping from the pulsar's magnetosphere.

Nevertheless, we can point out three major facts, which have become clear since the discovery of the pulsar in 1968. (1) The energy supplied by a pulsar is converted into nebular synchrotron radiation with an extremely high efficiency of 10%–20%. (2) In the nebula, the pulsar produces a magnetic field far stronger than that expected from a primordial field frozen into the expanding nebular. The pulsar and nebula therefore are strongly coupled hydromagnetically. (3) Equipartition of energy density calculated from the synchrotron radio emission provides the lower limit on the pressure in the nebula which exceeds the interstellar medium by far. Thus, the energy from the pulsar, in any process, is considered to be confined within the nebula, although little observational signature for the confinement mechanisms have been found until recently.

2.5 Origin of Cosmic Rays

Cosmic rays, comprised mainly of relativistic protons and coming from all directions of our universe, were first observed with balloon-borne instruments. The observed proton energies range from $< 10^9$ eV to 10^{20} eV; the presence of the low energy limit is due to interference from the solar wind. The integral energy spectrum extends with a single power-law with the index of about -1.7, to the energy of 10^{15} eV, then steepens (the 'knee') to an index of about -2.1. The energy density of cosmic rays in the Galaxy is known to be about 1 eV cm^{-3}, a value which other components are compared to.

The cosmic-ray flux of electrons is lower than that of protons by about an order of two, and has been observed to the energy of about 10^{12} eV, above which the electron fluxes become lower than the background noise level induced by protons.

The abundances (compositions) of heavy elements in the cosmic rays below 10^{10} eV are larger than that found in Population II, and are similar to those in Population I stars, except for elements such as Li, Be and B. These show larger values than their solar abundances by about an order of 6 and have been considered to be produced by the collision of heavier nuclei in the cosmic rays with those of interstellar gas. With this assumption, we can estimate the mean column density along the path of cosmic rays to be about 4×10^{24} cm^{-2}. The mean lifetime of the cosmic rays,

on the other hand, can be also estimated from the flux of the radioisotope ^{10}Be produced by the same collision, and is found to be about 20 million years. From the lifetime and the mean column density along the pass of a cosmic ray particle, we can estimate the mean density of 0.02 cm^{-3}, which is significantly smaller than the typical value of the galactic plane. This may indicate that cosmic particles spend significant fraction of their lifetime in the region of very ambient medium, such as in the hot bubble, or in the galactic halo.

Due to the Lorentz force generated by interstellar magnetic fields, cosmic rays can not travel straight in the interstellar medium. Therefore, we cannot identify the original position of the cosmic rays from its incoming direction. With the typical magnetic field of $\sim 1\mu$G in the Galactic plane, protons up to 10^{15} eV can be confined in the Galaxy. Above this energy, the Larmor radius of the proton becomes comparable to or larger than the order of the thickness of the Galactic disk, hence protons begin to escape from the Galaxy, and the spectrum slope becomes steeper than that determined for lower energies. Thus, the cosmic rays below the knee are believed to be of Galactic origin.

From the energy density and the mean lifetime of cosmic rays, we can estimate the energy injection rate to cosmic rays. Assuming that the Galactic disk has 30 kpc diameter and 300 pc thickness, the total energy of cosmic rays in the Galaxy is estimated to be 10^{66} eV $\sim 10^{54}$ ergs. Dividing by the mean lifetime, we get the energy injection rate as $\sim 10^{40}$ ergs s^{-1}.

This rate can be compared with the energy released by Galactic supernova explosions. Since the supernova rate in the typical spiral galaxy and explosion energy per one SN are, respectively $\simeq$ 30 years event^{-1} ($\sim 10^9$ s event^{-1}) and $\sim 10^{51}$ ergs, the mean energy generation rate is 10^{42} ergs s^{-1}. Thus, about 1% of the supernova energy is required for the cosmic ray acceleration. The radio synchrotron emission from SNRs, which is radiated from $\sim 10^8$–10^9 eV electrons in $\sim 1\mu$G magnetic field, partly support the idea that cosmic rays are accelerated in the shell of SNR.

Possible mechanism would be the first-order Fermi acceleration in an expanding shock of SNR. Then, the differential energy spectrum of accelerated particles becomes a power-law of number index 2, which is smaller than the observed value 2.7. The difference between the observed value from that expected from Fermi acceleration may result from the possible energy dependency of the rates at which particles escape from the shock acceleration site, and from the energy loss of the particle during propagation in the space.

Thus, it is reasonable to address the SNR as the major source of cosmic rays. Since cosmic rays below 10^{15} eV is of Galactic origin, it can be assumed that SNR can accelerate the cosmic particles to the same energy 10^{15} eV. However, the observational evidence of accelerations to energies more than 10^8–10^9 eV were unavailable until now.

Chapter 3

Review of SN1006

3.1 Historical records

SN 1006 is the remnant of the brightest historical supernova explosion in A.D.1006. Its explosion was recorded throughout the world either as a new star or a 'guest star', from Europe, Egypt, Middle East, China to Japan, in diaries, chronicles and official records. These records were first examined systematically by Goldstein (1965), then supplemented by Goldstein and Yoke (1965). The properties they collected from more than 20 documents are as follows:

1. The supernova appeared in early May 1006, the earliest report on 1 May, in the constellation Lupus. It had been very bright for about $3\frac{1}{2}$ months, and re-appeared after about 7 months.

2. The apparent size of the event, as observed by naked eye of medieval astronomers, was $2\frac{1}{2}$ to 3 times of Venus, where apparent diameter of Venus was generally referred to be $\frac{1}{10}$ that of the sun, or about 3 arcmin. At the maximum, the brightness was equivalent to a quarter of the brightness of the full moon, or was as bright as the moon when a little more than a quarter of the surface is illuminated. The latter is consistent with the comparison to the size of Venus. A quarter-illuminated moon has a magnitude of -8, and at quadrature it is -10. These magnitudes are certainly the largest among the historical supernova.

From the records of Toktaga and Ouyang Haüan cited in Goldstein and Yoke (1965), Minkowski (1966) suggested that the supernova had remained visible for at least another year, and thus ruled out the possibility of a type II event, which declines faster than this light curve. Furthermore, he suggested that the absence of the star between $3\frac{1}{2}$ and about 7 month after the explosion is due to its close vicinity to the sun. At the epoch of the disappearance, the angular separation between the sun and the SN was about 70°. Accordingly, he estimated the magnitude of the supernova was

fainter than $m_v = -4.5$ at +105 days. This gives the upper limit of the maximum brightness of the SN to be $m_v = -8$.

Using this value of $m_v = -8$, the average type I supernova maximum brightness of $M_v = 19.^{\rm m}0$ (Minkowski 1963), interstellar absorption of $0.^{\rm m}4$ (Sharov 1964) and the 11 cm radio image of the remnant (Gardner and Milne 1965), he estimated the distance and the linear radius of SN 1006 to be 1300 pc and 7.5 pc, respectively. The radius and the age of 960 yr (in 1965) give an average expansion velocity of 7600 km s^{-1}, which is not much less than that of Tycho's supernova, another type I SN candidate based on its light curve (Baade 1943). Thus, he reached the conclusion that SN 1006 was a type I supernova.

3.2 Previous Observation

SN 1006 (G327.6+14.6, PKS 1459–41) was firstly cataloged by Bolton, Gardner and Mackey (1964) as a radio source 1459–41. Following the suggestion by Goldstein (1965), Gardner and Milne (1965) regarded the remnant of SN 1006 as the radio source. They made an 11 cm image, revealing the shell-like structure. They also showed that the linear polarization and spectral index from each intensity maxima, respectively, exceeds 10% and $\alpha \sim 0.6$; the latter value is obtained from comparison with the results of Bolton, Gardner and Mackey at 75 cm and Mills, Slee and Hill (1960) at 350 cm. Most of the single-dish works at frequencies from 408 to 5000 MHz are summarized by Milne (1971).

Recently, high-resolution images in various radio wavelengths have accumulated. Reynolds and Gilmore (1986) gave 1370 and 1665 MHz images of $16'' \times 20''$ resolution with the Very Large Array (VLA). Two bright regions with extremely sharp outer edges dominate the total flux, while the fainter emission appears to be dispersed in the interior of the SNR. Several discrete filaments, unresolved in width, can be found near the outer diameter of the remnant diameter; one near the remnant edge with almost a perfect quarter circle. The properties of the filaments are consistent with them being sheets seen edge-on, with widths on the order 1 pc and thickness less than 0.1 pc.

Roger et al. (1988) obtained 843 MHz image of $44'' \times 66''$ resolution with the Molonglo Observatory Synthesis Telescope (MOST). Similarly, the image shows a high degree of bilateral symmetry, both in intensity and in the shape of outer boundary. Near the symmetry axis, the flux is weak with no distinct boundaries.

Reynolds and Gilmore (1993), on the other hand, obtained the 1370 and 1665 MHz polarization images of $24''$ resolution with VLA. The gross morphology of the polarized intensity is "bipolar," similar to that the total (unpolarized+ polarized) intensity: two bright limbs nearly parallel to each

other. The SE quadrant, although is the faintest region in the total intensity, exhibits significant polarized flux, while the NE quadrant, which is fairly bright in total intensity, shows no significant polarization. The integrated polarized fraction (measured polarized flux divided by total flux, taken from published single-dish observations) was about 13%. However, the ratios exceed 30% locally. By combining their observations with the previous observations, they inferred an intrinsic polarization position angle to be ordered with the magnetic field being primarily radial, as is the case of the other historical shell remnants.

Moffeit, Goss and Reynolds (1993) measured the expansion velocity of the radio shell at 1370 and 1665 MHz, and compared these images with those reconstructed from observations made in 1983–1984 by Reynolds and Gilmore (1986). They calculated the mean expansion velocity at this epoch to be 3.5 ± 1 arcsec: the expansion rate to be 0.049% yr^{-1} or $R \propto t^{0.48\pm0.13}$, consistent with the Sedov expansion, or with a forward/reverse shock pair moving into constant-density material.

In the optical wavelength, an Hα filament was detected by van den Bergh (1976) at the northwest edge of the remnant. Subsequent spectral observations by Schweizer and Lasker (1978) and Lasker (1981) revealed only the existence of the Balmer-line. Kirshner, Winkler and Chevalier (1987) discovered a broad component to the Balmer-line and inferred shock velocities in the range 2800–3900 km s^{-1} using the non-radiative shock models of Chevalier, Kirshner and Raymond (1980). Long, Blair and van den Bergh (1988) observed the filament, and by comparing it with the image taken by van den Bergh (1976), inferred the mean proper motion of the filament to be 0.30 ± 0.04 arcsec yr^{-1}. Comparing this value with the shock velocity inferred by Kirshner, Winkler and Chevalier, they calculated the distance to SN 1006 to be 1.7–3.1 pc. Therefore, the maximum visual magnitude is estimated to be between -6 and -9.5.

In the UV band, Wu et al. (1983) observed a sdOB star that had been found by Schweizer and Middleditch (1980) in the projected direction near the remnant center. They discovered strong Fe^{+} resonance absorption lines with zero radial velocity, but are broadened by ~ 5–6×10^3 km s^{-1}. These observations suggest that the bulk of the ejecta is iron, in agreement with the type Ia supernovae scenario. They also discovered redshifted $Si^{+,+2,+3}$ lines, which indicates that the star is located behind, hence not physically associated to the SNR.

From the optical filament, Raymond, Blair and Long (1995) discovered HI, HeII, CIV and OVI with the Hopkins ultraviolet telescope during the Astro-2 space shuttle mission. The found that the line widths are consistent with the ~ 2300 km s^{-1} width reported for Hα, implying that the velocities of different ions are separately randomized in the shock and that ion temperature equilibration is not efficient. The faint continuum in the spectrum is consistent with relatively strong dust-scattered starlight along the line of sight. They also suggested that the line intensity

ratios are, within the ambiguity of a factor of 2, consistent with those of model predictions for a 2300 km s^{-1} shock with cosmic abundance gas, with 50% neutral gas ahead the shock.

In the X-ray band, Palmieri et al. (1972) first scanned the Lupus Loop including SN 1006 with a rocket-borne proportional counter of a 2.°62 FWHM collimator and of the 0.2–1.6 keV energy range. They detected an extended emission over about 8° with a peak at the position of SN 1006.

The X-ray image of SN 1006 was first obtained by Pye et al. (1981) with the IPC on the *Einstein* observatory. The image, with resolution of ~ 1 arcmin, shows a limb brightened circular nebula of $\simeq 15$ arcmin radius. The enhanced limb emissions found in the two quadrants are similar to the radio images.

The shell-like structure of the radio and the soft X-ray images of SN 1006, which is similar to those of Cas A, Tycho and Kepler, suggests that the bulk of the X-rays is attributable to a shock-heated plasma. However, the X-ray spectrum of SN 1006 shows a featureless structure over a wide energy band. Thus, SN1006 has been regarded as an enigma in the X-ray astronomy. In fact, Becker et al. (1980) observed SN 1006 with the SSS on the *Einstein* observatory and the CXS (cosmic X-ray spectrometer) on *OSO 8*, and suggested that the X-ray emission is of non-thermal origin, since X-ray emission lines are absent, and the X-ray spectrum could be appropriately represented by a single power-law with a photon index of 2.2, a similar value to those of well established synchrotron nebulae such as Crab and Vela X.

However, some pieces of information suggesting that X-rays are of thermal origin have been accumulating. Vartanian, Lum and Ku (1985), using an instrument with an improved energy resolution, detected K-emission lines from highly ionized oxygen atoms (O VII and O VIII) , which is direct evidence for a thermal X-ray emission. Using Tenma-data, Koyama et al. (1987) reported that after careful subtraction of the local background from the Lupus region, the spectral slope of the hard X-ray band was steeper than that of typical synchrotron nebula. Combining the Tenma and SSS data, Hughes (1991) demonstrated that the wide-band X-ray spectrum favors a thermal spectrum rather than a non-thermal power-law model. Soon after, Leahy, Nousek and Hamilton (1991) reanalyzed the scanning data of the *HEAO-A2* LED (Low Energy Detector) instrument, and concluded that the low-energy X-ray spectrum can be explained by a two-temperature thermal plasma model. If the X-ray emission is of thermal origin, regardless of whether it is multi-temperature or not, a critical problem is the lack of any prominent lines other than that from oxygen.

An important issue for the X-ray data analysis is an accurate determination of the local background from the Lupus Loop overlapping SN 1006. In fact, Koyama et al. (1987) have already reported an excess of diffuse hard X-rays from this region, which is described with either a power-law with a photon index of 2.2 or a thermal bremsstrahlung of $kT = 7$ keV temperature. Since

the local background is diffuse and would not be spatially uniform, X-ray observations in a smaller field of view, together with a high sensitivity to the low surface-brightness features is essential for deriving reliable data for SN 1006.

The Lupus Loop is a very old supernova remnant of about $270'$ radius (Milne 1971). It has been observed in the X-ray and radio regions (Palmieri et al. 1972; Davelaar et al. 1979; Winkler et al. 1979; Toor 1980; Koyama et al. 1987; Leahy, Nousek and Hamiltont 1991). From radio (Clark and Caswell 1976) and soft X-ray observations (Leahy, Nousek and Hamiltont 1991), the age and distance are estimated to be about 10^4 yr and about 500–1000 pc, respectively.

Since the surface brightness of the Lupus Loop is rather low and the previous observations had limited the statistical accuracy, the reported temperature of the plasma are largely scattered over the wide range of 60–1600 eV. In the hard X-ray band, Koyama et al. (1987) discovered an excess emission near the Lupus region. The spectrum is described by a 7.5 keV thermal bremsstrahlung model, which is considerably higher than that of the pervious soft X-ray spectrum. Although it shows no prominent iron K-shell emission line, the plasma temperature resembles that of the Galactic Ridge (Koyama 1989). However, since the galactic latitude of the Lupus Loop is much larger than the scale height of the Galactic Ridge, it is still unclear whether the hard X-ray excess is really associated with the Lupus Loop, to a larger extended galactic ridge emission, or to other sources.

3.3 Previous Interpretations or Models of X-ray emission

As described above, SN 1006 exhibits apparent inconsistency between the image and the X-ray spectrum. Some scientists have tried to explain the inconsistency: their ideas fall roughly into two categories, depending on the assumption of whether the spectrum is thermal or non-thermal. The X-ray energy index generally used in any models is $\simeq 2.2$, based on rather old observations.

3.3.1 Non-thermal model

Reynolds and Chevalier (1981) developed a self-consistent model for non-thermal radiation from supernova remnants in the Sedov phase, assuming that the shock accelerates electrons to an energy density proportional to the postshock pressure.

They assumed that an isotropic power-law electron distribution is created at the shock:

$$N(E)dE = KE^{-s}dE, \ (m_e c^2 \leq E \leq E_{\max}) \tag{3.1}$$

with the additional assumption that the accelerated electrons remain in the thermal gas, or no diffusion, but with no discussion for the detailed acceleration mechanism. For a given element of

gas, K evolves behind the shock as a result of adiabatic expansion; it is proportional to $\rho^{(s+2)/3}$, where ρ is the gas density given by the Sedov solution. They set the synchrotron emissivity to zero within the radius of the reverse shock, at which the Sedov extrapolation would have given an initial expansion velocity greater than 10,000 km s^{-1}, appropriate for a type Ia explosion. For the evolution of the postshock magnetic field, they considered two cases: one where the field is swept up and compressed the interstellar field, and the other where the fields is turbulently amplified to the field energy density of a fixed fraction of the postshock energy. The former, however, was eliminated on the basis of X-ray data.

The upper limit of $E_{\max}$ is determined by the assuming no diffusion, while the lower limit comes from the requirement that the acceleration time should be less than or on the order of the radiative lifetime.

Since the amount of energy gain after a round-trip depends only on the initial energy and the shock velocity, the acceleration time scale is proportional to the mean round-trip path, or the mean free path. Therefore, the lower limit of the acceleration rate is determined by the assumption that the mean free path is short enough to keep the electrons in the thermal gas. Accordingly, $E_{\max}$ is limited since the synchrotron radiative lifetime is proportional to E^{-1}.

They explained the X-ray power-law continuum of energy spectral index $\simeq 1.15$ shown by Toor (1980) and Becker et al. (1980) as the extension of the radio emission, steepened by synchrotron radiative losses; the photon index of the spectrum of a continuously injected power-law electrons increase by 0.5 above a critical energy. While their model do not fully satisfy this category, they regarded the difference as minor. In order to fit the X-ray flux, the break frequency at $\sim 10^{14}$ Hz was required, hence the model required a high post-shock magnetic field on the order of 100μG. Under this magnetic field,electrons with $\gamma \sim 10^8$ (5×10^{13} eV) emit the X-ray photons.

At frequencies where the energy losses become important, emission is confined to a thin shell behind the shock containing the most recently accelerated electrons. Therefore, the radius of X-ray shell becomes larger than that of the radio. They could not, however, find any signature of this kind. The resolution of the radio map would not have been sufficient to support a firm conclusion.

3.3.2 Thermal model

Hamilton, Sarazin and Szymkowiak (1986) tried to create the observed X-ray spectra from a combination of thermal emissions from the ejecta swept up by the reverse shock and that from ISM (CSM) with cosmic abundance swept up by the forward shock. They argued that the power-law continuum and the absence of line emission are consistent with the spectrum of a reverse shock into the ejecta with a roughly uniform density and stratified layered structure of heavy elements.

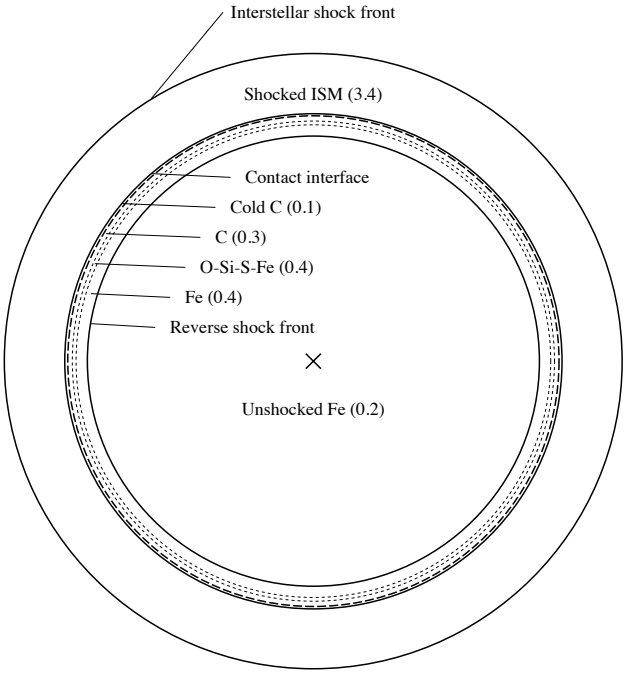

Figure 3.1: The onion-skin structure model of SN 1006 by Hamilton, Sarazin and Szymkowiak (1986). Numbers in brackets are masses in $M_{\odot}$.

They obtained a satisfactory fit to the published X-ray spectra with a three-layer model of ejecta consisting of an outer layer of pure carbon, a middle layer of processed heavy elements, oxygen, silicon, sulfur and iron, and an inner layer of pure iron. The free-free emission from fully ionized gas in the dense outer layers of the ejecta can produce a power-law continuum.

To explain the power-law continuum, they obtained the following equation, assuming that the electron pressure in the remnant is constant, a power-law distribution of mass with temperature:

$$\frac{dM}{d\ln T_e} = \beta M_{tot} \left[\frac{T_e}{T_e(\max)}\right]^{\beta}, \tag{3.2}$$

with $\beta \approx 0.3$ in the hydrogen and helium dominant plasma, or $\beta \approx 0.5$ in the fully ionized carbon or oxygen plasma. Equation (3.2) assumes that β is positive and $T_e(\min) \ll T_e(\max)$.

The power-law distribution cannot be made by Sedov (1959) solution nor by individual components, the blast wave or reverse shock, in Chevalier's (1982) similarity solutions. To make this power-law distribution, they adopted the early time reverse shock similarity solution for uniform density ejecta moving into an external medium (Hamilton and Sarazin 1984). Furthermore, to explain the weak oxygen K-line emission, they restricted the oxygen to the dense outer layers of ejecta, where the low energy X-rays are emitted.

Figure 3.1 is a the schematic illustration of the structure of the best-fit model, and table 3.1 gives the strengths of selected line features.

Table 3.1: Line strengths predicted by Hamilton, Sarazin and Szymkowiak (1986) model.

Line	Flux [photons $cm^{-2}s^{-1}$]	Equivalent width [eV]
C Lyα	0.1–0.2	—
O K-line	0.1	—
Si and S L-lines	0.1–0.2	—
Si K-line	3×10^{-4}	40
S K-line	2×10^{-4}	50
Fe K-line	5×10^{-5}	150

The spectrum is dominated by the reverse shock at low energies, and by the interstellar blast wave at high energies. In the dense outer layer of the ejecta, carbon is fully ionized and produces the soft X-ray continuum and strong carbon Lyman lines. The middle layer produces line emission from heavier elements, O, Si, S and Fe. The low-density inner layer of iron produces negligible emission. This innermost layer is included in the model, in order to argue that a large amount of iron can be hidden without difficulty inside the ejecta components. The equivalent widths of Si, S and Fe K-lines are 40, 50 and 150 eV, respectively, and are consistent with the observations they cited.

Chapter 4

Review of IC 443

IC 443 (G189.1+3.0, 3C157) is a shell-like SNR of about 45 arcmin diameter. The flux density at 1 GHz is 160 Jy and the radio spectral energy index from 20 MHz to 11 GHz is 0.36 (Erickson and Mahoney 1985).

While the association of supernova progenitors and their parent molecular clouds is expected, SNRs that show a clear-cut interaction of molecular cloud and blast wave are apparently rare. IC 443 is an unique SNRs where the interaction between the shock wave and the molecular cloud is distinguished by the presence of clearly identifiable highly perturbed regions of molecular gas.

4.1 Previous Observations

DeNoyer (1979a,b) discovered three shocked OH and CO clumps with pointing observations where bright condensations of the shocked HI have previously been seen (DeNoyer 1978), and suggested the existence of clumpy structures named A, B and C. The CO associates with the accelerated HI and OH clouds, and its lines have velocity width of 20 km s^{-1} and appeared to be optically thin.

To determine the overall structure of IC 443 in radio and IR wavebands, Braun and Strom (1986) analyzed the IRAS all sky survey data of 12, 25, 60 and 100μm bands, and 327 and 1400 MHz and λ21 cm HI line radio data. They argued that the SNR shock has encountered a pre-existing high-density shell.

With the radio data, they showed that IC 443 consists of three interconnected $\sim$ spherical subshells of vastly different radii and centroids. The first two together define the usually assumed boundaries of IC 443, while the third includes the optical filaments which extend beyond the bright north-eastern rim. They showed that these filaments have well correlated non-thermal radio counterparts. They found that the spectral index ($S \propto \nu^{-\alpha}$) for the bright north-eastern rim is $\alpha = 0.35 \pm 0.03$, while that for the external filaments are $\alpha = 0.42 \pm 0.09$. These are in good

agreement with the value found by Erickson and Mahoney (1985) from integrated fluxes between 20 MHz and 11 GHz, $\alpha = 0.355 \pm 0.013$.

From the λ21 cm data, they showed that the emission of negative velocities is dominated by an incomplete semi-circular arc which is coincident with radio continuum filaments in the east-central portion of the SNR, and that the emissions of positive velocities are found at the bright north-eastern rim, and as extended emissions in the south and south-east, and as long nearly linear features from the north-east to south.

From the IRAS data, they extracted cool and warm dust emission images assuming that the data represent a linear combination of cool dust, zodiacal light and warm dust emission. The cool emission reveals a shell-like image, while the warm emission shows more clumpy, centrally concentrated structure. They argued that the cool dust distribution suggests an outer skeleton which has been consumed from within by the action of the massive stars of the Gem OB1 association, and showed that the warm peak coincides with the O9 Vp star HD256035 which is likely to be responsible for local heating and ionization. The brightest infrared emission regions have best spatial correlation with the shocked HI emission from the northeast and the molecular cloud.

Mufson et al. (1986) argued that the expansion of an initially symmetric SNR blast wave into an inhomogeneous ambient medium is sufficient for explaining the HI, IR, visible and X-ray morphology of the IC 443.

Dwek et al. (1987) also analyzed the IRAS data and estimated the IRAS band luminosity to be 360 times the X-ray luminosity. They argued that approximately half of the infrared emission arises as thermal emission from shock-heated dust assuming a normal gas-to-gas ratio.

From the shocked clumps, other lines such as ^{13}CO and HCO^+ have been detected. Dickman et al. (1992) carried out systematic, high-resolution $J = 1 \rightarrow 0$ CO and HCO^+ mapping observations over the entire region of IC 443. They found five new clumps of perturbed molecular gas and clarified their relations: together with the previous three clumps, the clumps outline a roughly elliptical ring whose major axis is ~ 9 pc across assuming the generally accepted distance of 1500 pc for IC 443. They showed a systematic variation in the distribution of the high-velocity molecular gas associated with the clumps: the southern part of the gas is blue-shifted and the northern is red, which is the same trend observed in the λ21 cm image (Braun and Strom 1986). This suggests that the clumps are distributed along the periphery of a tilted, expanding ring. They argued that the ring is a byproduct of the blast wave's interaction with a more homogeneous confining structure.

Various simple molecules in the shocked molecular gas were observed by van Dishoeck, Jansen and Phillips (1993). From CO 3–2 line profiles, they found that in the S–SE part of the ring (clumps A–C) the shock occurs mostly along the line of sight, whereas in the NE–NW part, the shock is

mostly perpendicular (clumps D, E, G).

In the soft X-ray band, Petre et al. (1988) analyzed IPC, HRI and SSS of the *Einstein* observatory, and ME of *HEAO-1* A-2 data. They found that there is little correlation between soft X-ray and optical or radio features, which is highly atypical for a supernova remnant in the adiabatic phase. The best-fit models of the low-energy X-ray spectrum of the brightest area suggested either that the remnant has not yet attained ionization equilibrium or that the X-rays arise in a multi-phase medium. They found that the X-ray hardness ratio map with IPC is well correlated with the surface brightness distribution of the CO line emission from a molecular cloud in the line of sight (Cornett et al. 1977), and suggested that the spatial structure of the X-ray absorption is globally explained by the molecular cloud.

Wang et al. (1992) observed IC 443 with *Ginga* satellite and found that the flux below 6 keV is consistent with *Einstein* and *HEAO-1*, and the spectrum is smoothly extended to 20 keV. The extension could be fitted with a power-law with an energy index of about one. They also found the iron K emission equivalent width to be about 0.25 keV.

Asaoka and Aschenbach (1994) analyzed ROSAT all-sky survey and pointing data, and found another overlapping SNR of $\sim 10^5$ yr, which they called G 189.6+3.3. They suggested that the high-energy X-rays (> 2 keV) are emitted only from the two smaller shells (IC 443), but not from the large shell of G 189.6+3.3. From the spatially resolved spectroscopy of a ROSAT pointing observation, they suggested that G 189.6+3.3 and IC 443 are separated along the line of sight by the CO molecular cloud, and only the IC 443 spectrum is affected by low energy X-ray absorption in the molecular cloud. They also suggested that the lane-like structure of reduced X-ray surface brightness across IC 443 is due to absorption of the background X-rays from IC 443 by a dense shell of cold matter associated with the G 189.6+3.3 lying in front.

In the gamma-ray band, Esposito et al. (1996) studied the data from the EGRET instrument aboard the *Compton Gamma Ray Observatory*. The gamma-ray flux, $E > 100$ MeV, from 2EG J0618+2234, which coincides with IC 443, is $(5.0 \pm 0.4) \times 10^{-7}$ photons cm^{-2}s^{-1}, and the spectrum can be fit by a single power-law with a photon index of 1.97 ± 0.07. They showed that shock acceleration of cosmic rays gives consistent results with the data although the pulsar origin cannot be precluded, and that SNRs are possibly the origin of Galactic cosmic rays.

4.2 Interpretations for hard X-ray emission

For the origin of the hard tail observed with *Ginga*, Wang et al. (1992) discussed several possibilities: a shock-heated plasma, and other 3 possibilities of non-thermal origins, containing synchrotron

radiation, inverse Compton scattering and bremsstrahlung.

Here we quickly review their discussion. Assuming a synchrotron origin, the break frequency determined from extrapolations of the spectra of both the radio and X-ray becomes $\sim$ 100 GHz. The half-life of the electrons having the peak synchrotron emission at this break frequency should therefore be shorter than the age of the SNR, probably shorter than 10^4 yr. Since the half-life is inversely proportional to the electron energy, a half-life of X-ray emitting electrons is therefore shorter than one year. Such an efficient mechanism of acceleration is unlikely. In the case of inverse Compton X-rays, the strong IR emission of a photon density comparable to that of the cosmic microwave background would be attributable to the inverse Compton X-rays. Since the energy index of the spectrum of the Compton scattered X-rays is the same as that of the synchrotron radio emission, the same electrons cannot be responsible for both X-rays and radio emissions. In addition, the hard X-ray flux is consistent with the radio flux, only when the magnetic field strength is weaker than 10^{-6} G, significantly weaker than the average of the galactic magnetic field. Such a weak magnetic field is unlikely.

If the mechanism is the bremsstrahlung from non-thermal electrons, the X-ray emitting electron is non-relativistic, hence the electron energy is lower than that of the radio emitting (synchrotron) electrons. The observed X-ray and radio spectral index can be explained by the electrons with a single spectral index. However, since both electrons and the magnetic field are responsible for the radio synchrotron, either the electrons must have unreasonably high density, or the magnetic field must be unreasonably weak to explain both X-ray and radio flux.

Wang et al. (1992) thus suggested that a shock-heated plasma is most likely origin, and that the other 3 non-thermal origins are unlikely. In fact, after subtracting the soft component obtained by Petre et al. (1988), they got an acceptable fit to the hard component with temperature higher than 8 keV. To explain the low equivalent width of the iron K line, they proposed a low ionization time $n_{\rm e}t$ for the plasma.

Such a high temperature for the hard component requires a shock velocity of 2500–3500 km s^{-1}, which results in the crossing time for the shock wave over the radius of IC 443 to be in the range of 1000-1400 yr. If the emission comes from about $\frac{2}{3}$ of the SNR, the hard X-ray flux and $n_{\rm e}t$ required for the iron equivalent width become consistent. Thus, they suggested that the age of IC 443 is $\sim$ 1000 yr instead of the previous estimation of 10^4 yr, and that IC 443 is the remnant of a supernova in A.D.837.

Chapter 5

Instruments

5.1 Ginga

Ginga is the third Japanese X-ray observation satellite which was launched by the M–3SII–3 rocket from Kagoshima Space Center (KSC) on 5 February 1987. It was thrown into a slightly elliptical orbit with the perigee of 520 km, the apogee of 670 km and the orbital inclination of 31°. The orbital period is 96 min, that is, 15 revolutions a day. The argument of perigee rotates in the orbital plane with a period of 37 days. It weighted 430 kg and consisted of 1000 mm×1000 mm×1550 mm body and four 760 mm×1755 mm solar paddles.

Ginga could contact KSC only for about 10 minutes each in 5 (or 6) consecutive orbits out of the 15. These orbits are usually called "contact orbits", and the other ten, "remote orbits".

Ginga had three instruments; the large area proportional counter (LAC; Turner et al. 1989), the al sky monitor (ASM; Tsunemi et al. 1989) and the gamma-ray burst detector (GBD; Murakami et al. 1989). Figure 5.1 shows the configuration of these three instruments.

For the satellite attitude control system, *Ginga* had five different attitude sensors; (i) star trackers (STT) which are CCD cameras and detect the position of stars with > 6 mag., (ii) non-spin type solar aspect sensor (NSAS) with accuracy of $\simeq 3$ arcmin, (iii) spin type solar aspect sensor (SSAS), (iv) inertial reference units (IRU) which detect the angular velocity around the X, Y, Z and S-axes which was arranged to form a 54.7° angle to other three axes and (v) geomagnetic aspect sensor (GAS). The attitude was controlled in reference to four IRUs to an accuracy of $\sim 0.1°$.

For maneuvering and stabilizing the attitude, *Ginga* had one momentum wheel (MW) to control around the satellite Z-axis slew, and three magnetic torquers (MTQ) to maneuver the Z-axis direction, as well as to release the accumulated extra momenta in the satellite body to the space maneuver. Figure 5.2 shows the definition of the satellite coordinates. The speed of the slew and the maneuver was $14°\text{min}^{-1}$ and $5°\text{min}^{-1}$; therefore, maneuverability around the Z-axis is about 170

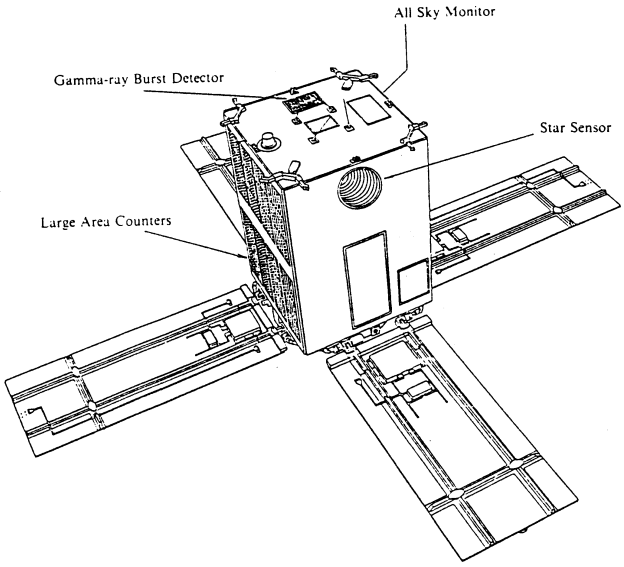

Figure 5.1: Instruments configuration of the Ginga satellite.

times more efficient than that around the X and Y-axes. The satellite attitude is perturbed by the forces due to air between the earth atmospheric air drag, the solar light pressure and gravitational torque. The IRU attitude controller can compensate for these small perturbations instantaneously.

If the angle between the sun and the Z-axis becomes small, the solar light on the solar paddles is reduced significantly, hence the satellite lacks the power to operate. The attitude operations are therefore limited within the solar angle of $> 140°$. For emergency when the solar angle accidentally becomes $< 135°$, the satellite was programmed to enter the power-save mode, and to move back to the attitude of the largest solar angle.

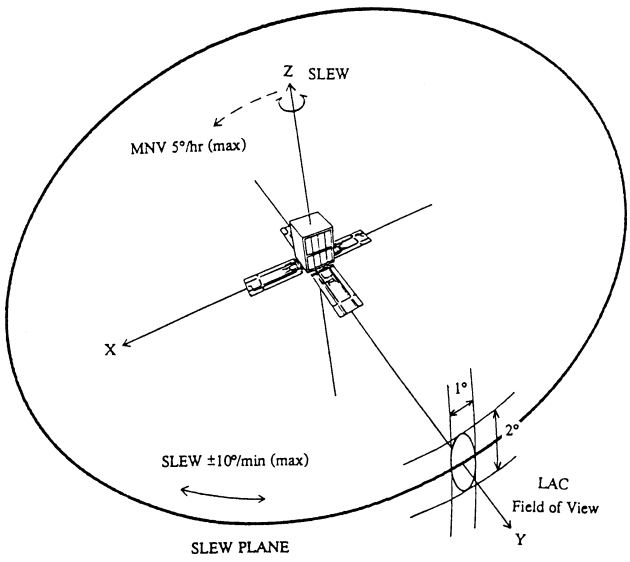

Figure 5.2: The definition of the Ginga satellite coordinates.

In addition to the ordinary pointing mode, the scanning mode was also available using the high-speed maneuverability around the Z-axis, hence rotating the field of view of LAC along a great circle. The scanning mode was generally used: (i) to determine the source position precisely, (ii) to examine whether or not any contamination sources exist near the target of a pointing mode and (iii) to survey a wide sky region, either for the observation of surface brightness distribution of an extended source or that of the diffuse background near the target.

The final attitude of the satellite and the aspect of the LAC were reconstructed on the ground using the IRUs and STTs data within a typical accuracy of $\sim 0.02°$.

As the telemeter channel, *Ginga* used U-band (down-link 400 MHz) and S-band (up-link 2.1 GHz, down-link 2.3 GHz). On the contact path, the satellite transmits the stored and real-time data in S-band and U-band, respectively. The control commands are sent to the satellite in U-band. At the same time, the orbital elements of the satellite were obtained with the Doppler shift and loop-back time of the S-band signal. The daily operations were planned using thus accumulated orbital parameters.

The data are divided into three groups: scientific data from LAC, ASM and GBD, house keeping data such as battery condition and charged particle monitor, and data of the satellite attitude information. These data were processed by on-board processor (DP), then stored in the bubble data recorder (BDR) of 41.9 Mbits capacity when the satellite was out of contact, or transmitted to the ground station during the contact path.

Since the interval between contacts was variable depending on the phase of orbital cycle, and since the BDR capacity was limited, *Ginga* had three data processing bit rate, High, Med and Low. The recording time and time resolution depended on the bit rate. Each rate could record for 40 min, $5\frac{1}{2}$ and 23 hr with 16K, 2K and 512 bits s^{-1}, respectively. Therefore, bit-low was used in the remote passes and bit-med and -high were in the contact passes.

5.1.1 LAC

LAC consists of 8 proportional counters equipped with collimator blocks (figure 5.3) and a front-end electronics (LAC-S). All signals are fed into a signal processing part called LAC-E.

The collimator has semi-honeycomb structure shown in figure 5.4. It has the peak transmissivity of about 82% with a field of view of about 1° and 2° in X- and Z direction, respectively.

The counter is made of stainless steel with a thickness of 0.7 mm, and intercepts X-rays up to ~ 50 keV and electrons up to ~ 1 MeV. The gas chamber is divided into 4 layers, each consisting of 13 multi-cell structure, with a center wire for an anode wire. Multiple ground wires electrically separate these layers and cells. These wires are also made of stainless steel with diameters of 40μm

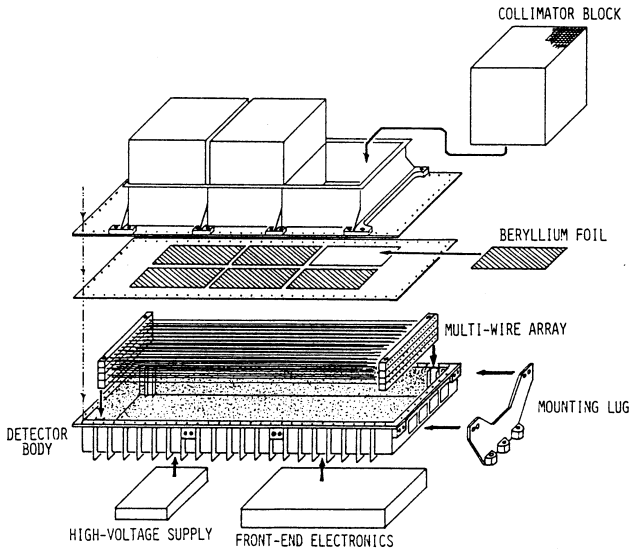

Figure 5.3: The schematic figure of the Ginga LAC.

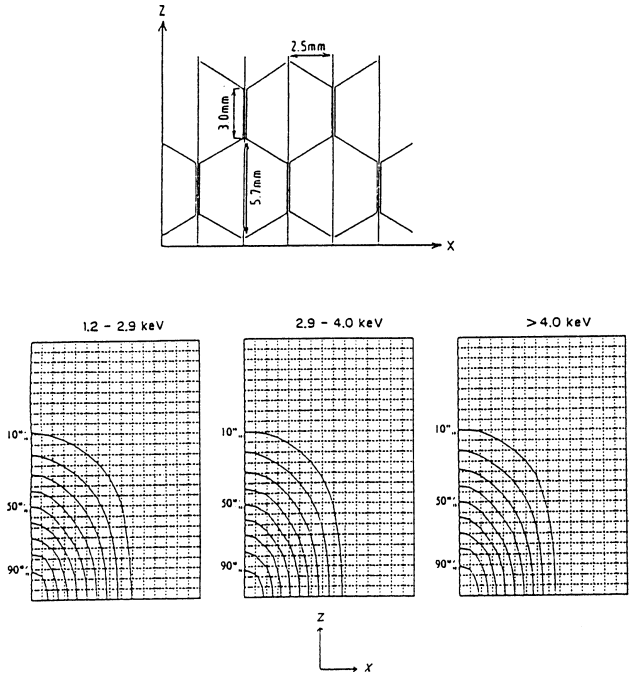

Figure 5.4: The structure and the angular response of the Ginga LAC collimator.

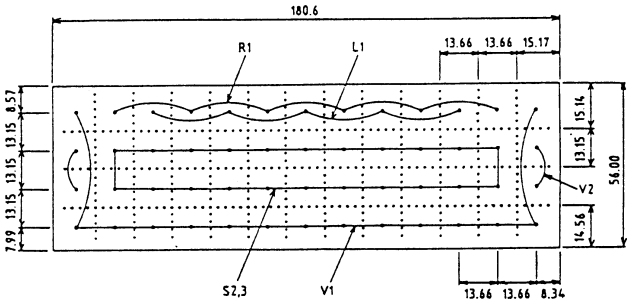

Figure 5.5: The wiring of the signal lines in a LAC.

for the anode and 50μm for grounds. The signals form the first layer just behind the X-ray entrance window are mixed and called the TOP layer, and those from the following two layers are called the MID layer. Figure 5.5 shows the wiring of the signal lines in a LAC. The signals from the 4th layer, together with those from the aluminum plates called end-veto, which are set in front of the end-walls of the anode wire and provide veto-signals induced near end wall events, are mainly caused by cosmic particles through the wall or electrons from the wall Compton scattered by gamma rays.

The counter gas consists of 75% Ar, 20% Xe and 5% CO_2, and its total pressure is 1.86 torr at 0°C. As the counter is 56 mm in depth, the upper energy of the detectable photon is about 35 keV. At the window, the gas is sealed by a beryllium foil with a thickness of 62μm, which intercepts X-rays up to $\simeq$ 1 keV and electrons up to $\sim$ 100 keV. Behind the beryllium window, open area of 11 columns out of 13 excluding both side cells is selected by the collimator. The central cells are thus guarded from the walls on three sides by the cells in the right and left side and those in the 4-th layers. Therefore, signals form the guard cells are grouped all together and are, together with the end-veto signals, fed into the LAC-E, both proving the veto-signals for background rejection.

The open area of one proportional counter is 665 cm^2. By multiplying the transmissivity of the collimator, the effective area becomes 545 cm^2 and the whole effective area of 8 LACs becomes 4360 cm^2. In the actual operation, the effective area decreases to 4000 cm^2 due to the additional anti-coincidence filtering of coincidence events between each adjacent two cells. Figure 5.6 shows the efficiency of the LAC.

LAC-E processes the signals from LAC-S: L1, R1, S23, V1, V2 and EV in figure 5.5 are converted to the pulse height and timing data, and sent to DP. Figure 5.7 shows the block diagram of LAC-E.

In usual observations, only L1, R1 and S23 signals are selected as real X-ray data. The signals are filtered by the anti-coincidence: the signals are not processed if more than one line signaled at the same time. V1, V2 and EV signals inhibit the processing. Through these selection processes, the charged-particle events that leave long tracks in the gas chamber and signals to more than one line are removed. These filtering remove most of the charged-particle background.

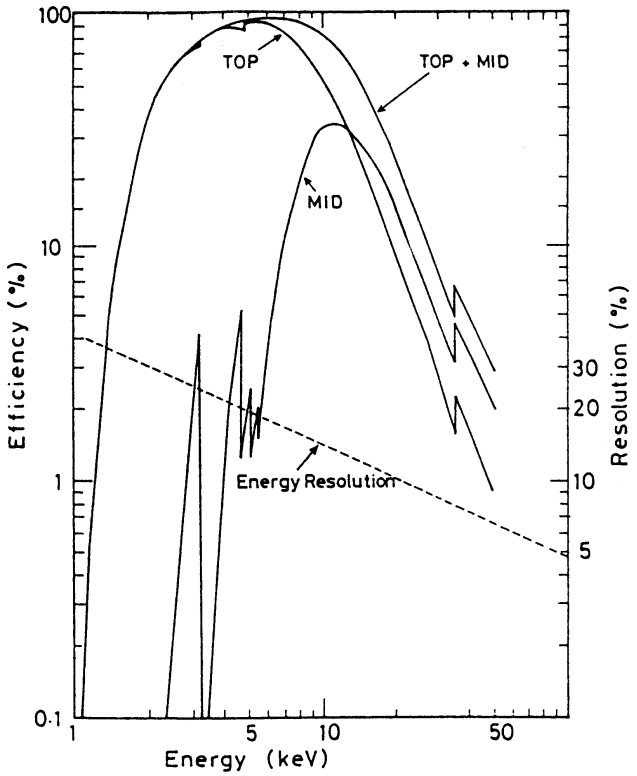

Figure 5.6: The detection efficiency and the energy resolution of the LAC for each layer.

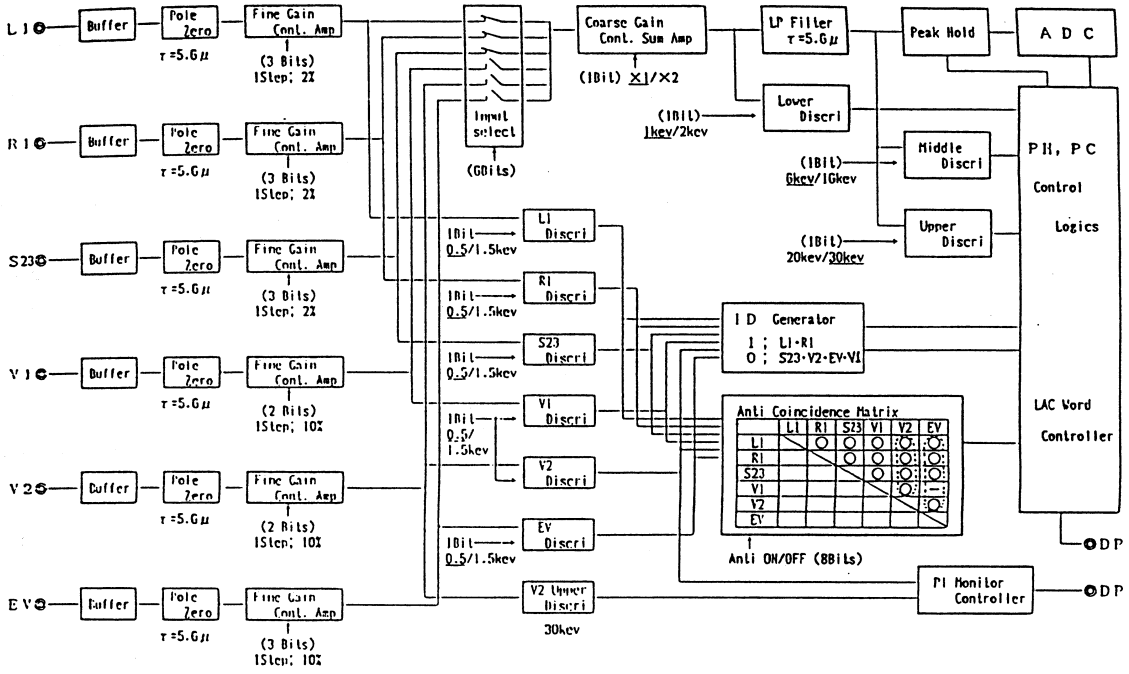

Figure 5.7: The block diagram of the LAC-E.

The pulse height corresponding to 0–37 keV is converted to 64 channels in LAC-E, then DP compresses them to 48 channels by rebinning the higher 32 channels into 16. At the same time, another 1 bit information to discriminate the event between the lower and middle discriminator level (called PCL data) and between the middle and upper (PCH) are sent to DP.

DP counts the number of events in each pulse-height channel using on-board memory in a fixed time interval, and compiles the resultant spectrum into telemetry format. Depending on the requirement of spectra or timing, data from each layers and detectors can be combined on-board, providing four modes for the LAC data:

MPC-1 Events are accumulated separately for the TOP and the MID layers of the 8 detectors, thus producing 16 separate spectra simultaneously. The energy corresponding to the lowest two channels are below the lower discriminator. This mode is mainly used for spectral study of faint sources.

MPC-2 Events from 4 counters and 2 layers are combined, thus 2 spectra are accumulated. The temporal resolution is 8 times finer than MPC-1 mode.

MPC-3 Events from all counters and layers are combined into one. In addition, the pulse heights are rebinned into 12 channels: each energy channel corresponds to 4 consecutive channels in the MPC-1 and -2 modes. The temporal resolution becomes 64 times finer than MPC-1 mode. This mode is used mainly for fast timing studies with intermediate energy resolution.

PC In this mode, the discrimination data is used instead of the ADC data. Events from all counters and layers are combined into one. The temporal resolution of PCL and PCH data becomes 4096 and 2048 times finer than MPC-1 mode, respectively. This mode is used only for fast timing observation of the bright galactic objects.

Table 5.1 gives the number of energy channels and the maximum temporal resolution of these four modes for three recording bit rates.

5.2 ASCA

ASCA is the 4th Japanese X-ray observation satellite launched on 20 February 1993, by the M–3SII–7 rocket from KSC, the same rocket series and launching site as those of Ginga.

The satellite orbit is semi-circular with the perigee of 520 km, the apogee of 620 km. It weights 417 kg and is 4.7 m long along the telescope axis and 3.5 m wide across the solar paddles. Figure 5.8 shows the schematic view of ASCA in orbit.

Table 5.1: Temporal resolutions of the LAC data.

Mode	number of	Bit rate		
	PH Channel	High	Medium	Low
MPC-1	48	500 ms	4 s	16 s
MPC-2	48	62.5 ms	500 ms	2 s
MPC-3	12	7.8 ms	62.5 ms	250 ms
PC	2	0.98/1.9 ms†	7.8/15.6 ms†	31.3/62.5 ms†

†: For PCL/PCH data.

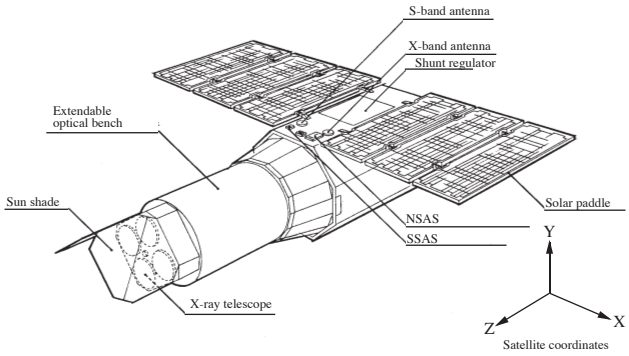

Figure 5.8: The schematic view of the ASCA satellite.

Since the orbit is similar to *Ginga*, up- and down-link operations are also the same, except that *ASCA* can do down-link of the stored data to NASA DSN stations of Madrid, Canberra, Goldstone, Wallapse and Santiago. These reproductions are previously programmed in the KSC contact pass.

ASCA has four observation instruments; two Gas Imaging Spectrometers GIS; Ohashi et al. 1996) and two Solid state Imaging Spectrometers (SIS). These instruments are both equipped with a X-ray telescope of a 3.5 m focal length, and have imaging capabilities. Since M–3SII type rocket has no space for the optical bench with the long focal length, the telescopes are mounted on the top plate of an extendable optical bench.

The satellite attitude control system is essentially the same as *Ginga*, but has significantly improved capability with three-axis stabilization and the pointing accuracy better than 10 arcsec and about $\simeq$ 30 arcsec, respectively. To achieve them, *ASCA* is equipped with 4 plus one back-up gyros, four reaction wheels, two CCD star cameras and 3 magnetic torques; all have control electronics. The satellite attitude is limited to keep the direction of the solar paddle within 30° from the sun.

A biased and sun-direction angular momentum is always given in the 4 wheels, hence, in emergency, the satellite can automatically go into a safe-hold mode, which is a spinning mode around the sun vector. The maneuver is performed by changing the angular momentum balance among the reaction wheels. The slew rate is $\simeq 0.2^{\circ}s^{-1}$.

As the telemeter channel, *ASCA* uses X-band (down-link at KSC, 8.5 GHz) and S-band (up-link 2.1 GHz, down-link 2.3 GHz). Unlike *Ginga*, the stored data are reproduced in X-band with higher bit rate than the real-time data. The orbital elements are measured twice a day.

The data from the detectors and on-board instruments are processed by the data processor (DP), then stored in the bubble data recorder (BDR) with 134 Mbits capacity. DP has three bit rates, High of 32 Kbits s^{-1}, Med of 8 Kbits s^{-1} and Low of 1 Kbits s^{-1}; thus the recording time is 68, 273 and 2185 minutes, respectively. Bit-High is mainly used in the contact orbits, and Bit-Med in the remote orbits. Bit-Low is used to save the BDR capacity when the detectors cannot observe the target, i.e., the satellite is in the South Atlantic Anomaly (SAA) or the target is behind the earth.

5.2.1 XRT

ASCA has four identical conical foil X-ray mirrors which are light-weight versions of similar mirrors flown earlier on the Broad Band X-ray Telescope experiment (BBXRT) aboard NASA's Astro-1 space shuttle mission. Since the X-ray photon of a few keV is reflected only in a grazing incident angle, or the light pass is almost parallel to the mirror surface, effective area of the X-ray reflector

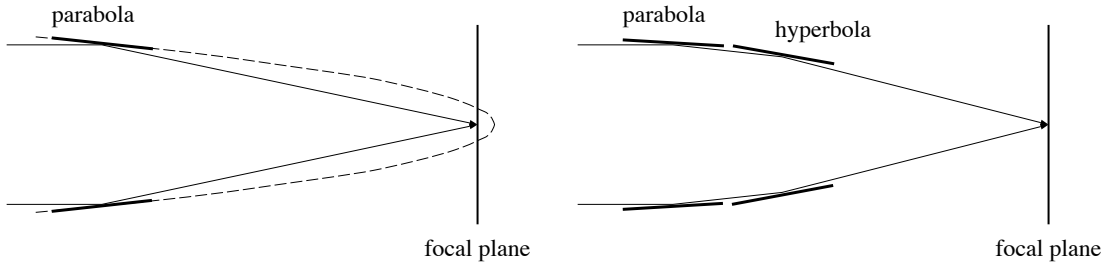

(a) (b)

Figure 5.9: The schematic figure of the X-ray telescope. (a) The primitive model. (b) Wolter type I geometry, which is used in ASCA XRT.

is largely limited; for example, see the case for a paraboloid (figure 5.9a). To gain reflection area and to compensate for aberrations, the X-ray mirror consists of multi-nesting tandem with aligned and co-focusing paraboloids and hyperboloids (Wolter type I geometry; figure 5.9b). *ASCA* XRT approximates this concept with flat conical surfaces instead the parabolic or hyperbolic surface. This practical simplification was crucial in allowing us to construct the multiple-nesting of 119 thin foils for one XRT. Nearly flat pieces of aluminum foil 125μm thick are first shaped into flexible conical segments having approximately the required curvature. They are then dipped in an acrylic bath to smooth the surface, and plated with a $\sim$ 500Ågold layer to increase X-ray reflectivity. They are finally placed in a housing, constrained by supporting lags to fit the X-ray optics.

One XRT with 119 foils aligned by $\sim$ 1 mm pitch has an effective area of 558 cm^2, more than 50% of the geometric open area. A trade-off of this large effective area by the thin foil mirrors is found in less spatial resolution than the ideal Wolter type 1 optics. The half power diameter of XRT is about 3 arcmin. Table 5.2 gives the design parameters of XRT.

To maintain the best-performance of the mirror in orbit (i.e., to keep the reflecting surfaces free from contaminations and to minimize the mirror deformation by thermal stress), heaters and thin (0.22 and 0.54μm for the SIS and GIS, respectively) aluminized mylar covers were placed on the entire mirror aperture.

Since X-ray reflectivity depends on the grazing angle and photon energy, the efficiency and point spread function (PSF) of XRT also depend on the source position and energy. The efficiency and PSF are calibrated on ground in several points (for energy, mirror position, and incident angle), but overall features are simulated with the ray-tracing with appropriate optical constant (complex refractive index) of the mirror foils, including the actual XRT structures.

The final response is supplied by the ASCA team with fine tunings to fit the standard sources: Crab for spectrum and Cyg X-1 for imaging.

Figure 5.10 shows the energy dependence of the XRT effective area. The values used to plot

Table 5.2: XRT design and performance parameters.

Design Parameters	
Mirror Substrate	0.125 mm aluminum foil
Surface	10μm Acrylic Lacquer + 500 ÅAu
Number of Nested Cones	120 (back-to-back layers)
Outer/Inner Diameter	345/120 mm
Focal Length	3500 mm
Grazing Angle Range	0.24–0.70 deg.
Geometric Area	558 cm^2 (each)
Field of View	24/16 arcmin (@1/7 keV)
Number of Telescopes	4
Mirror Weight	10 kg (each)
Performance Parameters	
Effective Area	$\simeq$ 300/$\simeq$ 150 cm^2@1.5/7 keV (each)
Size of Blur (Encircled Energy)	$\simeq$ 3 arcmin Half Power Diameter (no energy dependence)
Reflector Surface Roughness	$\simeq$ 3 Å

the graph are an integrated flux within the 6 arcmin circular area from the image center.

The effective area decreases rapidly as the off-axis angle increases. At higher incident energy, only the inner foils remain effective since the grazing angle become smaller. Accordingly, effective area decreases significantly as energy increases. Figure 5.11 shows the off-axis angle dependence of the effective area.

Possible residual deformation of the foils results in loss of the angular resolution. While the half power diameter (HPD) of XRT is expected to be about 0.3 arcmin in an ideal case, the actul value is about 3 arcmin.

Figure 5.12 shows the radial profile of the PSF. It can be approximated as a Gaussian in the central core of ($r < 1'$), followed by an exponential function outside. The quadrant mirror structure makes the PSF take a Maltese cross shape (figure 5.13). As the off-axis angle increases, the PSF is largely distorted.

For the evaluation of the contamination of a bright source to the other regions, the encircled energy function (EEF) defined as the ratio of photons flux in a circle with given radius from a point source is useful. Figure 5.14 shows the EEF for different energies. It shows that 80% of the flux drops within the circle of a 12 arcmin diameter. The difference of the encircled fraction between high and low energy becomes large as the angular radius increases. Therefore, the apparent spectrum becomes harder as the accumulation radius increases.

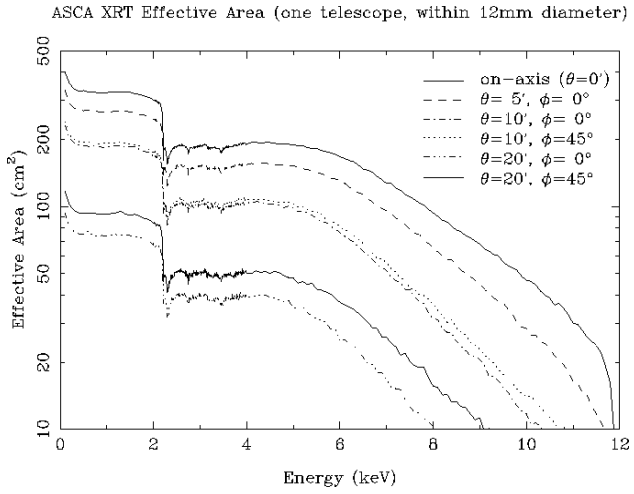

Figure 5.10: The energy dependence of the XRT effective area on-board ASCA.

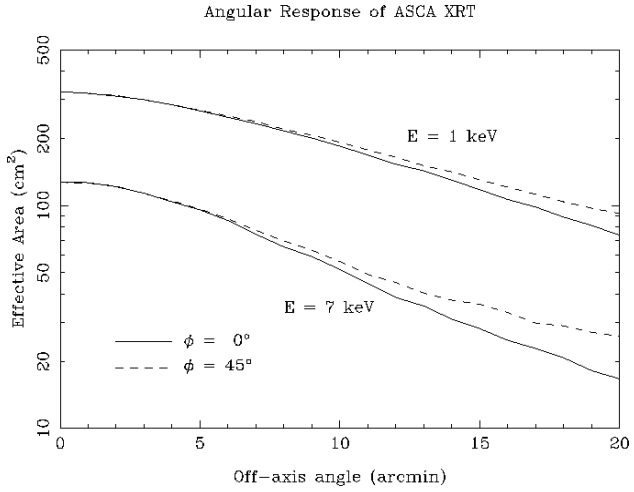

Figure 5.11: The off-axis angle dependence of the XRT effective area on-board ASCA.

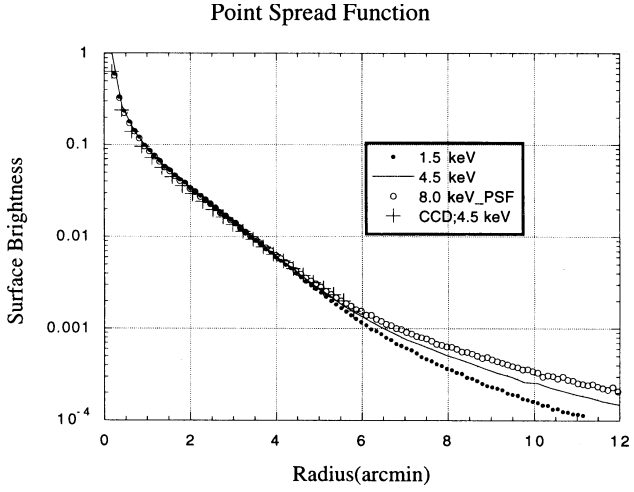

Figure 5.12: The point spread function of the ASCA XRT (Serlemitsos et al. 1995).

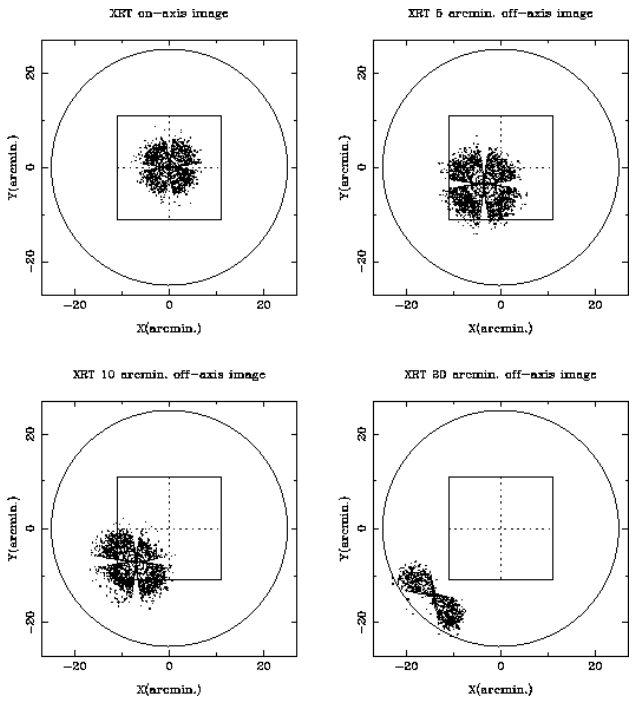

Figure 5.13: Point spread function of the ASCA XRT for four different off-axis angles. Approximate field of view is shown for GIS (circle) and SIS (square).

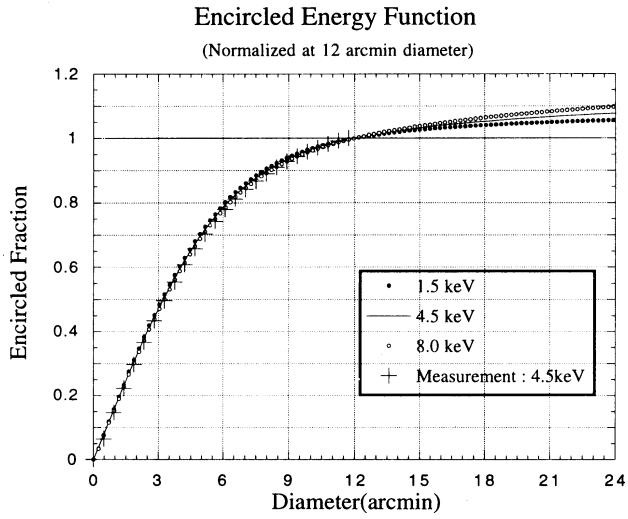

Figure 5.14: The encircled energy function of the XRT.

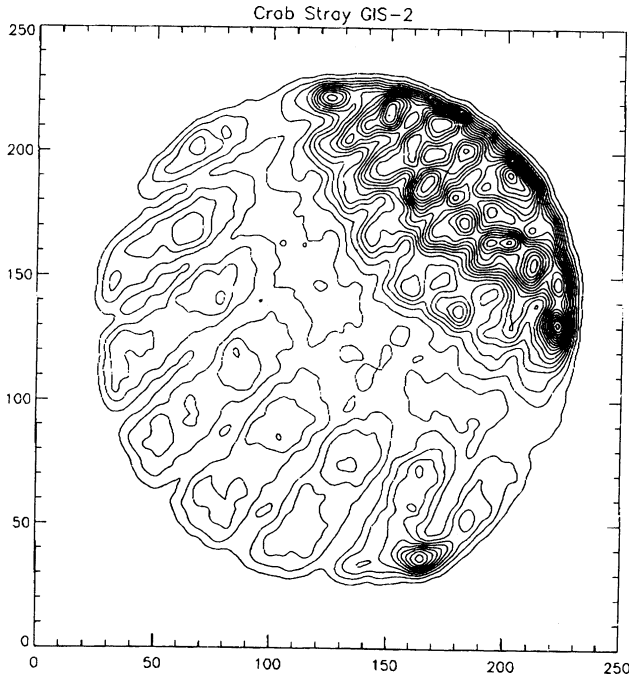

Figure 5.15: The stray light image of the Crab nebula at 1° offset from the detector center.

Another problem of the XRT is stray light from outside of the field of view (FOV). The XRT geometry prevents photons that were not intercepted by the foils from reaching the focalplane; however, the photons scattered due to the surface roughness, single or more than 3 reflection, or back-side reflected photon maypass into the focal plane. We call these photons stray light. Figure 5.15 shows the image of the stray light when the Crab nebula is 1° offset from the detector center. The stray light, if a strong source is nearby, interferes with the observations of a weak source or extended emission, such as the cosmic X-ray background (CXB).

5.2.2 GIS

The GIS (Gas Imaging Spectrometer), which has been developed mainly by the University of Tokyo, ISAS and Meisei Electric Co., Ltd., consists of two imaging scintillation proportional counters (GIS-S2 and -S3) and a part for signal processing (GIS-E). It is also equipped with the radiation belt monitor (RBM).

Compared with the SIS (see next subsection), the GIS has larger efficiency (by a factor of 2 at 7 keV) at high energy, higher temporal resolution, higher signal saturation flux and a four-times wider FOV. However, it has a lower soft X-ray efficiency, a somewhat worse position resolution and poor energy resolution (by a factor of 2-4).

Each GIS-S consists of a gas cell, a position-sensitive phototube and high-voltage suppliers. Figure 5.16 shows the cross section of the GIS-S. X-rays from the XRT are detected by the 25 mm-

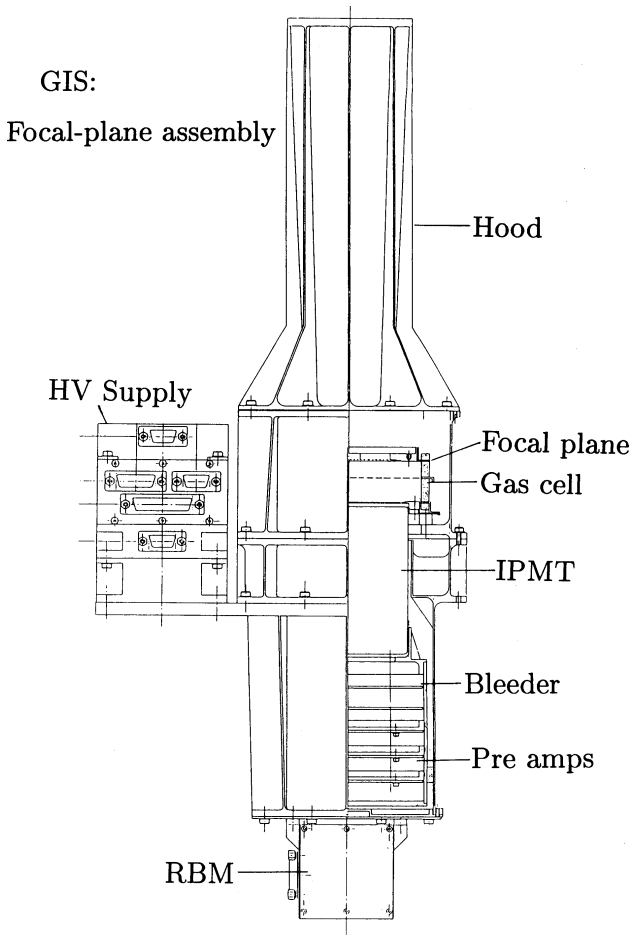

Figure 5.16: The cross section of the GIS-S.

depth gas cell, which is filled with 96% Xe and 4% He to 1.20 atm pressure (at 0°C). The gas is sealed by a beryllium foil with a thickness of 10μm and a diameter of 52 mm, supported by a stainless steel grid and fine mesh. The gas cell is divided into two, the drift region just inside the Be window and the following scintillation region. Each region is biased by 1 kV cm^{-1} and 4 kV cm^{-1} electric fields. To intercept the non-X-ray backgrounds, the GIS has a hood coated by a 0.2–0.5 mm-thick tin foil and partially by a 0.1 mm-thick molybdenum foil.

The X-ray photon is photo-absorbed in the drift region and creates free electrons. The electrons drift into the scintillation region guided by the bias field, then are accelerated by the stronger field. The electrons are decelerated by collision with the Xe atoms, while exciting them in turn. The excited Xe atoms return to the ground states by emitting UV photons with wavelength of $\simeq$ 170 nm. This excitation and relaxation processes occur as the electrons pass the scintillation region in 2–3μs; thus, a scintillating column is formed through the drift region. The number of UV photons are $\simeq 1.5 \times 10^5$ for a 6 keV X-ray photon. Since these processes are not accompanied by secondary-electron multiplication, the energy resolution is kept 2-3 times better than the proportional counter.

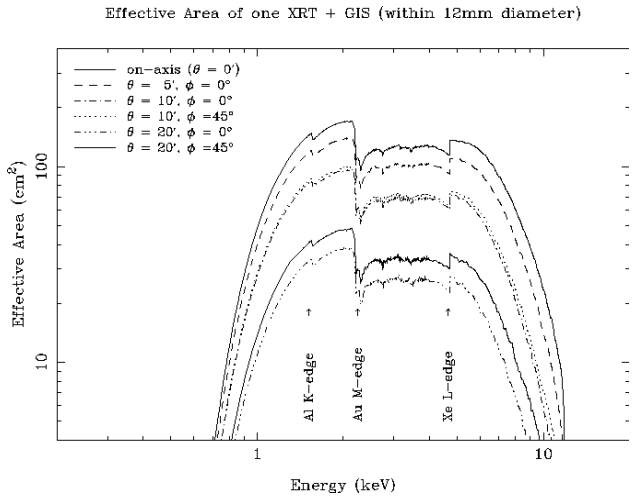

Figure 5.17: The effective area of the combination of XRT and GIS.

The scintillation UV photons are detected by a position-sensitive phototube set below the gas cell. Figure 5.17 shows the effective area of the combination of XRT and GIS.

The signals from the phototube are processed by GIS-E. The energy information is obtained from the final dinode signal. The energy resolution is about 8.0% (FWHM) at 5.9 keV, which scales as inverse square root of the energy. X and Y positions of a detected photon are calculated using outputs from 32 (16 for X and16 for Y) multi-wire anodes. The position resolution is about 0.5 mm (FWHM), which corresponds to about 30 arcsec, at 5.9 keV, and scales as inverse square root of the energy.

To eliminate non-X-ray backgrounds, only events whose rise time is within the window set by the command is passed to the on-board CPU. With this process, about 90% of backgrounds within 2–10 keV signal range are eliminated. In addition, on-board CPU eliminates the events that are positioned outside a certain radius or whose spatial distribution of multi-anode output is larger than a certain length. This discrimination method is called SPRD. Without SPRD, it is known that the strong source near the edge of the GIS, such as the calibration source, makes a ghost image at the inner area if the event position is determined with the Fast Lorentzian Fitting, used for the usual data processing. With these discriminations, 99% of the non-X-ray background is eliminated and the remaining non-X-ray background in the 17 arcmin radius is 5×10^{-4} counts s^{-1} cm^{-2} keV^{-1} in 2–10 keV.

Since the telemetry capacity is limited, the GIS has four different telemetry modes:

PH (Pulse Height) For nominal observations, this mode is usually used. Data for one event consists of the pulse-height, position, rise-time, event-spread and timing information packed to 32 bits. The commandable bit-shares are 10, 8, 5, 8 and 10 bits in normal operation. In

Table 5.3: The temporal resolutions and the maximum source intensities of the GIS.

mode	Bit rate	Temporal resolution Timing bits 0 bit	Timing bits 10 bits	Maximum Source Intensity [count s^{-1}]
PH	H	62.5 ms	61μs	256
	M	500 ms	488μs	32
	L	2 s	1.95 ms	8
PCAL	H	31.25 ms		32
	M	250 ms		4
	L	1 s		1
MPC	H	0.5 s	1.95 ms	128 Crab†
	M	4 s	15.6 ms	16 Crab
	L	16 s	62.5 ms	4 Crab

†: 1 mCrab $\sim$ 1 event s^{-1}

this mode, all data are processed by the on-board CPU.

PH PCAL (Position Calibration) This mode is prepared for the calibration of the position calculation done by on-board CPU. All information, including the 32 anode signals, are transmitted. Thus the maximum source intensity and the temporal resolution are reduced significantly from the PH mode. PCAL data, however, can be processed on ground in case of on-board CPU failure.

MPC (Multi-channel Pulse Count) This mode transmits only the pulse-height and timing information. The pulse-height converted data are accumulated in the on-board memory in DP. The maximum number of spectral bin is 256, which can be reduced to increase time resolution. This mode can be used for an extremely strong source or in the case of on-board CPU failure.

memory check This mode dumps the RAM image (32 KB×2) of on-board CPU as it is. Usually, this mode is carried out once a day during the KSC contact to check for memory loss.

Table 5.3 gives the temporal resolution and maximum source intensity of the GIS in each telemetry mode.

The gain of the GIS differs from position to position, hence the gain calibration by pointing Cas A in various positions has been performed. In addition, the gain changes with pressure and impurity of the counter gas and the phototube temperature. To correct for these effects, the gain

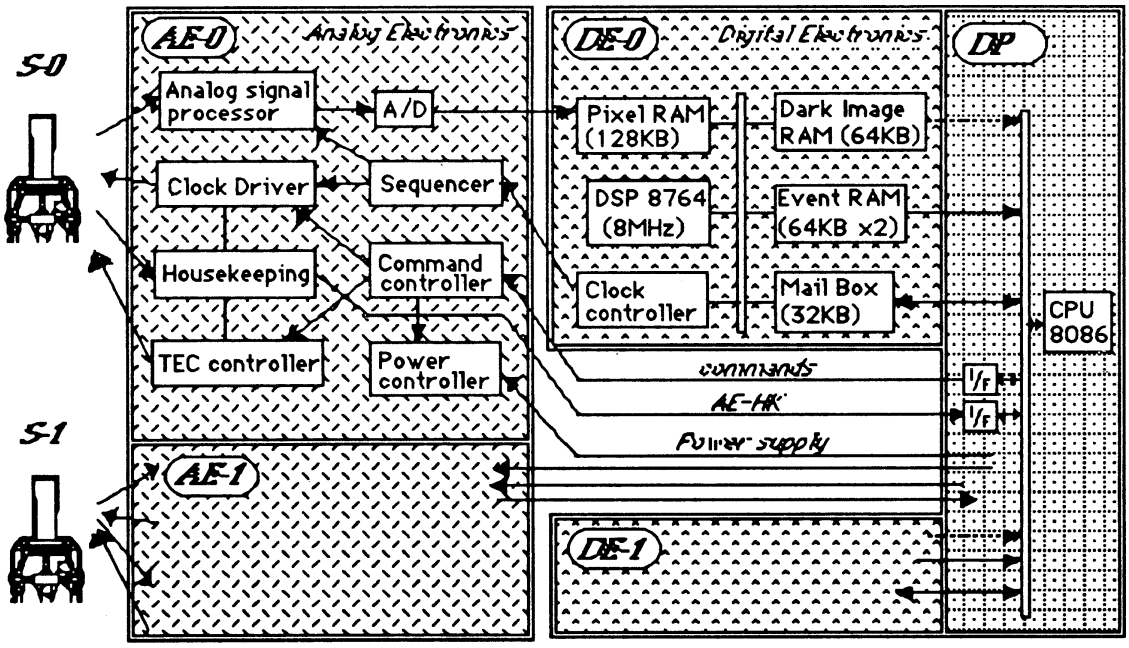

Figure 5.18: The signal block diagram of SIS.

of the GIS is monitored by ^{55}Fe isotopes at the edges of the entrance windows of the each gas cell. These calibration data are accumulated by the ASCA team and distributed to the end users.

5.2.3 SIS

The SIS (Solid state Imaging Spectrometer) consists of three components — two cameras (SIS-S0 and SIS-S1), each with four CCD chips, the analog electronics (SIS-AE) and the digital electronics (SIS-DE). SIS-DE is equipped within the DP body. The DP also takes part in the SIS data processing. Figure 5.18 shows the signal block diagram of the SIS subsystem.

The CCD detector can be regarded as a cluster of solid state detectors (SSD) with a large number of square-aligned microscopic ($27 \times 27 \mu m^2$ in case of SIS) electrodes called 'pixels'. The electron cloud induced by the X-ray photon is absorbed by the nearest pixels, then are carried by the driving external clock from pixel to pixel to the readout gate.

Since the charge is thus transferred from pixel to pixel with very small electric capacitance, the floating electric capacitance at the readout gate is also very small. This extremely small capacitance makes a higher readout voltage than normal SSD; hence the readout noise can be kept very small. On the other hand, the temporal resolution is much lower than the normal single detector such as GIS, because the charges are read sequentially. In the case of SIS, the readout cycle of one chip is 4, 8 or 16 sec in 1-, 2- or 4-CCD mode, respectively.

Figure 5.19 shows the cross section of the SIS camera, and figure 5.20 shows the chip configu-

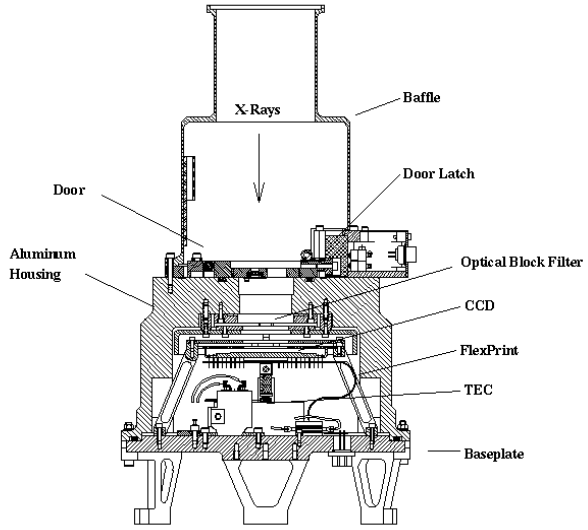

Figure 5.19: The cross section of the SIS camera.

ration of the SIS. During normal operation, the CCD chip is cooled to about $-60°$C by a Peltier device (TEC, thermal electric cooler) to reduce the dark current. The TEC dissipates the heat into the housing, which is cooled to -30–$40°$C with the radiator coupled to the heat pipe. The chip in the housing is covered by a multi-layer insulator and supported by Lexan columns in order to reduce the heat inflow. In front of the chip, a 1000Åthick Lexan film coated with 400Åthick aluminum layer is placed at each side to cut off optical light.

The SIS-AE generates the chip driving clock, controls the TEC and converts the video signal from the SIS-S into digital data (PH data). In contrast to GIS, SIS has no hardwired logic.

The SIS-DE receives the PH data from the SIS-AE and extracts the X-ray events. The X-ray photon with 10 keV energy induces a primary electron cloud 1μm in size by the photo-absorption process, with the size scaling as $E^{1.75}$ (Janesick et al. 1985). After drifting to the electrode of each pixel, the size is increased to $\sim 5\mu$m. Since this size is still smaller than the that of a pixel, the electron cloud does not separate into more than four pixels (figure 5.21). On the other hand, charged particle events leave long tracks (long cloud). Using this difference in cloud size, SIS-DE can eliminate the-X-ray backgrounds. The energy of the X-ray event is calculated from 3×3 pixels around the local maximum pulse height pixel.

The dark current level consists of 'Dark level' and 'Bias level'. To save the on-board memory, the Dark level is taken from the average of the pixel group, which is typically in a $\frac{1}{16} \times \frac{1}{16}$ (default value) frame. This dark level is further time averaged and is updated using the event-free pixel

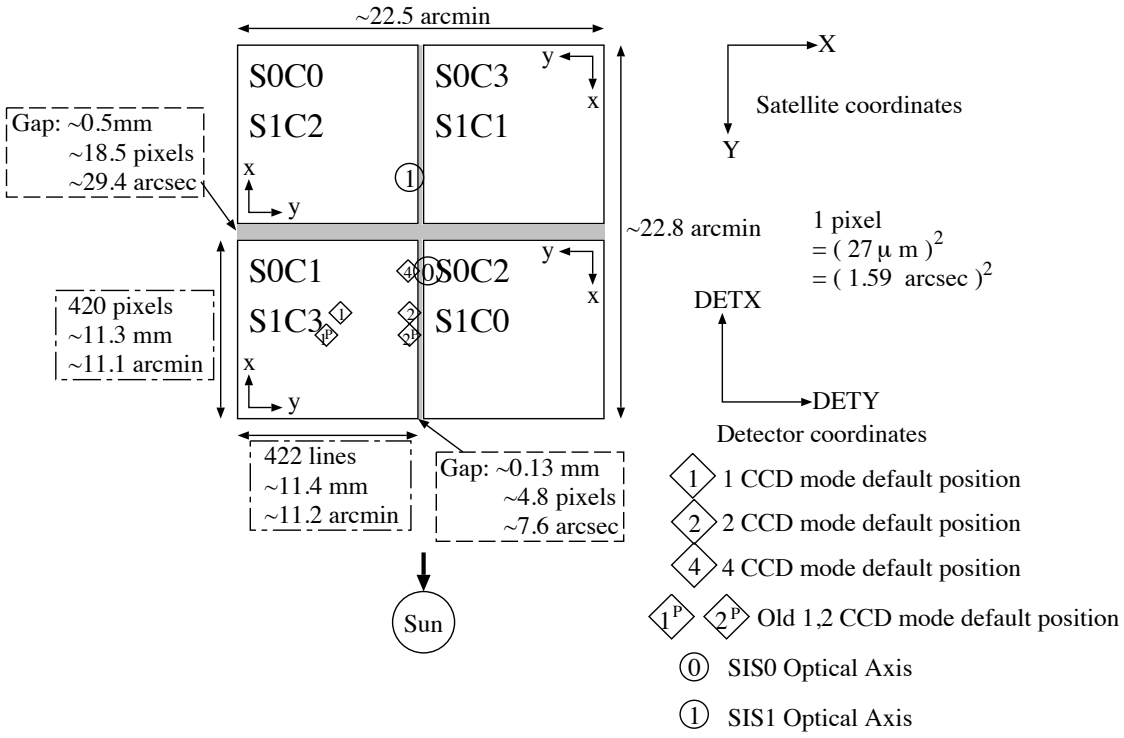

Figure 5.20: The chip configuration of the SIS.

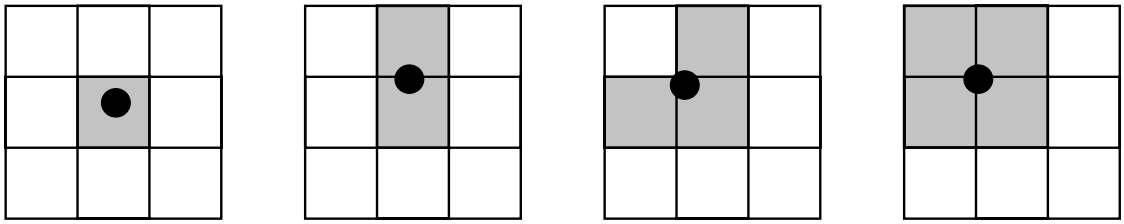

Figure 5.21: The X-ray event pattern of the CCD detector.

levels as:

$$\text{NewDarkLevel} = \text{OldDarkLevel} + \frac{\text{MeanPixelLevel}}{n} + 1, \tag{5.1}$$

where $n + 1$ is the history parameter and set at 1, 4, 8 or 16 on command. The set of Dark level is called the dark frame. The Bias level is the DC offset of the dark current level. This is obtained from the PH data of the overclock region, where there is no real electrode, and where but only the driving clock is operated to these virtual pixels. Since the Dark level and the Bias level are the mean value in the grouped pixels, their possible variation within the group degrade the energy resolution essentially taken from multiple pixels. In fact, the radiation damage caused by the cosmic rays makes the Dark level larger as the satellite spends time in orbit, hence the energy resolution becomes worse. To take account of or to compensate for this degradation, two approaches are currently used: (i) To update the response matrix periodically to account for the long-term change of the resolution. This method can be applied to any data, but needs the long term trend for pixel by pixel, which require a lot of work, hence has only been applied to a limited region. (ii) Since the Dark level of each pixel is found to be rather constant in a shot time scale (a few days), we can obtain the pixel-by-pixel dark template for the short time scale, by observing the night earth with frame mode or by accumulating the event-free corner pixels of the faint mode data (see below). With this template, we can adjust the pulse height on the ground. This method can be applied for the faint mode data and the grade-0 bright mode data.

The SIS has three observation modes (faint, bright and fast) and four diagnostic modes (frame, dark frame, histogram and integration):

Faint The event information consists of the CCD ID, the addresses and 12 bit pulse heights of nine pixels. The size of each event is 16 bytes including the CCD ID. This mode can be used only for faint sources, but all the pulse heights relating with the event is obtained.

Bright The pulse heights of 9 pixels are summed, and the summed PH data and the Grade information are transmitted. Table 5.4 gives the definition of the Grades. The event data has 4 bytes and consists of the Grade, addresses and the summed pulse height binned up to 11 bit scale; the original 1024-2047 channels are binned by a factor of two and 2048–4095 by a factor of four.

Fast In this mode, the chip is driven to project all the charge onto one dimension, so the spatial information is reduced: instead, the scan period of a frame becomes faster than the other modes. The event data has 2 bytes and consists of the Grade, the reduced addresses and the pulse height binned as the bright mode. This mode is used for extremely strong point source

Table 5.4: The grade definitions of the Bright-mode SIS events.

grade	name	split pattern
0	single	center
1	single+	center (+ detouched corner(s))
2	vertical split	center + top or bottom (+ detouched corner(s))
3	left split	center + left (+ detouched corner(s))
4	right split	center + right (+ detouched corner(s))
5	single-sided+	single-sided split + touched corner pixel(s) (+ detouched corner(s))
6	L or square	L or square split (+ detouched corner(s))
7	Others	all others

Table 5.5: Observation modes of the SIS.

	Faint	Bright	Fast
Temporal resolution†	4/8/16 s	4/8/16 s	16 ms
Maximum event rate‡	128/16/4	512/64/16	1024/128/32
PHA bits	12	11	11
Spatial bits	9×9	9×9	1 (and 3 timing bits)
Number of grade	—	8	2

†: In 1/2/4 CCD mode for Faint and Bright.

‡: In bit High/Med/Low. The unit is [events/s/2sensors].

whose X-rays may hit a chip at higher levels than the saturation level within accumulation time if other modes are used.

Frame This mode sends the pulse heights of all pixels with 12 bit resolution.

Dark frame This mode sends a map of dark frame to ground with 8 bit resolution.

Histogram This mode makes the histogram of pulse heights of 4096 bins for all pixels and sends it to ground.

Integration This mode integrates the events in the chip for 160 s, reads the resultant pulse heights and sends them to ground with 12 bit resolution.

The SIS has three clocking mode for observation and frame modes — 1, 2 and 4 CCD modes. The exposure time for each clocking mode is 4, 8 and 16 s, respectively. Table 5.5 gives the summary of the three observation modes.

SInce the SIS has no radio isotope, the relative gain between each chip was determined with the strong Fe-K emission line of supernova remnant W49B. All chips were pointed to SNR W49B,

and the gains were determined within 0.5% errors. The absolute energy scale was determined with the strongest internal background emission line, Ni, originating in the Kovar (an Fe-Ni alloy) frame-store shield.

During the transfer of the charge, a charge loss exists which is called the charge transfer inefficiency (CTI). The CTI is periodically calibrated by pointing Cas-A at each corner of chips. The calibration data is accumulated by the ASCA team and released to the end user.

Chapter 6

SN1006 Study With Ginga

6.1 Observations and Data reduction

To study the spectral feature of SN 1006 up to 20 keV, we analyzed pointing data as well as those of two background pointing near the Lupus Region. As described in the section 3.2, SN 1006 data with large field of view (FOV) are subject to significant contamination due to the emission originating from the Lupus Loop. Therefore, we further analyzed two scan data of the Lupus Loop, in order to examine a large-scale structure of the Lupus Loop. Figure 6.1 shows the observation points and scan paths, and table 6.1 gives the observation date and coordinates. All data were obtained with the MPC-1 mode. Hereafter, we will refer to the two backgrounds and the two scans as BG 1, BG 2, scan 1 and scan 2, as designated in table 6.1.

The data selections were usually made with the following parameters. COR is the minimum momentum per unit charge, cosmic rays below which cosmic rays can not arrive at the satellite orbit. Along the inclined and non-circular Ginga orbit in the bipolar magnetic field of the earth, COR is variable with the orbital phases. EELV is the elevation angle of the FOV from the horizon

Table 6.1: Field centers of pointing and scan paths.

Coordinates (α, δ) in 1950				
Point/Scan	pointing center	scan from	scan to	Observation date
SN 1006	(224.7, −41.7)	—	—	30 July 1988
BG 1	(223.4, −38.6)	—	—	30–31 July 1988
BG 2	(226.4, −39.4)	—	—	7–8 March 1991
scan 1	—	(227.2, −31.8)	(225.4, −51.7)	30–31 July 1991
scan 2	—	(223.2, −33.0)	(214.3, −51.9)	4 August 1990

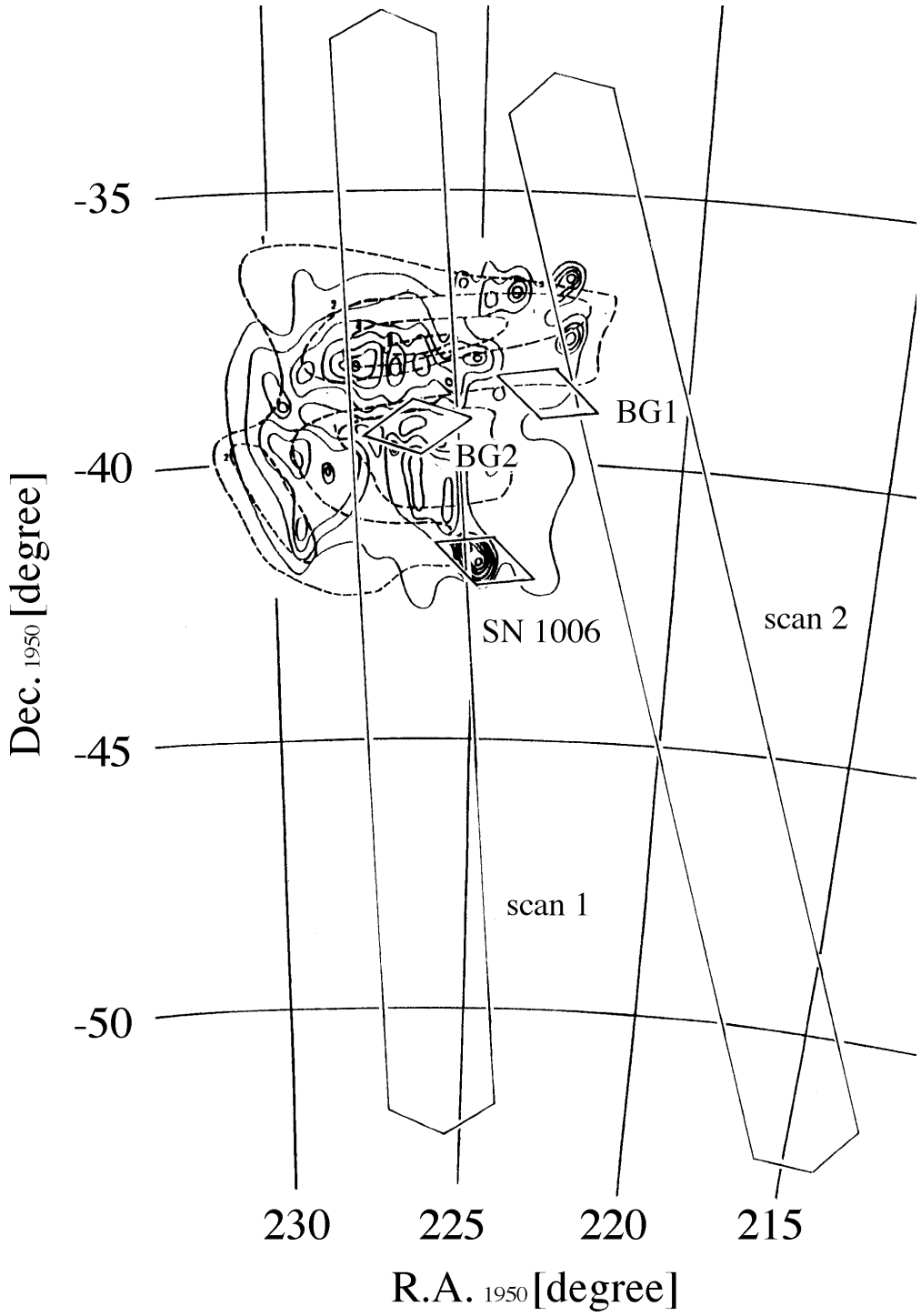

Figure 6.1: Pointing centers and scan paths with 1410 MHz surface brightness contour of Milne (1971) (solid line) and 0.2–1.0 keV feature of Toor (1980) (dashed line). Diamonds represent the LAC fields of view, and the long hexagonal boxes the FOVs of the scan paths.

of the earth. SUD and SSUD is the count rate above 24 keV and 37 keV, respectively. Since both the photon fluxes from the astronomical objects and the quantum efficiency of LAC decrease with increasing energy, while those for non-X-ray events are relatively constant, SUD and SSUD can be good indices of the internal background. In the present case, we have screened with the criteria of COR>9 GeV $c^{-1}Z^{-1}$, EELV>10°, SUD<8000 counts $(128s)^{-1}$ and SSUD<6000 counts $(128s)^{-1}$. The resultant exposure times are 12.3, 12.8 and 12.0 ksec for SN 1006, BG 1 and BG 2, respectively. For the spectral analysis, we used only the Top-layer data to obtain the best S/N ratio. The CXB and non-X-ray backgrounds were subtracted from the three pointing data with the method described in detail by Awaki et al. (1991). The spectral analysis was performed on the FACOM M340 computer of The High Energy Physics Laboratory of Kyoto University with the software package developed by Nagoya University.

Since the collimator response has a cone shape, we extract the whole flux from SN 1006 by assuming the surface brightness of a uniform-disk with a diameter of 30 arcmin. For the local excess near the Lupus Loop, we assumed a constant surface brightness, because the scan profiles shows that the excess flux extends beyond the LAC FOV. The resultant flux, however, depends little on the assumed spatial shape.

6.2 Results

6.2.1 Lupus Region

Spatial distribution

Figure 6.2 shows the background-subtracted scan profiles in the 2–10 keV band. The errors shown are purely statistical, which dominate over the systematic error due to subtraction of the particle background. Since the mean CXB has already been subtracted, the count rate should be 0 count s^{-1} on average if there was no local excess emission; however, as can be seen from the scan profile, there is a clear excess. The peak centered in scan No.1 corresponds to the position of SN 1006, which is located on the southern shell of the Lupus Loop; the smaller northern peak corresponds to the northern part of the shell. The other peak to the south of the main peak is a new X-ray source. Even if we exclude these peaks, we can still see excess emission extending over the Lupus region. The scan profile over path 2 shows more extended emission, although the largest enhancement appears near to the region of the Lupus loop. The fluctuations on spatial scales of 1 degree or so are probably due to uncataloged point sources or, equivalently, to fluctuations in the CXB.

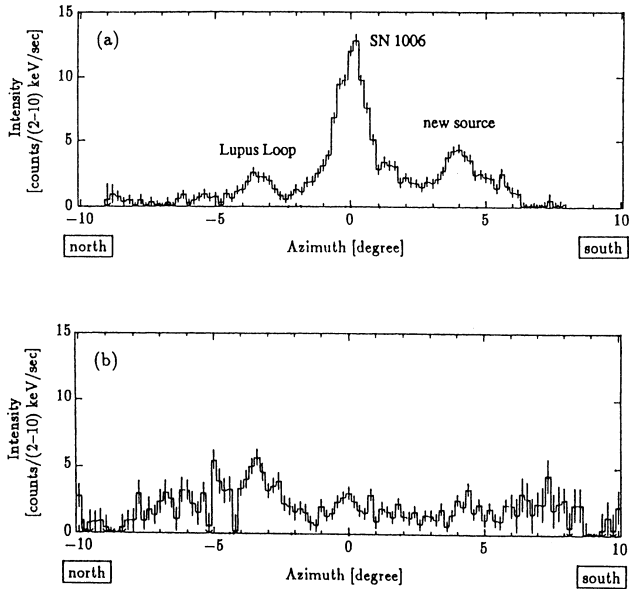

Figure 6.2: (a) Scan profile of path No.1. The horizontal axis shows the scan azimuth along the path. The zero level corresponds to the mean CXB level. Error bars represent 1-σ Poisson error. (b) The same as (a), but for path No.2.

Spectrum

Since the scan data are statistically poor, we performed the spectral analysis only for the BG1 and BG2 pointings. We examined two spectral models for them taking into consideration the interstellar absorption: a thermal bremsstrahlung and a power-law for the continuum, both with Fe-K line. The absorption column densities in both models were lower than that of the LAC window. Therefore, we tried the models again without taking absorption into account.

Figure 6.3 shows the best-fit models with the spectra, and table 6.2 gives the best fit parameters. The parameters of the thermal model for BG 1 are consistent with the *Tenma* values, while the temperature for BG 2 is higher. The photon index of the power-law models are, on the other hand, smaller than the previous *Tenma* value, and their reduced-χ^2 values suggest that the model can be rejected.

The new discovery with *Ginga* is the line emission near an energy of 6–7 keV. The best-fit energy and equivalent width of the emission lines are found to be 6.2–6.4 keV and 100–400 eV, respectively, depending on the positions and continuum models used. With rather large errors, the line energy is consistent with the K-shell transition from neutral to He-like iron (6.4–6.7 keV).

The background-subtracted count rates of BG 1 and BG 2 are 4.2 and 2.3 counts s^{-1}, respectively. These values are within a reasonable range compared with the scan profiles. On the other hand, the background-subtracted count rate of SN 1006 is 23 count s^{-1}, which is much larger than

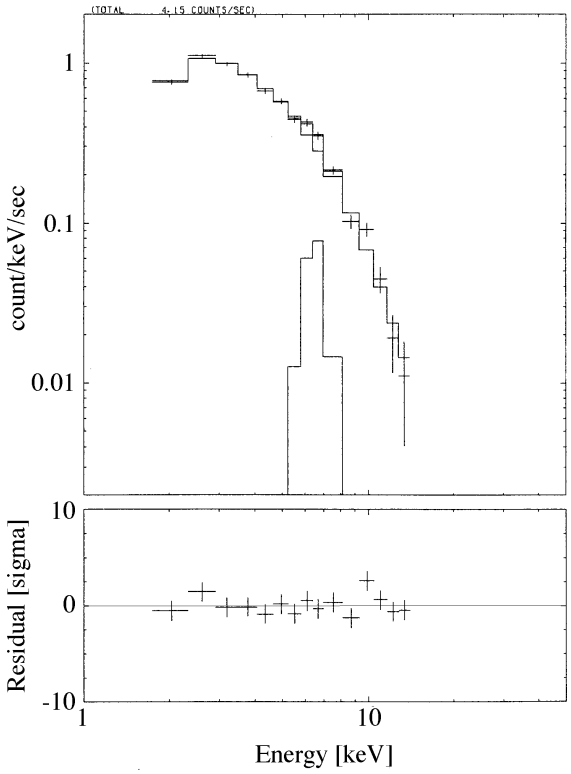

(a) BG1, thermal bremsstrahlung + line.

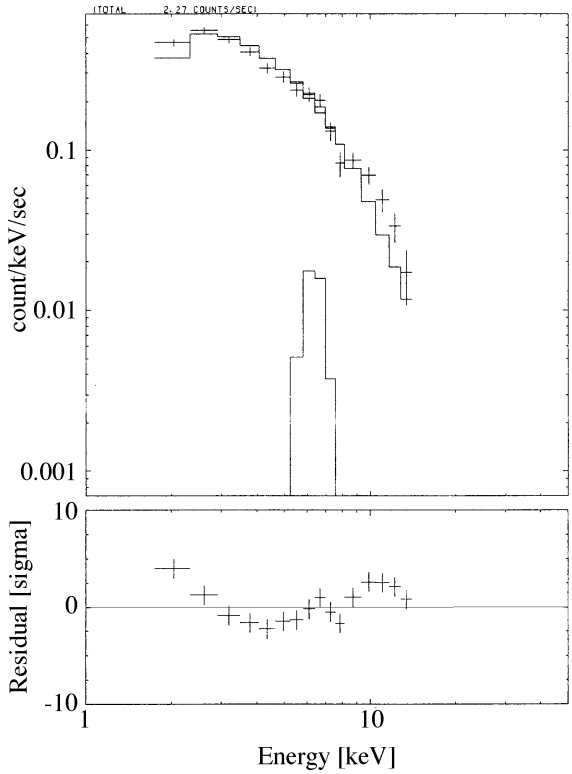

(b) BG2, thermal bremsstrahlung + line.

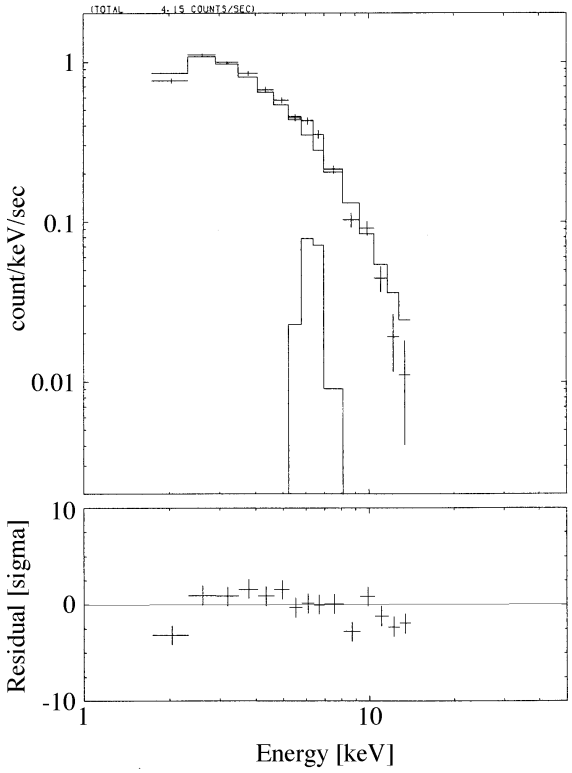

(c) BG1, power-law + line.

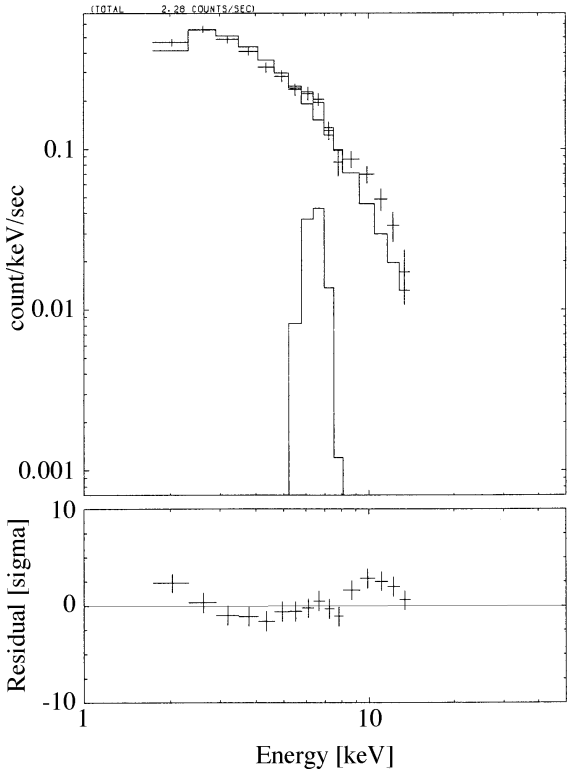

(d) BG2, power-law + line.

Figure 6.3: The Lupus Loop spectra after subtraction of CXB and non-X-ray backgrounds and the best-fit models.

Table 6.2: Results of fitting of Lupus Region.

(a) (thermal bremsstrahlung + line)

	Continuum	Line		Reduced χ^2 (d.o.f.)
	kT_e [keV]	center of energy [keV]	equivalent width [eV]	
BG 1	7.00 ± 0.61	6.33 ± 0.26	348 ± 147	1.23 (11)
BG 2	10.14 ± 0.59	6.22 ± 0.49	138 ± 95	4.46 (12)

(b) (power-law + line)

	Continuum	Line		Reduced χ^2 (d.o.f.)
	photon index	center of energy [keV]	equivalent width [eV]	
BG 1	1.96 ± 0.05	6.22 ± 0.24	350 ± 133	3.25 (11)
BG 2	1.85 ± 0.09	6.37 ± 0.49	277 ± 223	2.00 (12)

$*$ Errors show 1 parameter 90% confidence level.

BG 1 and BG 2. Therefore, the possible ambiguity of the local background subtraction for the SN 1006 pointing is not considered to be a serious problem.

Since we do not a priori know which local background (BG1 or BG2) is better for SN 1006, we subtracted the backgrounds separately, and analyzed the result to obtain a reasonable constraint on the spectrum of SN 1006.

6.2.2 SN 1006

The same model fittings as the local excess spectra were done for the SN 1006 spectra taking into account the interstellar absorption: a thermal bremsstrahlung and a power-law for a continuum, both with the Fe-K line. The former was rejected while the latter was not.

To examine the possibility of a thermal origin, we further tried a single-temperature NEI plasma model developed by Masai (1984), which had already been suggested to fit the SN 1006 *Tenma* spectrum by Koyama et al. (1987). Since the energy resolution of the LAC is limited, individual emission lines from Si and S are not resolved. Nevertheless, we allowed the abundances of Si and S to be free parameters; we then found acceptable fits.

Figure 6.4 shows the background subtracted spectra and the applied models, and table 6.3 gives the best-fit parameters for each fitting.

The photon indices are found to be 3.2–3.3, which is consistent with the *Tenma* value. While the energy range observed with *Tenma* is up to 12 keV, we confirmed in the present observation

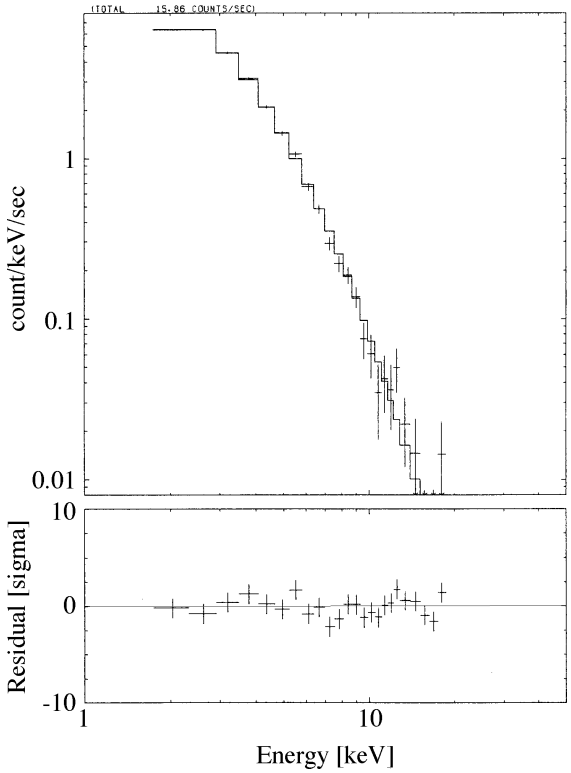

(a) Power-law (BG 1).

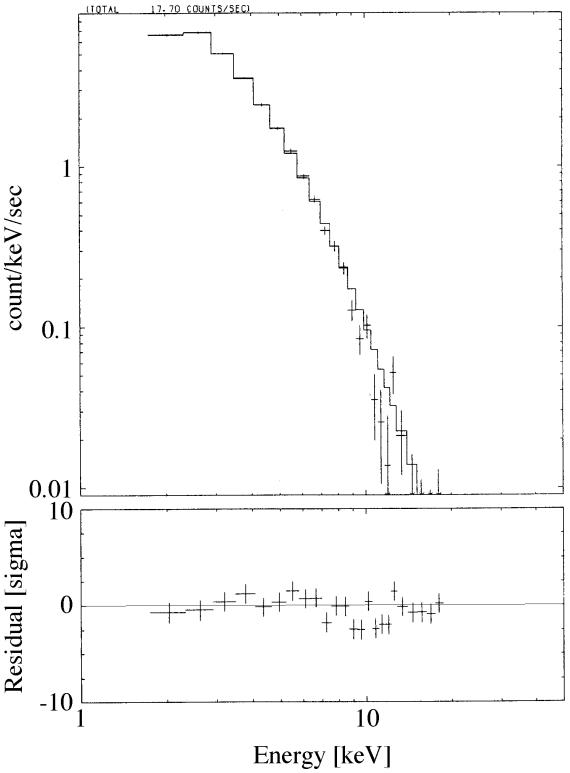

(b) Power-law (BG 2).

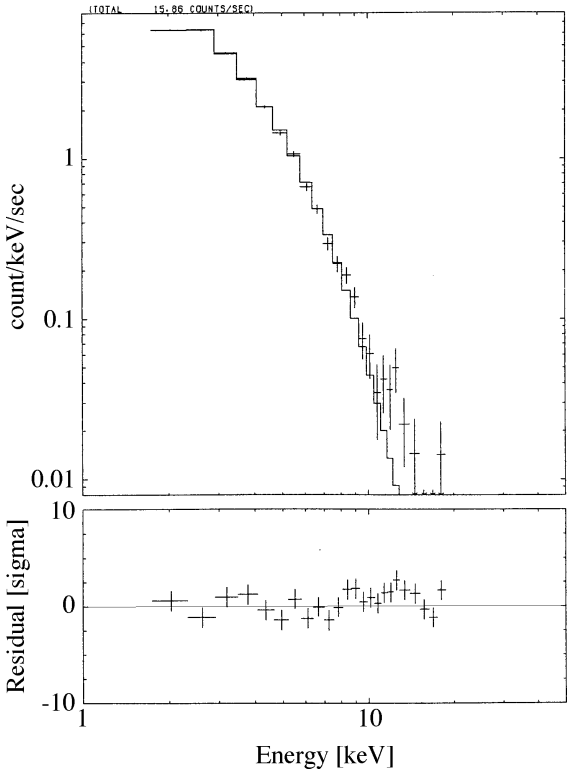

(c) NEI plasma (BG 1).

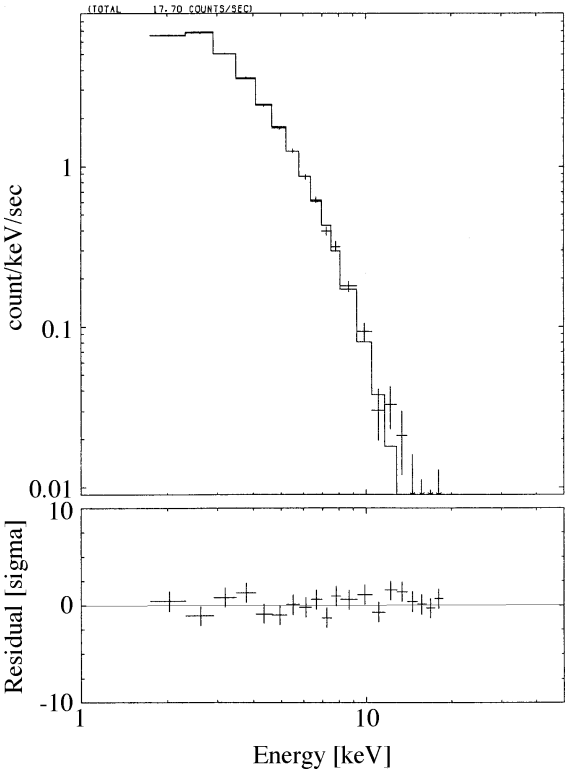

(d) NEI plasma (BG 2).

Figure 6.4: The SN 1006 spectra after subtraction of the backgrounds and the best-fit models.

Table 6.3: Results of fitting of SN 1006.

(a) power-law†

Subtracted Background	photon index	reduced χ^2 (d.o.f.)
BG 1	3.31 ± 0.03	1.10 (22)
BG 2	3.17 ± 0.03	1.75 (22)

(b) thermal bremsstrahlung†

Subtracted Background	temperature kT_e [keV]	reduced χ^2 (d.o.f.)
BG 1	1.78 ± 0.00	16.03 (21)
BG 2	—	—

The fitting for BG 2 was not performed because the BG 1 result gave very poor result.

(c) nonequilibrium ionization thin thermal plasma†

Subtracted background	temperature kT_e [keV]	ionization time $n_e t$ [10^{10} cm^{-3}s]	abundances‡ [solar abundance] Fe	Si, S, Ar, Ca	reduced χ^2 (d.o.f.)
BG 1	2.91 ± 0.02	4.68 ± 0.57	< 0.10	0.61 ± 0.01	1.01 (15)
BG 2	2.60 ± 0.00	3.70 ± 0.07	0.07 ± 0.03	0.60 ± 0.00	1.98 (19)

Errors show 1 parameter 90% confidence level.

† Absorption component was not included because from previous observations it is suggested that LAC window's absorption is dominant.

‡ Abundaces except Fe, Si, S, Ar, and Ca were fixed to 1.

that the continuum extends up to 20 keV. The upper limit for the equivalent width of Fe-K line is reduced to 120 eV.

The single-temperature NEI model survived the fitting. The largest difference between the NEI model and the rejected thermal bremsstrahlung model is the existence of strong Si and S K-lines around 2 keV: these lines enhance the low-energy side of the model. Becker et al. (1980), however, showed that the Si-K line in the brightest rim is significant only at the 2 σ level with SSS, which has sufficient energy resolution to distinguish the line from the continuum. The energy resolution of the LAC is poor compared to SSS, and is insufficient to recognize these lines. Therefore, we suggest that the NEI model is probably unsuitable.

Chapter 7

SN1006 Study with ASCA

7.1 Observations

We observed SN 1006 with ASCA on 19 August 1993 and 13 September 1993 during the PV (performance verification) phase, pointing at the center and the north-east rim of the remnant, respectively. Table 7.1 gives the coordinates and the attitude parameters, and table 7.2 gives the telemetry modes used in the observations. In these observations, no additional lower discriminator for SIS was set because the number of hot pixels due to the radiation damage was smaller than that of the telemetry saturation level. The Bright mode for Bit_Med was used to avoid the possible telemetry saturation. The Bit_Low mode was used only while the Earth occulted the target; therefore, no Bit_Low X-ray data exist.

7.2 Data Reduction

7.2.1 Data Filtering

The data were selected using the following indicator; cut off rigidity (COR), the earth elevation (ELV_MIN) and the radiation belt monitor count rate (RBM_CONT). In addition the following parameters were used for the SIS data selection criteria: the elevation angle from the bright earth

Table 7.1: The coordinates of SN 1006 ASCAobservations.

ID	Pointing Center	Mean Euler Angle	Observation date
Center	(225.700, −41.930)	(−133.9237, 131.8816, 162.1723)	19–20 August 1993
NE	(225.880, −41.773)	(−133.7396, 131.7557, 155.9022)	13–15 September 1993

The coordinates and the Euler angles are in J2000.0 system.

Table 7.2: The telemetry modes of SN 1006 ASCA observations.†

Bit Rate	GIS mode	SIS mode	
High	PH nominal (10–8–8–5–0–1)‡	4CCD	Faint
Med	PH nominal (10–8–8–5–0–1)‡	4CCD	Bright
Low	PH nominal (10–8–8–5–0–1)‡	4CCD	Bright

†: Both observations used the same arrangement.

‡: Telemetry bits for pulse height, X position, Y position, rise time, light spread and timing informations.

Table 7.3: The event selection criteria for SN 1006 ASCA observation.

	SIS0	SIS1	GIS2/3
COR	> 6	$> 6 >$	> 7.5
RBM_CONT	< 275	< 275	< 275
ELV_MIN	> 10	> 10	> 6
BR_EARTH	> 30	> 20	—
T_DY_NT	$> 4, < 0$	$> 4, < 0$	—
T_SAA	$> 4, < 0$	$> 4, < 0$	—

(BR_EARTH), the time after day-to-night/night-to-day transition (T_DY_NT) and the time after the South Atlantic Anomaly (usually called SAA) (T_SAA). These, respectively, are good indices for the earth light leakage through the optical blocking filter, the rapid change of the dark level due to the light leakage and the non-X-ray event from the short-lifetime radio isotopes activated in the SAA, which change the ratio of the event grade. Table 7.3 gives the criteria used in the selections, and table 7.4 gives the resultant exposure time for each observation and data mode. The exposure time for SIS is shorter than GIS mainly due to the more severe BR_EARTH selection. The event selection and the analysis below were performed on Unix workstations with the FTOOLS and XANADU packages released from the NASA Goddard Space Flight Center.

To improve the statistics, we converted the SIS Faint mode data to the Bright mode data format and treated the mode and pointing data as one data set for each region.

7.2.2 Data Combining

For the usual analysis, we observe the target with one satellite attitude and analyze the data set using the response function with the relevant detector position. In the present analysis, however, we observed the target with two attitudes and accumulated the data from different detector positions.

Table 7.4: The exposure times of SN 1006 ASCA observations after the event selection.

	SIS0/1 (Faint)	SIS0/1 (Bright)	GIS2/3
Center	17 ksec	7.5 ksec	35 ksec
NE	13/14 ksec	8.7/6.0 ksec	33 ksec

Since the response function changes with different detector position, we need to reconstruct the effective response function. To make the response function for each combined spectrum separately, we assumed that the surface brightness S_j (here suffix j represents the energy bin) is uniform within each region, which is roughly true for the present data; then we can represent the event number in each pointing and energy-bin as

$$C_{ij} = S_j t_i \Omega_i A_{ij}, \tag{7.1}$$

where C_{ij}, t_i, Ω_i and A_{ij}, respectively represent the counts of X-ray event, the exposure time, the detector area (or solid angle) and the detector efficiency[1], indicating pointing number by the suffix i.

Since the combined spectrum consists of the two independent pointings with two cameras (SIS0/1 or GIS2/3), the number of the data set is 4: $i = 1$ to 4. Thus the total count number of the X-ray event C_j is given as

$$C_j = \sum_{i=1}^{i=4} C_{ij} = S_j \sum_{i=1}^{i=4} t_i \Omega_i A_{ij}. \tag{7.2}$$

In other words, we can make the combined response and data as follows:

1. To make the combined data set, we sum all data within the same spectral group.

2. To make the response function, we add the matrix element of the mirror and the detector responses for the relevant spectral data with weights of exposure times and solid angles.

In the analysis below, all GIS data in the same sky region were combined into one spectral file. All SIS data were combined as well.

[1]In practice, the detector efficiency for each pointing data is not given as a vector but as a matrix because the detector has finite energy resolution. However, we simplified the response as explained in the text because the difference does not affect the essence of the discussion.

7.3 Analysis and Results

7.3.1 General property

Since the GIS FOV covered the whole remnant while the SIS covered only a limited region, we first made the GIS image and extracted the GIS spectra for each region. Figure 7.1 shows the vignetting-corrected GIS image with regions where we extracted spectra, and figure 7.2 shows the spectra after subtracting the corresponding CXB spectra extracted from the blank-sky data set supplied from ASCA GOF. The spectra can be divided into two groups; X-ray faint regions, including NW and SE edges, where strong lines of Mg, Si and S were found (hereafter referred to as "Interior"), and X-ray bright NE and SW rims with continuums extend to higher energy than the former regions and show no strong line (hereafter referred to as "Rim"). The former provides the first detection of the emission lines from SN 1006, hence gives clear evidence that the emission from the whole remnant is of thermal origin.

Background Estimation

Since the Interior emission is extended and very faint compared to the Rim, we have to consider three background components for the Interior data set: CXB (blank sky), the local background (coming from the Lupus Loop) and the leak from the strong Rim component. While the first two should be considered in any observation or analysis, the third is an issue for the ASCA XRT, whose PSF has a sharp peak but with a widely-spread tail (see the encircled energy function shown in figure 5.14). The leakage is not a matter unless the neighboring source is strong. In the present case, however, the bright Rim is far stronger than the other backgrounds below 5 keV. Figure 7.3 shows the model spectra of the leak and the local components detected by Ginga with the blank-sky data corresponding to the Interior regions; the leak component is computed using the XRT response, and the local component using the spectral parameter obtained in the Ginga analysis. In case of the ASCA Interior data, the local component is negligibly small compared to the CXB or the large contribution of the leak component, hence we did not include it in the relevant background.

As the first step of the background estimation, we simulated the leakage spectrum for IN1 and IN2 using the response matrix of the XRT which describes the efficiency at any point on the focal plane for X-rays coming from a certain direction.

The leak component of the simulated-BGD for each region is obtained as follows:

1. We made the mirror response, where the source image is of the Rim-component and leakage is integrated over the regions of the IN1 and IN2. The response was made for GIS to create

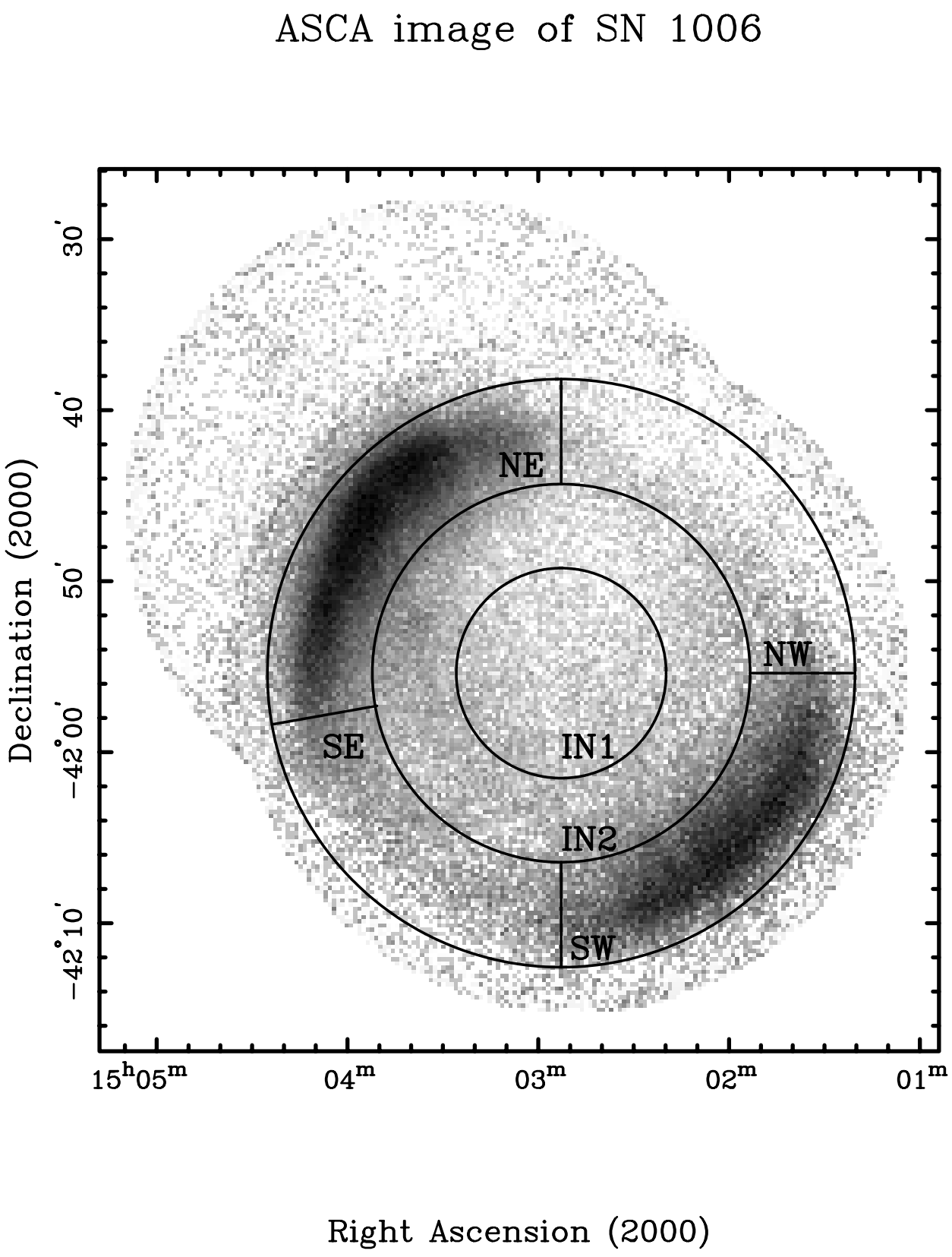

Figure 7.1: The vignetting-corrected image of SN 1006 with regions where we extracted spectra.

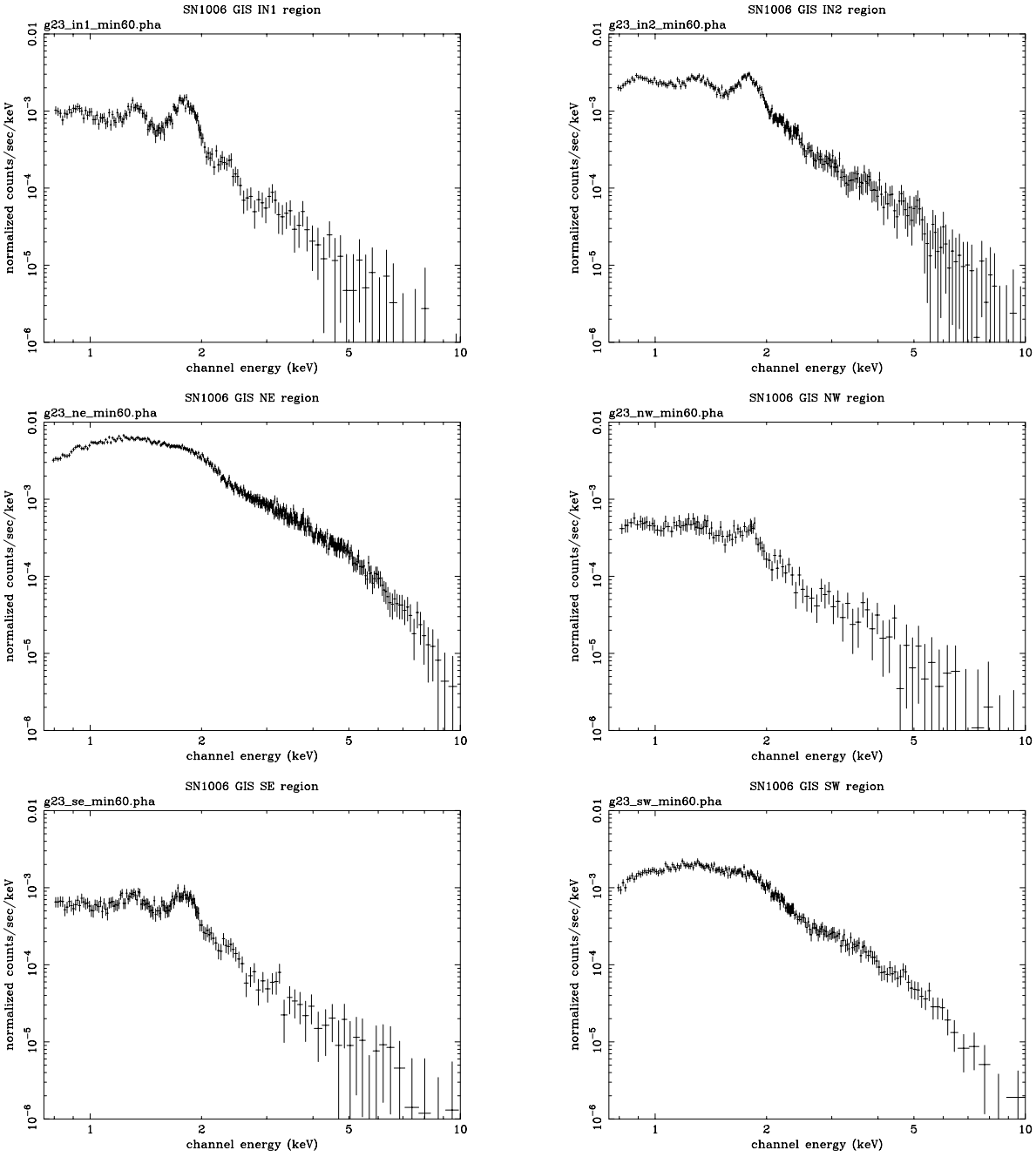

Figure 7.2: Spatially resolved GIS spectra of SN 1006. Each panel corresponds to the region shown in Fig.7.1. From each spectrum, non-X-ray backgrounds of the corresponding detector position and the blank-sky components were subtracted.

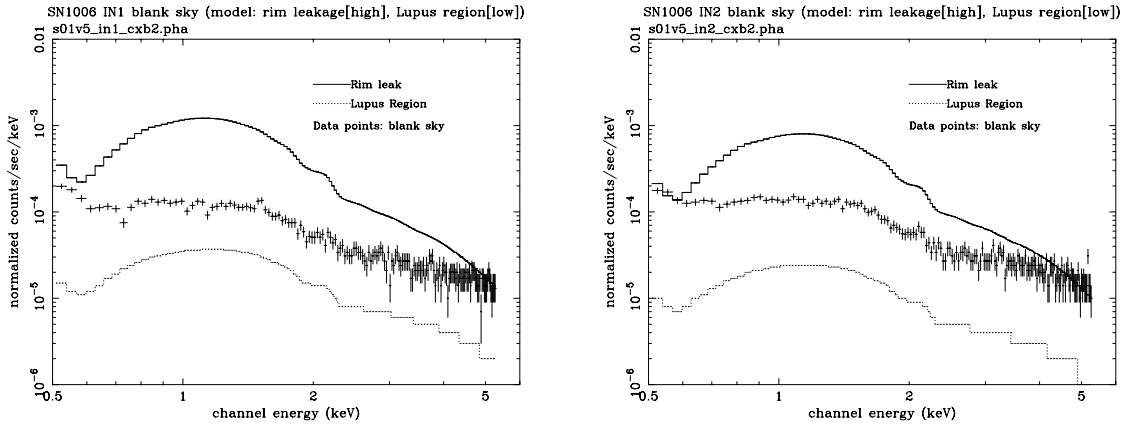

IN1 IN2

Figure 7.3: The model spectra of the leak component and the local component detected by Ginga with the blank-sky data for each region. In each panel, the model with larger flux is the leak component and the weaker one is the local component.

the large-area source image. Since each region data set consists of multiple pointings and detectors, the responses were made separately for each component.

2. We made the simulated spectra with the same exposure time as the observation using the responses above.

3. We combined the fake spectra in the same manner as the observation data.

4. We made the spectral model for reproducing the combined fake data using the response for the observation. The fitted model is a power-law with an interstellar absorption using the Rim analysis results.

Figure 7.5 shows the simulated leak-components with the Interior spectra after the subtraction of the blank-sky data. It can be seen from that spectral *shapes* at > 3 keV seem to fit the data; however, the models are stronger than the data in the same band. It may be attributed to the facts that the GIS image is different from the true source image due to the convolution by XRT PSF and that the response can only be calibrated precisely near the focal point for any direction. Thus, we gave up using simulated backgrounds.

As an alternative method, we described the background from the raw data of the SIS BG region, which is located opposite to the Interior region with the NE rim as the symmetry axis. (figure 7.4). Fortunately, the leakage spectra vary little between different position because the loose PSF comes from the geometrical strain of the mirror surface. Therefore, we can expect that contamination photons have similar spectra to that of the off-source region.

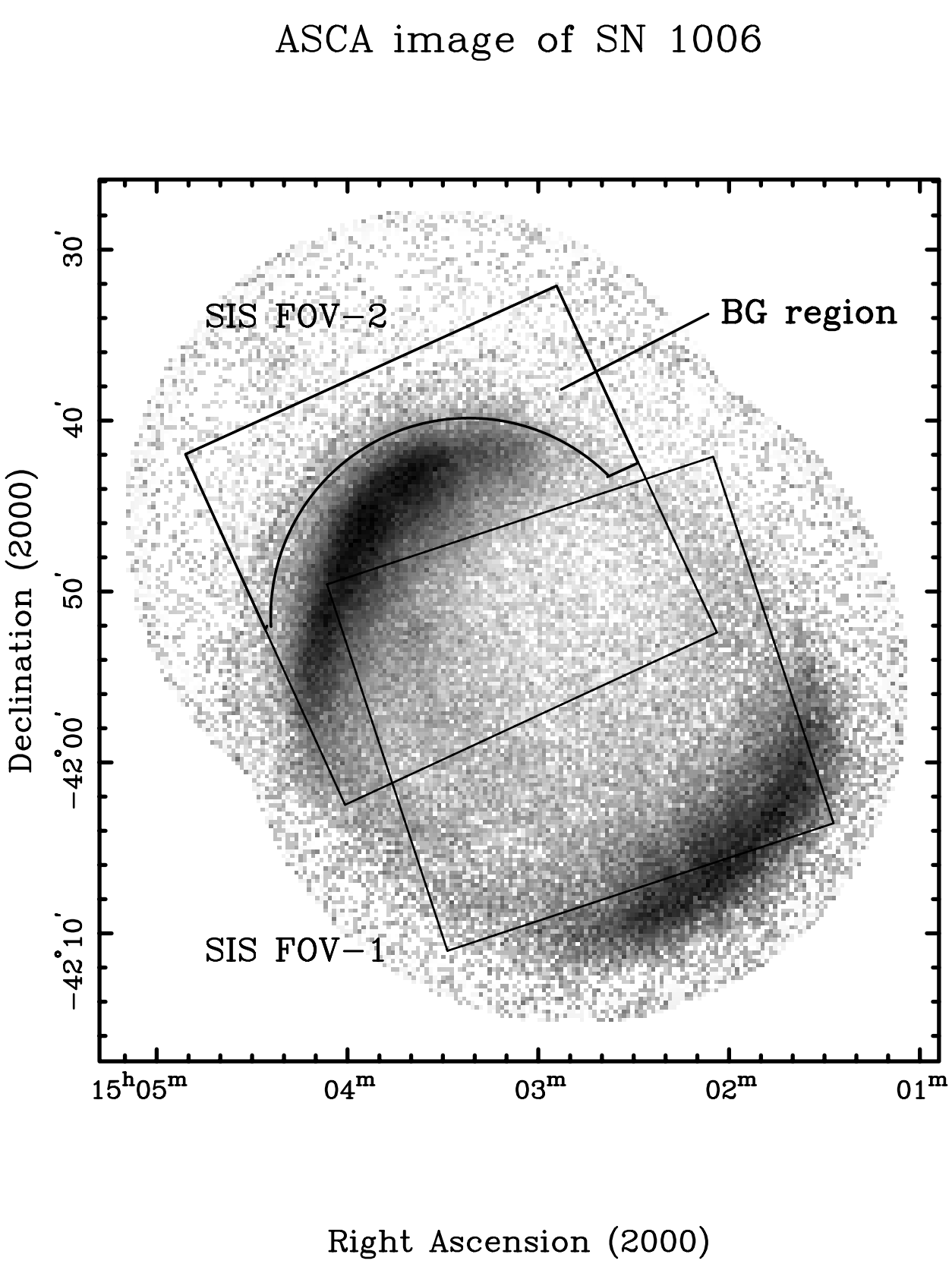

Figure 7.4: The region used for the background estimation with GIS image.

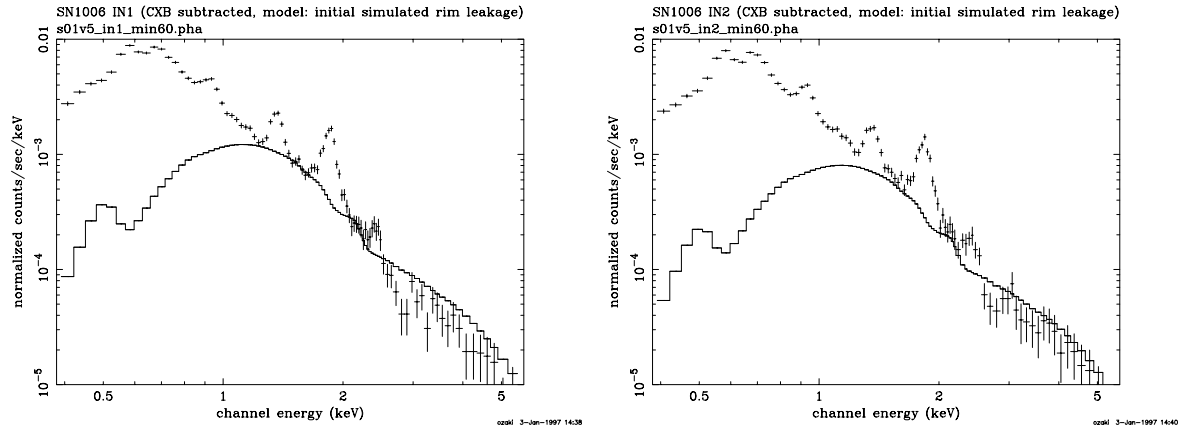

IN1 IN2

Figure 7.5: The simulated Rim-leak components and the Interior data after the subtraction of the blank-sky components. The models above 3 keV represent the spectral shape, but its flux exceeds the data. In the actual fittings, we renormalized the model to the > 3 keV data points in each region.

As the fitted-BGD model, we used a Raymond-Smith plasma with the solar-abundance and a power-law continuum: figure 7.6 shows the spectra with the best-fit model. For the fitting, we used the 0.8–5 keV band for the SIS0, 0.5–5 keV for the SIS1 and 0.8–10 keV for the GIS data; the 0.5–0.8 keV for the SIS0 data were excluded because they are polluted by the optical-light leakage. The > 5 keV SIS data were excluded due to the intrinsic background limit. The best-fit values of the temperature and the photon index are $kT = 0.19 \pm 0.01$ keV and $\Gamma = 2.24 \pm 0.05$, respectively (with reduced-$\chi^2 = 1.083$ for 312 d.o.f.). The power-law index represents the composition of the CXB with a photon index of $\simeq 1.5$ and the leakage of the Rim emission of the index $\simeq 3$. The Raymond-Smith can be interpreted as the leak of the Interior component judging from its temperature and the surface brightness.

The uncertainty in the normalization still remains. Since the Interior spectrum is thought to be of thermal origin, we can expect that the harder data points are mainly from the leakage and CXB. Therefore, we normalized the leakage with data points of higher energy as follows.

We determined the energy range for the estimation as follows:

1. In order to estimate the contribution of the thermal component to the Interior data points, we fitted the data set with a NEI model for each region. The results are, of course, statistically unacceptable, but we can estimate the 90% error of the temperature from the best-fit parameter.

2. With the model of the 90% upper-limit temperature, we determined the energy where the

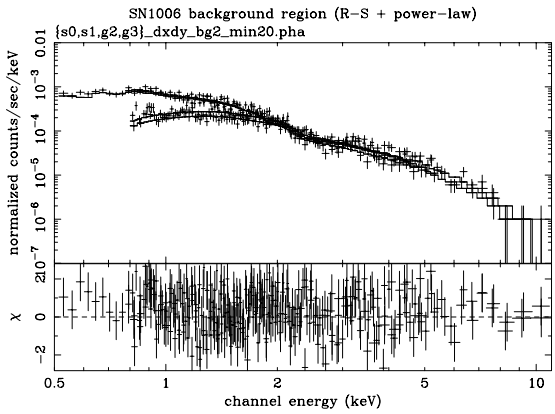

Figure 7.6: The BG region data and the 'fitted BGD' model.

Table 7.5: Best-fit parameters for GIS NE- and SW-rim fittings. The applied model is power-law with an interstellar absorption.

Region	$N_{\rm H}$ [10^{21} cm^{-2}]	photon-index	reduced-χ^2 (d.o.f.)
NE	$1.69^{+0.18}_{-0.19}$	$2.91^{+0.03}_{-0.04}$	1.432 (95)
SW	$1.50^{+0.34}_{-0.35}$	2.98 ± 0.07	1.256 (109)

data point becomes 10 times larger than the model. We considered that the data points above this energy is of leakage origin. With IN2 data, the energy becomes 3.4 keV. For other regions, we could not estimate the 90% error; the fittings did not converged due to poor statistics. Therefore, we used 3.4 keV as the lower boundary of the BG-fitting for all the regions.

3. We fitted the data points with the background model and determined its normalization.

For the bright rims, we subtracted only the CXB component because the model above is intended to describe the Rim-leakage.

GIS data

Basically, the two bright rims can be described with a power-law with an interstellar absorption model. Table 7.5 gives the best-fit parameters with 90% errors and figure 7.7 shows the best-fit models with data. While two rims are spatially separated from each other, their slopes are similar. The residual shows weak Si and S lines which implies that there is a thermal plasma or the power-law shape is of thermal origin. We will analyze this further in section 7.3.3 using the strength of lines with SIS data.

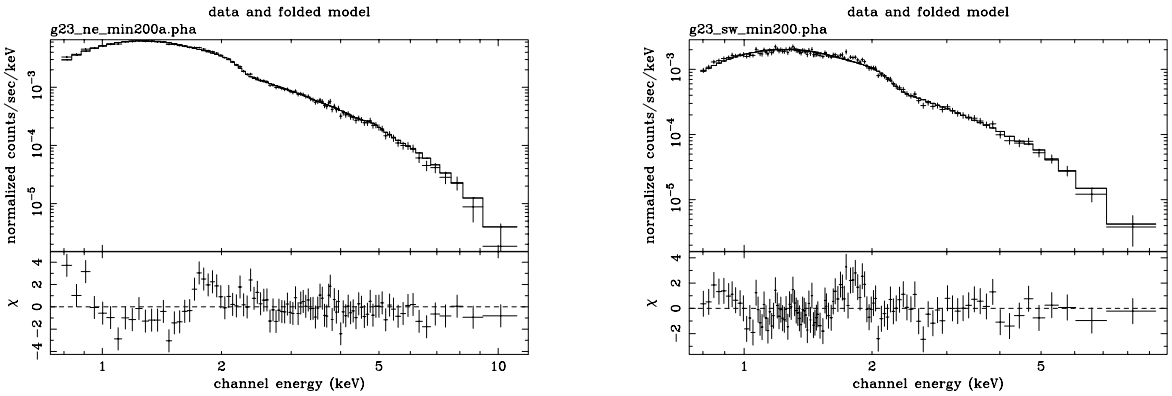

Figure 7.7: GIS spectra of two bright rims with best-fit power-law models. In both regions, continuums can describe the data points well, but Si and S line structures remain.

Table 7.6: Best-fit parameters for GIS thermal-region fittings. The applied model is a thermal bremsstrahlung continuum with He-like Ne, Mg, Si and S lines. Since the energy resolution of GIS is broader than that of SIS, each element can be described with one line in contrast to the SIS spectrum (see table 7.7).

Region	kT [keV]	Ne [keV]	Mg [keV]	Si [keV]	S [keV]	Reduced-χ^2 (d.o.f.)
IN1	0.37	0.883	1.321	1.794	2.309	1.225 (44)
IN2	0.50	0.883	1.296	1.781	2.277	0.8931 (106)
NW	0.21	0.877	1.265	1.762	2.288	0.5243 (19)
SE	0.86	0.853	1.300	1.781	2.369	1.224 (30)

The Interior GIS data cannot be described with a thermal bremsstrahlung continuum with He-like Ne, Mg, Si and S; line centers of the data set are lower than the model in each region. Thus, we assumed line centers as free parameters and re-fitted them. Table 7.6 shows the best-fit parameters and figure 7.8 shows the best-fit models with data. The degrees of ionizations of for Ne, Mg, Si and S are like Li-Be, Be-N, Be-O and Heβ-like-Si, respectively. This may indicate a difference in the ionization between different atomic numbers or a systematic error of the response matrix. We will analyze this further in section 7.3.2 with SIS data.

7.3.2 Interior emission

For the SIS analysis, we extracted a bright-rim data set and two Interior sets whose regions correspond to the GIS data sets in section 7.3.1. Figure 7.9 shows the regions where we extracted the SIS data sets.

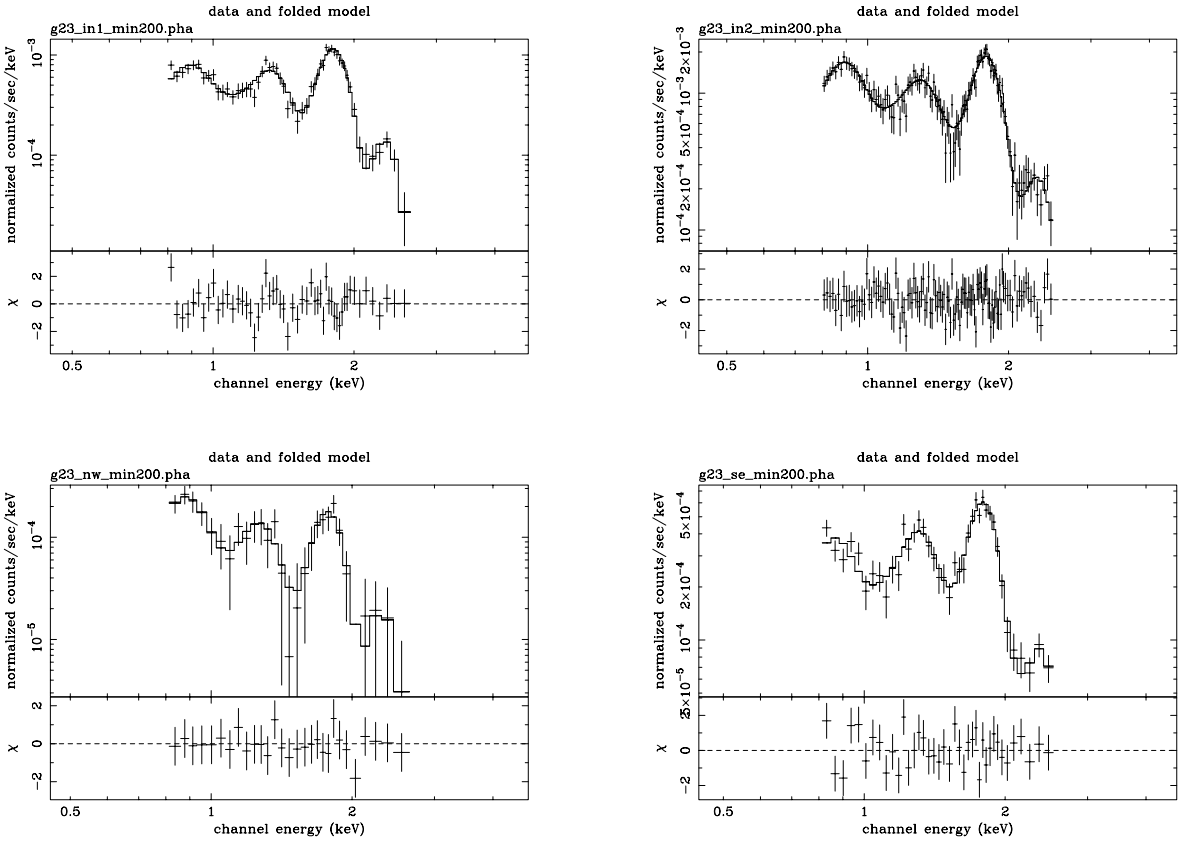

Figure 7.8: GIS spectra of thermal regions with best-fit thermal bremsstrahlung and line model. In each fitting, data points above 2.6 keV were ignored because they were so near the background level that statistical errors are too large for fitting.

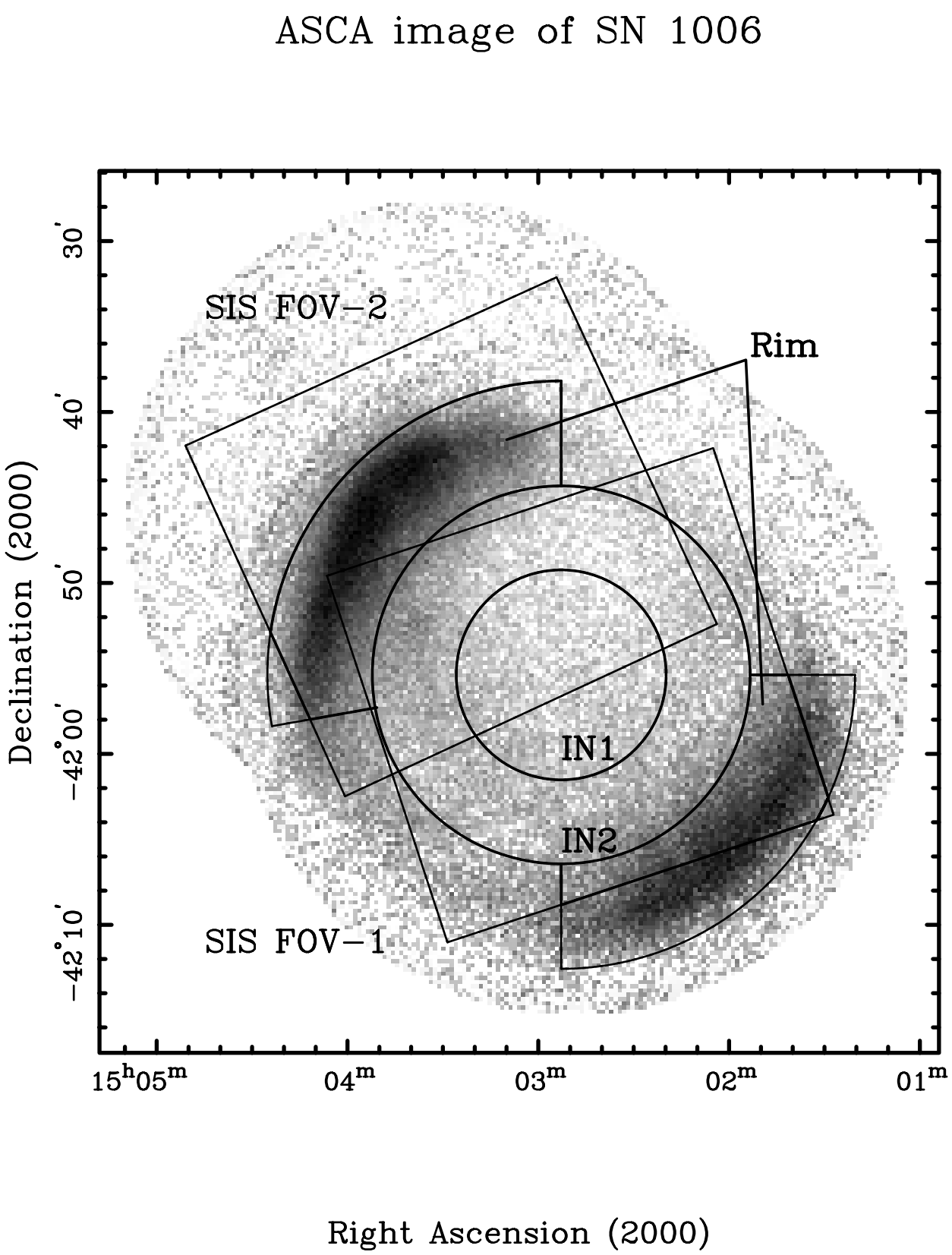

Figure 7.9: The GIS image and the integrated regions for the SIS analysis. For the Rim analysis, two bright-rim data sets were combined into one because the SE rim region (see figure 7.1) inside SIS FOV is too small for independent fitting.

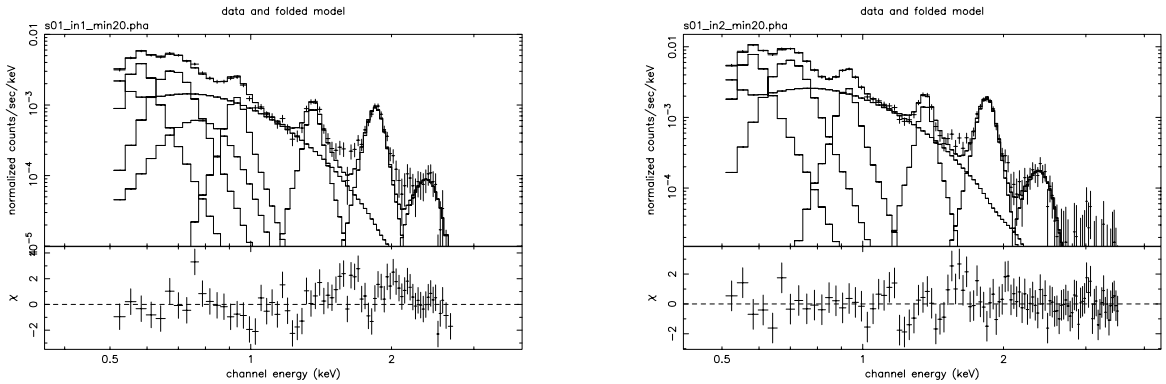

Figure 7.10: SIS spectra of IN1 and IN2 region with best-fit thermal bremsstrahlung and Gaussians models. The Gaussians included are He- and H-like O and low-ionized Ne, Mg, Si and S. In addition, broad-width Gaussian around 0.7 keV is added for IN1 model in order to describe the $\simeq$ 0.7 keV structure. This structure is thought to be a Fe-L complex, and described with NEI-plasma model in figure 7.12. These fittings were done for the estimation of the SIS energy scale.

For Interior fits, we subtracted CXB data supplied from GSFC and the leakage background model from the data sets.

For the Interior model, we first tried a thermal bremsstrahlung model with Gaussians to see the basic spectral feature. Figure 7.10 shows the SIS spectra with best-fit models, and table 7.7 gives the best-fit parameters. Lines lighter than Mg show higher center energy than the lab-value, and Si and S lines show significantly lower center energy. The former can be basically explained with the error of the response matrix because the shift is systematic and below the guaranteed value. The H-like oxygen K-α line shift is significantly larger than others and the line has larger width than others; it is thought to be due to the contamination of Fe-L lines. By contrast, Si and S peaks are much lower than the He-like K-α lines. This suggests that their ionization state is lower than the thermal equilibrium condition.

Judging from the systematic shift of the low-energy lines, we shifted the response matrix 5 eV, which is the lowest value of the shifts, for the IN1 and IN2 analysis described below.

As the next step, we tried an NEI plasma model because the lines suggested less-ionized plasma. However, this model could not describe spectra well; the model could not describe the widths of Si nor S lines, nor the <1 keV profile. Figure 7.11 shows spectra with best-fit models and table 7.8 gives the best-fit parameters. As the fitting gave unreasonable results, we did not evaluated errors. Two-component NEI might describe this data, but we gave up the fittings because two models interfered with each other in the fittings, and we could not find the best-fit point with reasonable errors or acceptable χ^2 values.

Table 7.7: Best-fit parameters for first-tried SIS Interior fittings. The applied model is a thermal bremsstrahlung continuum with Gaussians that describe He- and H-like O and low-ionized Ne, Mg, Si and S. The Gaussian energies are $\simeq$ 50 eV higher than those of GIS but still lower than He-like ions: this may imply that GIS energy scale has inaccuracy that make discussions of the ionization state impossible.

Region	kT [keV]	O VII [keV]	O VIII [keV]	Ne [keV]	Mg [keV]	Si [keV]	S [keV]
		σ [eV]	σ [eV]	σ [eV]	σ [eV]	σ [eV]	σ [eV]
IN1	0.31	0.580	0.686	0.928	1.360	1.845	2.369
		0	38	0	0	39	105
IN2	0.26	0.580	0.691	0.925	1.365	1.854	2.346
		0	41	0	0	40	102

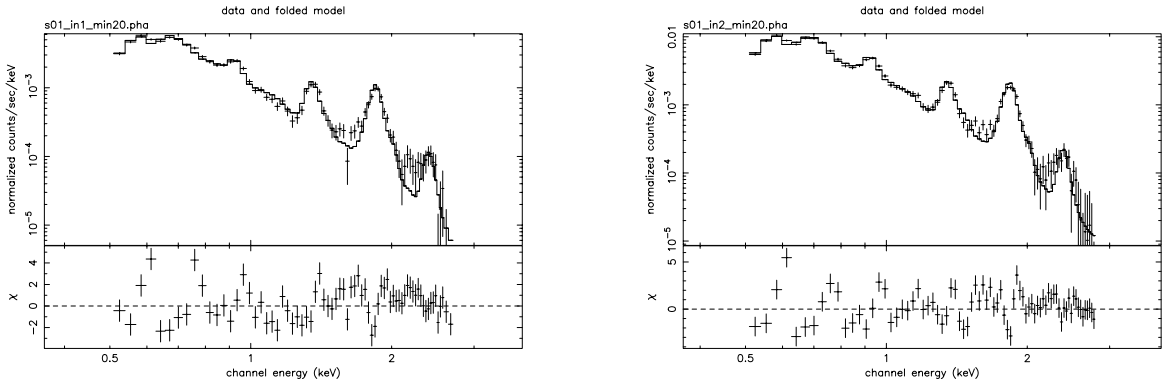

Figure 7.11: SIS spectra of IN1 and IN2 region with best-fit single-component NEI-plasma models. In spite of the introduction of the shift of the energy scale, the model could not describe line structures in each region.

Table 7.8: Best-fit parameters for SIS-Interior one-component NEI fittings. As χ^2 values show, this rather simple NEI model is clearly rejected for both spectra.

Region	kT	$n_e t$	O	Ne	Mg	Si	S	Fe	Reduced-χ^2
	[keV]	[log cm^{-3}s]			[solar abundance]				(d.o.f.)
IN1	0.82	9.89	1.5	1.3	4.6	25	35	3.2	2.775 (64)
IN2	0.99	9.71	1.1	1.1	3.8	21	23	8.1	2.902 (69)

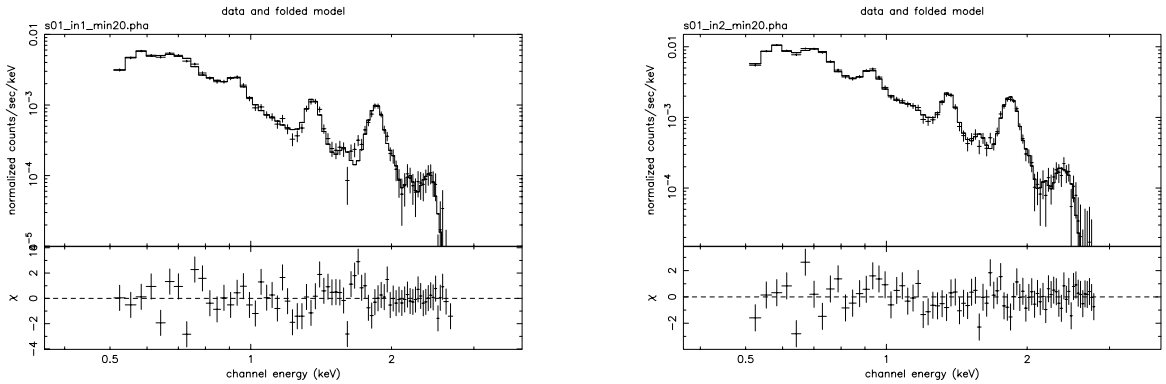

Figure 7.12: SIS spectra of IN1 and IN2 region with best-fit Gaussians and NEI-Fe plasma (see text). In these fittings, Fe-L complex and H-He continuum are described with NEI plasma, and other lines (table 7.9) are introduced separately.

For further analysis, we added lower-ionization lines around Si and S, in addition to the thermal bremsstrahlung and He-like line components above Ne K-α energy. Below this energy, we introduced the NEI code developed by Masai (1989) in addition to He- and H-like O lines only to obtain fits for the Fe-L profile because the energy resolution is not high enough to distinguish each Fe lines. Figure 7.12 shows the final results of the ad-hoc model fit and table 7.9 gives the best-fit parameters. While we did not take the Fe-K line into account in this fit, the best-fit Fe-K strength is consistent with observations — the model predicted much lower strength than the background level.

As the background is uncertain, we did not proceed to analyze this any further.

7.3.3 Rim emission

For the bright rim, we combined two rims into one because SW rim lies at the edge of the SIS FOV so that the statistics of the data sets are too poor to discuss the spectrum precisely, and because it was implied from the GIS analysis that the two rims have similar spectra, except for their strength.

Spectrum

If the whole emission of SN 1006 is due to an NEI plasma, the Rim region should show stronger equivalent widths of lines than elsewhere. This is because the stronger continuum of the NE and SW rims than the NW and SE edges but with similar geometry indicates that higher-density plasma prevails in the bright Rims. Consequently, the ionization of heavy elements goes faster, hence gives stronger equivalent widths of emission lines than elsewhere. This prediction is, however, completely opposite to the observations. Thus, we suggest that the Rim emission is essentially of a non-thermal

Table 7.9: Best-fit parameters for SIS-Interior Gaussians and NEI-Fe plasma model (see text). In these fittings, Fe-L complex and H-He continuum are described with NEI plasma, and other line energies are fixed. Since the spectra have insufficient quality to study Fe-L lines in NEI condition, we estimated only best-fit values for Fe abundances and ionization parameters in both fittings.

			Region	
	(unit)	(Energy [keV])	IN1	IN2
kT(keV)	[keV]		0.24 ± 0.02	$0.27^{+0.03}_{-0.01}$
Emission measure	[10^{52} cm^{-3}arcmin^{-2}]		$8.2 \times (\frac{D}{1\mathrm{kpc}})^2$	$9.6 \times (\frac{D}{1\mathrm{kpc}})^2$
nt(s/cc)	[log cm^{-3}s]		10.4	9.87
Fe abundance	[solar abundance]		0.94	56
O-Kα (He-like) E.W.	[eV]	0.574	520^{+70}_{-60}	540^{+60}_{-40}
O-Kα (H-like) E.W.	[eV]	0.654	260 ± 30	190^{+30}_{-20}
Ne-Kα (He-like) E.W.	[eV]	0.923	180^{+40}_{-30}	180^{+20}_{-30}
Mg-Kα (He-like) E.W.	[eV]	1.352	810^{+110}_{-100}	510^{+50}_{-60}
Mg-Kβ (He-like) E.W.	[eV]	1.580	420^{+160}_{-140}	290^{+80}_{-100}
Si-Kα (B-like) E.W.	[keV]	1.802	$3.9^{+0.9}_{-0.6}$	3.3 ± 0.4
Si-Kα (He-like) E.W.	[keV]	1.865	12^{+2}_{-1}	5.4 ± 0.6
Si-Kα (H-like) E.W.	[keV]	2.006	3.6 ± 1.3	1.2 ± 0.5
Si-Kβ (He-like) E.W.	[keV]	2.183	$5.3^{+2.3}_{-2.1}$	1.4 ± 0.8
S-Kα (O-like) E.W.	[keV]	2.331	11^{+11}_{-9}	6.9 ± 3.2
S-Kα (Be-like) E.W.	[keV]	2.408	< 47	< 11
S-Kα (Li-like) E.W.	[keV]	2.440	< 45	
S-Kα (He-like) E.W.	[keV]	2.460		$5.9^{+5.7}_{-5.2}$
Reduced-χ^2			1.454	0.9335
(d.o.f.)			(56)	(60)

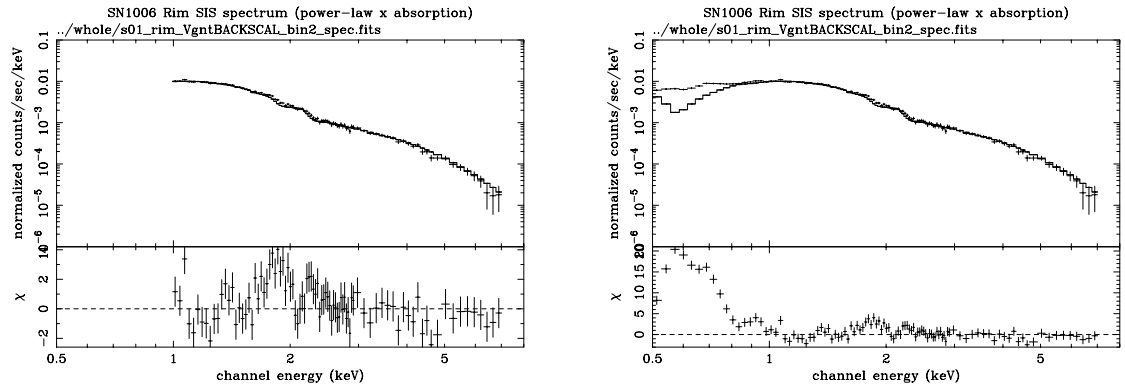

Figure 7.13: The Rim data and the power-law model which is the best-fit for the > 1 keV data. The structures below 1 keV and around 2 keV remain.

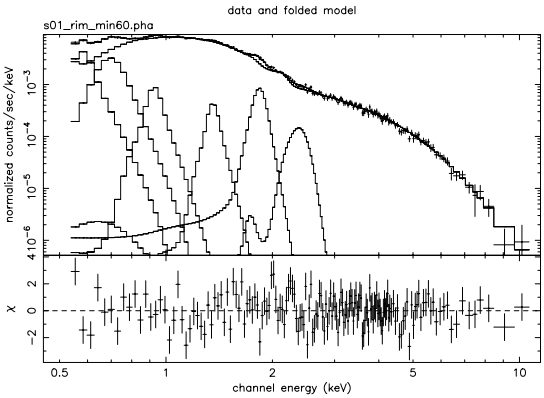

Figure 7.14: The Rim data with the power-law and emission-line model. The structures in Fig.7.13 are reduced or disappear.

origin. Since non-thermal emission generally exhibits power-law spectra, we tried to fit the Rim spectra with a power-law and interstellar absorption. Figure 7.13 shows the best-fit model with the observed data. The model fits the > 1 keV continuum well except for a weak line profile around 2 keV. The model however cannot explain the data at the lower band than 1 keV; the line-like structure remains. The residual structure is similar to that of the Interior spectrum.

To examine it more quantitatively, we compared the count rate of each line between the Rim and the Interior as follows:

1. We extracted the line structure from the IN2 region by fitting a model of a thermal bremsstrahlung continuum plus Gaussians. In contrast to the interior fitting, we did made the width of Gaussians as free parameters instead of introducing many of low-ionization lines.

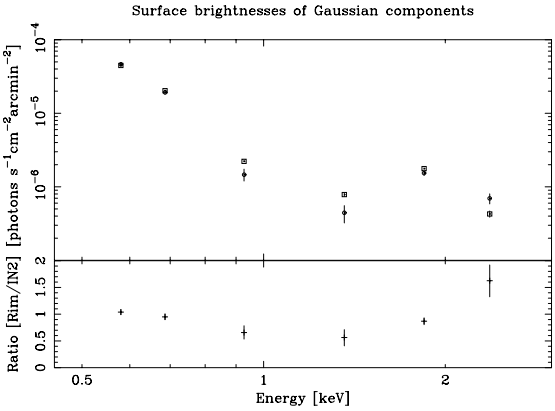

Figure 7.15: The surface brightness of the Gaussians of the Rim and Interior regions. At all energies, the Gaussians of both regions have almost equal surface brightness.

Table 7.10: The center energy, width (σ) and the surface brightness of each Gaussian in the Interior and the Rim regions.

Energy	σ	Rim flux	IN2 flux	Rim/IN2 ratio
[keV]	[eV]	[10^{-7} count s^{-1}cm^{-2}arcmin^{-2}]		
0.580	0	465^{+18}_{-16}	447^{+12}_{-11}	1.04 ± 0.05
0.686	38	193^{+11}_{-10}	203 ± 5	$0.95^{+0.06}_{-0.05}$
0.928	0	$14.6^{+2.8}_{-2.6}$	$22.2^{+1.2}_{-0.5}$	$0.66^{+0.13}_{-0.12}$
1.360	0	$4.42^{+1.12}_{-1.20}$	$7.85^{+0.45}_{-0.47}$	$0.56^{+0.15}_{-0.16}$
1.845	40	$15.4^{+1.0}_{-1.1}$	17.7 ± 0.5	$0.87^{+0.06}_{-0.07}$
2.369	106	$6.96^{+1.06}_{-1.10}$	4.28 ± 0.41	$1.63^{+0.29}_{-0.30}$

2. We then fitted the Rim by a model of a low-energy absorbed power-law plus the Gaussians with the center energies and σs fixed to the Interior values.

The best-fit model is shown in figure 7.14. Table 7.10 shows the center energy, width (σ) and the count rate of each Gaussian in each region, and figure 7.15 shows the best-fit surface brightness of the Gaussians and their ratios between both regions; each ratio is roughly constant from line to line and nearly equal to one. This fact confirms the assumption that the line-structure found in the Rim can be attributed to the Interior plasma.

Therefore, we fitted the Rim data set by introducing the Interior component into the model. As the component, we used the best-fit IN2 model that consists of a thermal bremsstrahlung continuum with Gaussians and Fe-L complex found in the Interior analysis, and let its normalization be the free parameter. As the foreground, we tried two models: a power-law and a thermal Bremsstrahlung

Table 7.11: The best-fit parameters of the power-law and the thermal Bremsstrahlung fits for the SN 1006 SIS Rim data. The soft model in each fittings is the Interior (IN2) component which was introduced to explain the line structure.

Model	$N_{\rm H}$ [10^{21} cm^{-2}]	kT [keV]	photon index	Reduced-*chi*^{2} (d.o.f.)
Power-law	2.27 ± -0.14	—	$2.84^{+0.03}_{-0.02}$	1.321 (159)
Thermal brems.	0	1.87	—	2.143 (159)

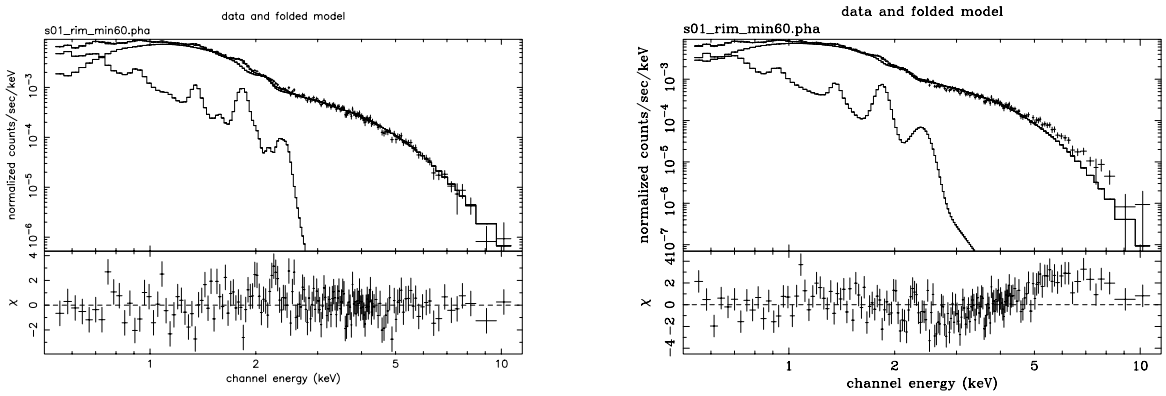

Figure 7.16: The SIS Rim spectrum with power-law (left panel) and the thermal bremsstrahlung (right) continuum and IN2-region model. Although the S-line structure still remains, most of line structures disappears. Nevertheless, the thermal bremsstrahlung model cannot describe the continuum shape.

both with interstellar absorption.

Table 7.11 gives the best-fit parameters with 90% errors and figure 7.16 shows the best-fit model with the data set. It can be seen that the power-law model can represent the data, while the thermal continuum leaves a wavy residual over the whole energy band and is rejected statistically. In contrast to the Interior fittings, the -90% value of the absorption column does not become 0: this implies that the Rim emission becomes flatter at energies below 1 keV.

At the same time, we estimated the Fe K emission equivalent width in the Rim region, and obtained the 90% upper limit of 45 eV at 6.7 keV.

We estimated the flux of the non-thermal emission using the Center pointing GIS data and the Interior-free SIS spectrum. For the GIS data, we used only the > 3 keV band where the non-thermal emission dominates the spectrum; therefore, the photon index is decided by using both the SIS high energy and the GIS data, while the absorption and the normalization are decided by the SIS low energy data and the GIS data, respectively. Table 7.12 gives the best-fit parameters. The whole- and NE-rim parameters were obtained by the data sets of the Center and the NE pointings,

Table 7.12: The best fit parameters for SN 1006 non-thermal component flux estimation. The whole-rim parameters were obtained with both SIS and GIS-Center data, and NE-rim parameter were done with SIS and GIS-NE data.

		whole-SNR	NE-rim
Photon index		2.97 ± 0.03	2.97 ± 0.03
Absorption column density	[cm^{-2}]	$(3.1 \pm 0.1) \times 10^{21}$	$(3.1 \pm 0.1) \times 10^{21}$
Flux (2–10 keV)	[ergs s^{-1}cm^{-2}]	3.4×10^{-11}	1.9×10^{-11}
Flux density at 5 keV	[ergs s^{-1}cm^{-2}keV^{-1}]	3.6×10^{-12}	1.9×10^{-12}
reduced-χ^2 (d.o.f.)		1.072 (590)	1.135 (464)

respectively.

Spatial structure

To discuss the energy source of the non-thermal emission, the spatial structure of the non-thermal emission region may provide the key information. The symmetrical appearance of the region strongly suggests that its three-dimensional structure is of axial-symmetry (see figure 7.17). We therefore examined whether the appearance of the bright rims can be reproduced by the axial-symmetrical structure.

For simplicity, we studied two extreme cases; a barrel structure and a pair of polar-cap structure, both have 0 thickness skin with symmetrical axis perpendicular to the line of sight. We made the surface brightness profiles along three strips: one crossing the remnant from NE to SW, and the other two overlapping the bright rims (figure 7.18), using the vignetting-corrected GIS image of the Center pointing in the 2–4 keV band, where the non-thermal component dominates the emission (actually, Si k-β and S K-α lines esist in 2.0–2.7 keV, but they do not affect the Rim-profile analysis because they are distributed in a wide region while the Rims are spatially confined). We then made models of surface brightness in the same strips taking into account the PSF and compared them with the data. In the models, we assumed a 0-thickness cylinder for the barrel, and 0-thickness disk for the cap. The PSF we used is of the 2.0–3.0 keV energy band and positioned at $\theta = 17.0$ arcmin and $\phi = 39$ deg, which is supplied by the ASCA team. Figure 7.19 shows the employed PSF and its projected profiles along the radial and azimuthal directions of the GIS FOV.

Figure 7.20 shows the NE-SW crossing strip with the simulated profile of the barrel structure whose bottom is normalized to that of the data. It is clearly shown that the rims have quite different brightness from each other, thus the profile cannot be represented by a simple barrel structure. In addition, even if we were to see the NE or SW half of the profile, each peak is far brighter than that

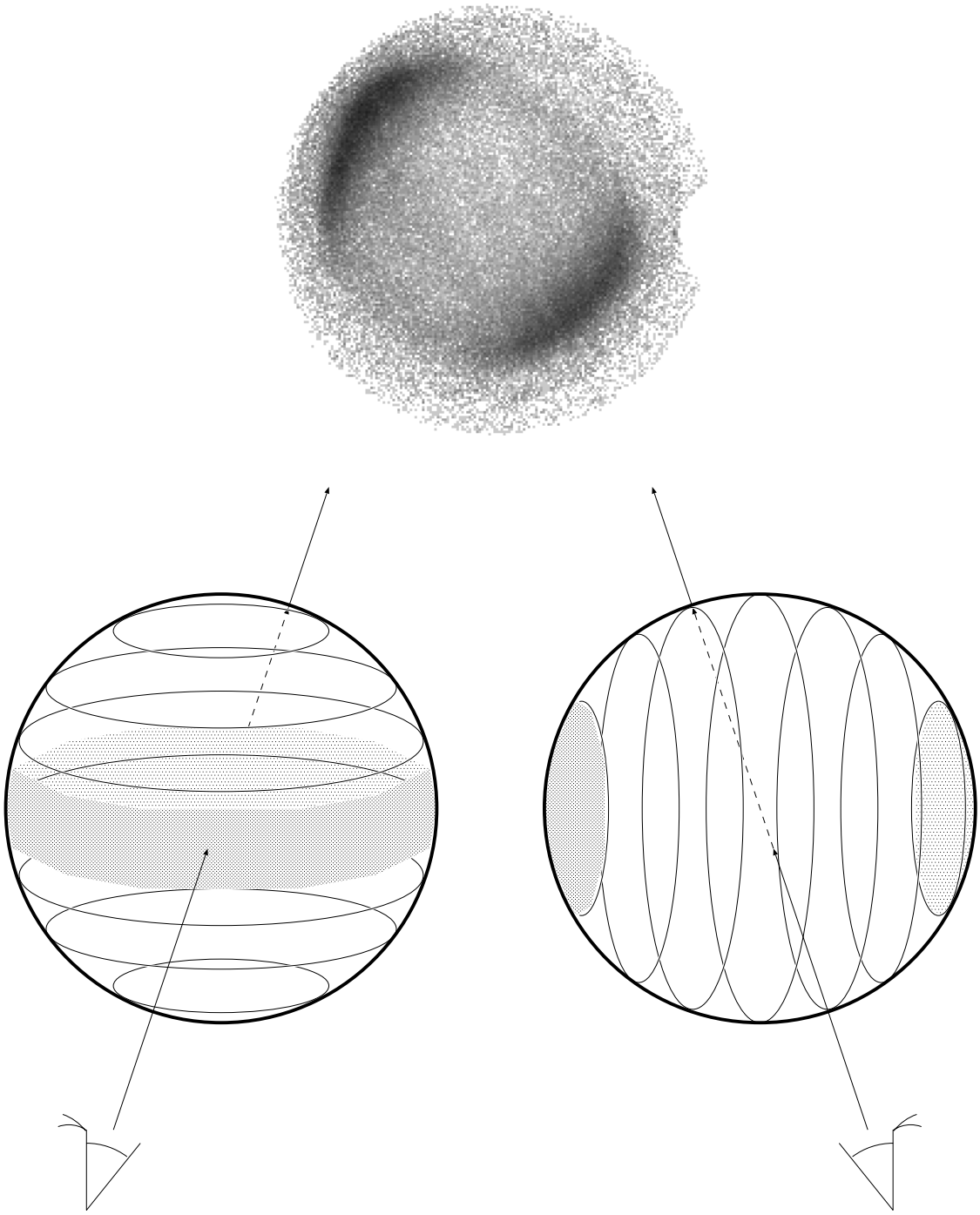

Figure 7.17: Candidates for the 3-D structure which can explain the observed image of SN 1006 qualitatively.

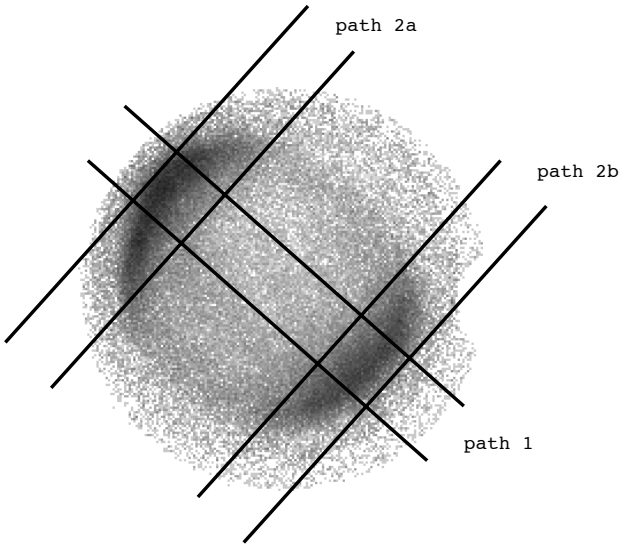

Figure 7.18: Regions where the surface-brightness profiles were made.

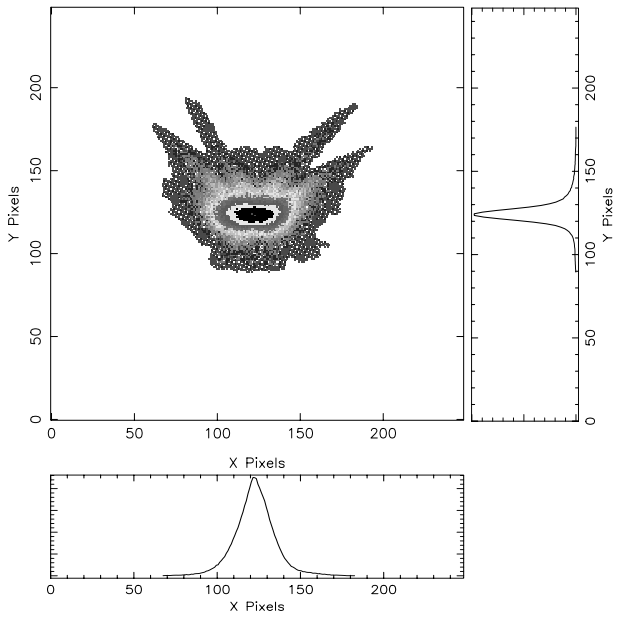

Figure 7.19: The XRT+GIS PSF (17.0 arcmin apart from the optical axis) used in the SN 1006 spatial analysis and the projections along the radial and azimuthal directions. The optical axis is pointed toward the top of the figure.

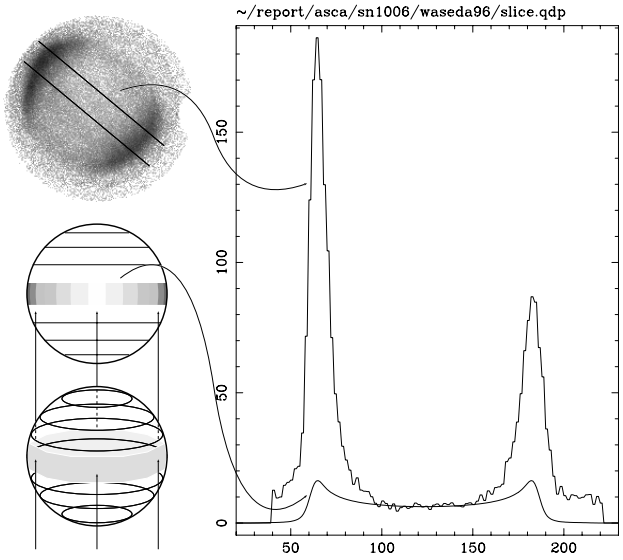

Figure 7.20: The remnant-crossing surface-brightness distribution (path 1) and the simulated profile of the barrel-like structure normalized at the interior of the remnant. It is clearly shown that the rims have quite different brightness from each other and the contrasts between the rim and the interior cannot be represented.

predicted by the model. The polar-cap (actually, the polar-disk) model can represent the outer slopes of each rims. The inner slopes are, however, thicker than the model; therefore, we introduced the disks with finite thickness or thin disks with curvature. In short, the data profile cannot be explained by the projection effect of a thin barrel. However, the profile can be explained by the projection effect by two distinct emitting regions locally confined in the both sides of the remnant.

Apart from the relative flux of the rims, the profile is roughly symmetric with each other. Therefore, it can be explained by the projection of disks with a common center but different emission measures. As the simplest case, we examined whether the profile can be represented by a single disk with an uniform emission measure. Figure 7.21 shows the data and the simulated profiles; it seems that the surface brightness can approximately be explained by this simplest assumption. Since the rims extend along a few pc, they should have fine spatial structure in addition to the disk. The data still cannot be fitted well by the simple model, and perhaps require fine structure in the model. However, the spatial resolution of *ASCA* and the data statistics are not good enough to resolve the finer structure, hence we did not examine more complicated models.

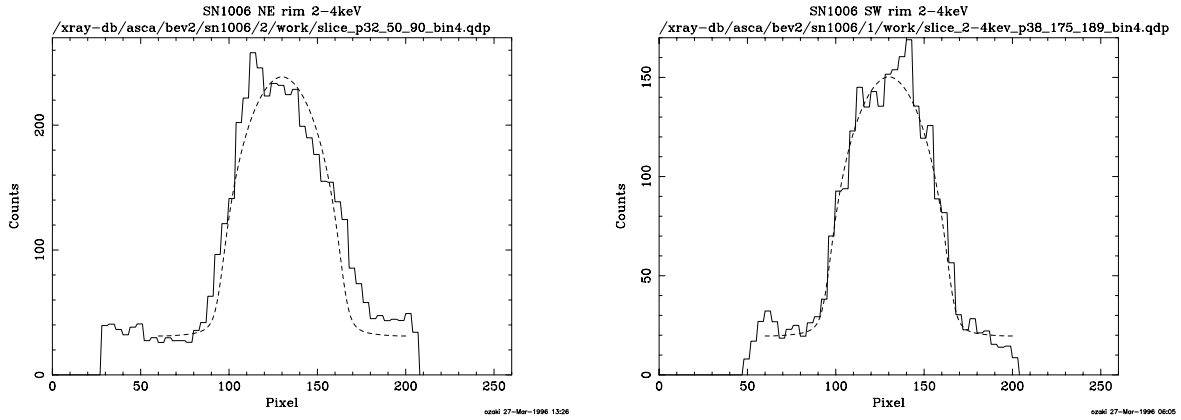

Figure 7.21: The surface-brightness profiles grazing the rims and the emission models from disks of uniform emissivity.

Chapter 8

IC443 Study with ASCA

8.1 Observations

We observed IC 443 with ASCA on 14–15 April 1993 and 9–10 March 1994 during the early PV and AO1 phases, respectively. The former observation pointed the brightest NE subshell of the remnant, and the latter, the SW subshell. Figure 8.1 shows the FOVs of the observations overlaid on the Palomar Observatory Sky Survey image. Table 8.1 gives the coordinates and the attitude parameters, and table 8.2 gives the telemetry modes used in the observations. In these observations, no additional lower discriminator for SIS was set because the number of hot pixels of the radiation damage origin was smaller than the telemetry saturation level. The Bit_Low mode was used only when the Earth occulted the target, hence no Bit_Low X-ray data are available.

Since the PV data of IC 443 were obtained at the very early phase and the spread discriminator (see section 5.2.2) had not been applied yet, the data contains more non-X-ray background events than the late PV and AO observations. There is also a ghost image of the calibration source at the image area. The AO GIS3 data are degraded by the on-board data processing trouble happened on February 10, 1994, between 22:05 and 22:35 UT, after passing through the SAA; the three least significant PHA bits were stuck in the pattern 101, resulting in a loss of digital resolution. Thus, some of the IC 443 GIS data are less qualified and suffered larger background than those of other

Table 8.1: The coordinates of IC 443 ASCA observations.

ID	Pointing Center	Mean Euler Angle	Observation date
PV	(94.1304, 22.4818)	(94.6377, 67.1966, 177.8991)	14–15 April 1993
AO1	(94.1304, 22.4818)	(94.3579, 67.4463, 174.5171)	9–10 March 1994

The coordinates and the Euler angles are in J2000.0 system.

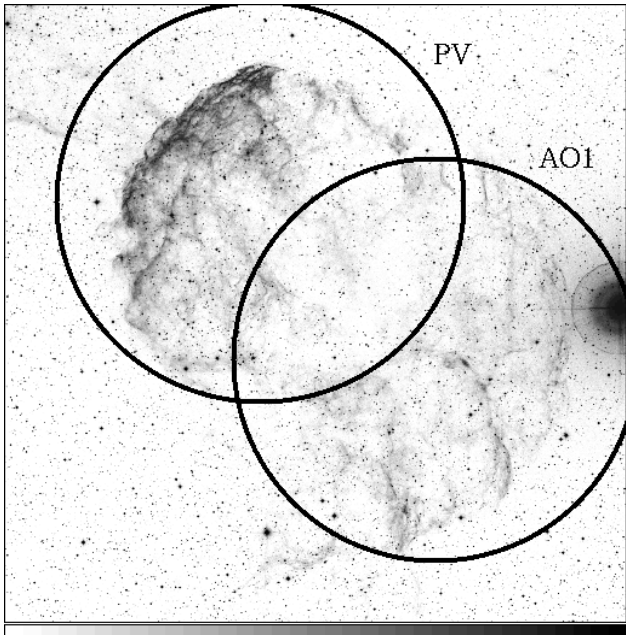

Figure 8.1: The GIS FOV of the IC 443 observations over the Palomar Observatory Sky Survey image.

Table 8.2: The telemetry modes of IC 443 ASCA observations. In both observations, the same arrangements were used.

Bit Rate	GIS mode	SIS mode†	
High	PH nominal (10–8–8–5–0–1)‡	4CCD	Faint
Med	PH nominal (10–8–8–5–0–1)‡	4CCD	Bright
Low	PH nominal (10–8–8–5–0–1)‡	4CCD	Bright

†: In the present analysis, we did not use the SIS data (see text).

‡: Telemetry bits for pulse height, X-position, Y-position, rise time, light spread and timing informations, respectively.

observations such as SN 1006.

8.2 Data Reduction

In this paper, we focus on the study for the large-scale characters of the remnant in order to clarify the spatial distribution of the Ginga hard component. Consequently, we analyzed only the GIS data which cover a larger area and have higher sensitivity in the hard band than SIS.

The data were selected under the same criteria applied to the SN 1006 data, which are described in section 7.2. In short, these are COR > 6, RBM_CONT < 275 and ELV_MIN > 7.5. The resultant exposure time for PV and AO1 observations are 53 ksec and 42 ksec, respectively.

Since the IC 443 pointing have no region which can be used as the background, we used the blank sky fields and night earth data accumulated by the ASCA team as the standard background for the AO1 data analysis. For all the PV data analysis, on the other hand, we have made the blank sky data set accumulated when the spread discriminator was off.

Since the AO1 GIS3 data were degraded by the on-board trouble, we truncated the 2 least-significant energy bits (2 LSB), so that no trouble remain for the spectral analysis.

8.3 Results

8.3.1 General property

Figure 8.2 shows the GIS images of IC 443 in 0.8–10 keV and 4–10 keV bands. While the former appears to have a center-filled morphology, which is similar to the Einstein and ROSAT images, the latter appears as a bright spot and an incomplete semi-circular structure surrounding the NE part of the remnant with a bright bar-like structure at the southern edge of the PV FOV. The positions of the bright spot and the bar-like structure are approximately (06h17m04s, 22d22m)J2000 and (06h18m01s, 22d26m)J2000, respectively.

8.3.2 Hard component

To study the hard component, we extracted the spectra from three regions; the bright spot, the bar-like structure (hereafter, referred to as the hard-spot and hard-bar, respectively) and the whole region.

For comparison of the spectra of the hard-spot and the hard-bar with the soft component prevailing over the whole remnant, we also extracted the spectra of the hard-component-free regions, whose surface brightness in the whole energy band and the distances from the pointing centers are

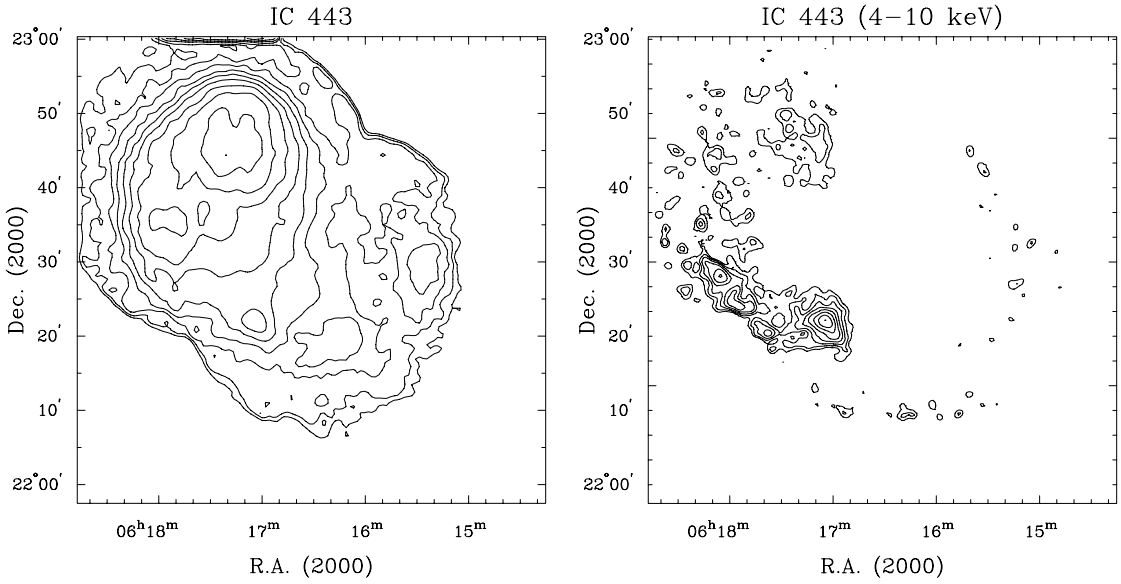

0.8–10 keV band 4–10 keV band

Figure 8.2: The GIS image contours of IC 443 in 0.8–10 keV and 4–10 keV bands. Each panel is drawn in log-scale.

similar to those of the hard regions. Figure 8.3 shows the regions where we extracted the spectra of the hard regions and their backgrounds.

Hard-spot

For the hard-spot, we extracted foreground and background spectra from the AO1 data. Since the foreground spectrum includes local background mainly attributable to the soft X-rays from IC443, we first made the background spectral model using the background data and included it into the foreground fittings. For each spectrum, we subtracted the blank-sky data at the same detector coordinates as the relevant region.

As the local background model, we used a single-component NEI plasma model with the interstellar absorption. The best-fit temperature and the absorption column density were $kT = 1.55$ keV and $N_{\rm H} = 4.8 \times 10^{21}$ cm^{-2}, respectively. Abundances of Mg, Al, Si and S were 1.3, 4.4, 0.7 and 1.0, respectively. The ionization parameter was $\log n_{\rm e}t = 10.7$.

In the foreground fitting, we tried two models; one is a single-component Raymond-Smith plasma and the other is a power-law, both with the interstellar absorption. In the fitting, we fixed all parameters of the local background, except normalization, to those shown above. Both models can describe the data well, hence we could not discriminate these models from the shape of the continuums. Figure 8.4 shows the spectrum and the best-fit power-law model, and table 8.3 gives best-fit parameters for both model. The flux and the flux density of the best-fit power-low

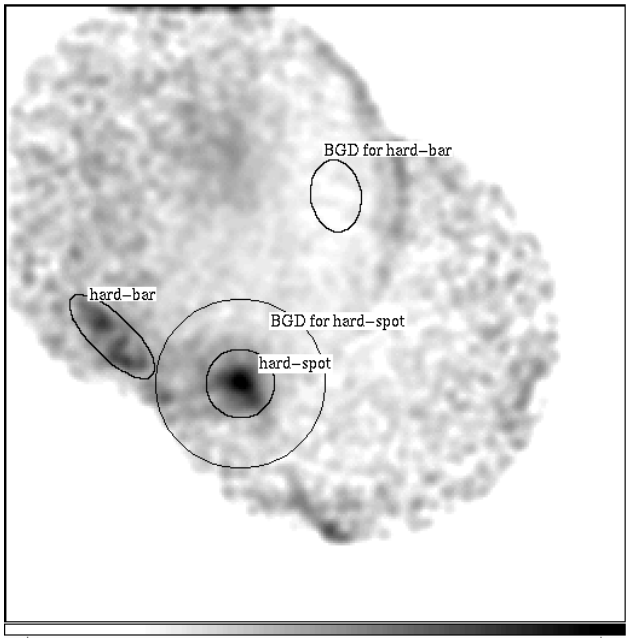

Figure 8.3: The regions where the hard component events and the corresponding local-background (or soft component) events were extracted.

Table 8.3: The best-fit parameters of the IC 443 hard regions spectra.

Region	Model	$N_{\rm H}$ [10^{21} cm^{-2}]	photon index	kT [keV]	Fe [Solar abundance]	reduced-χ^2 (d.o.f.)
hard-spot	Power-law	14 ± 6	2.3 ± 0.2	—	0.9003 (116)	
	R-S	< 67	—	$5.2^{+1.2}_{-0.9}$	< 0.15	0.9379 (115)
hard-bar	Power-law	25^{+19}_{-14}	2.4 ± 0.6	—	—	0.9715 (260)
	R-S	20^{+15}_{-12}	—	$4.2^{+4.1}_{-1.6}$	< 0.8	0.9654 (260)

model are 4.7×10^{-12} ergs s^{-1}cm^{-2} (2–10 keV) and 3.8×10^{-5} photons s^{-1}cm^{-2}keV^{-1} (at 7 keV), respectively.

Hard-bar

For the hard-bar spectrum taken from the PV phase data, we employed the same method for background evaluation as the hard-spot one. The only difference is that the blank-sky data was accumulated from data that had been taken when the spread discriminator was off.

As the local background model, we used an optically-thin thermal plasma containing heavy elements (Raymond-Smith model) with the interstellar absorption. We linked all the abundances of the elements and assumed the ionization equilibrium in order to avoid making the model too complicated compared to the data quality. In contrast to the hard-spot case, the background

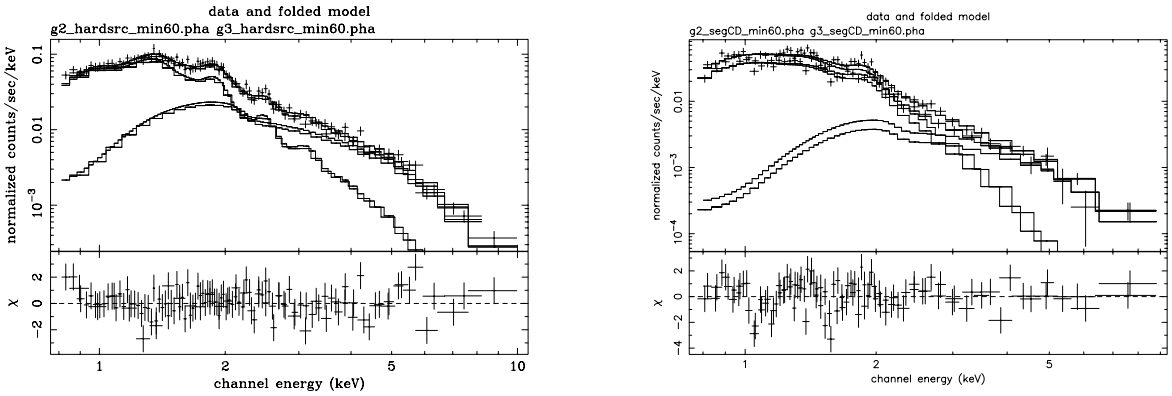

Figure 8.4: The hard-spot (left panel) and hard-bar (right) data with best-fit power-law models and the soft thermal components.

could be described with this rather simple model because of the less accumulated-photon number. The best-fit temperature, abundance and the absorption column density were $kT = 0.66$ keV, $Z = 0.1$ solar abundance and $N_{\rm H} = 4.6 \times 10^{21}$ cm^{-2}, respectively.

As for the spectrum of the hard-bar, which include the local background, we tried the same two models for the hard-spot. Figure 8.4 shows the data and the best-fit models including the local background, and table 8.3 gives the best-fit parameters. The flux and the flux density of the best-fit power-low component are 1.9×10^{-12} erg s^{-1}cm^{-2} (2–10 keV) and 1.2×10^{-9} photons s^{-1}cm^{-2}keV^{-1} (at 7 keV), respectively.

Whole region

Since the position dependence of the response function differs between different energy bands, it is complicated to reconstruct the overall response function for a largely extended emission when the extended source has different energy spectra from position to position. This is the case of IC443 because the soft and hard components exhibit quite different spatial structures with each other, as previously noted.

To estimate the hard component flux from the whole FOV, we accordingly assumed that the surface brightness of the hard component can be described by that of the >4 keV image, because contribution of the soft component almost disappears in that band. Then we reconstructed a response function for the particular purpose of the flux estimation of the hard components from the whole region of the SNR.

We fitted the model consisting of a thermal bremsstrahlung, a power-law and a line of which energy is near 6.5 keV to the > 4 keV band spectrum from PV and AO1 (except for the overlapping

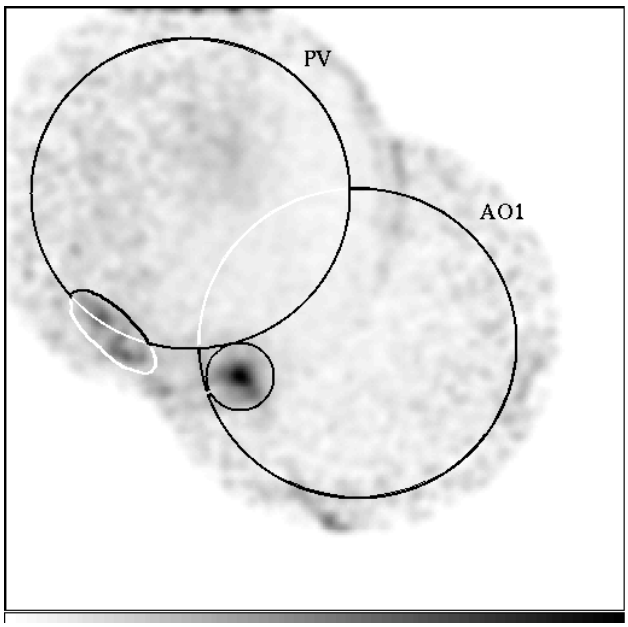

Figure 8.5: The region where we estimated the whole hard-component flux.

PV) region, fixing the temperature and the photon index to the Ginga value reported by Wang et al. (1992). Figure 8.5 shows the regions where we estimated the hard-component flux. The flux density at 7 keV is estimated to be 2.1×10^{-5} photons $s^{-1}cm^{-2}keV^{-1}$ for each region. The equivalent widths of the iron lines of the PV and the AO1 region are $1.33^{+0.51}_{-0.36}$ keV and <63 eV, respectively. The center energy and the flux of the iron line in the PV region are $6.60^{+0.08}_{-0.14}$ keV and $3.4^{+1.3}_{-0.9} \times 10^{-5}$ photon $s^{-1}cm^{-2}$, respectively. Note that we cannot determine the precise flux of the soft components with this particular response function because the response does not reflect the surface brightness distribution of the low-energy band.

8.3.3 Soft component

In the soft component fitting, we did not use the AO1 GIS3 data because the energy bin is not fine enough to use the NEI plasma fitting, due to the instrument trouble.

We divided the PV GIS data into 12 regions as shown in Figure 8.6, and extracted the spectra for each region. For each spectrum, we subtracted the blank sky background at the same detector coordinates as the relevant source region. The surface brightness of the AO1 region is too faint to make spatially sorted analysis with sufficiently small errors to make a comparison of the fitting parameters from position to position. Therefore, we analyzed only the whole AO1 spectrum excluding the PV and hard-spot regions.

As the first step in the fitting, we tried the single-component NEI model for each region with linking all the abundances. Table 8.4 gives the best-fit parameters. While the parameters shows

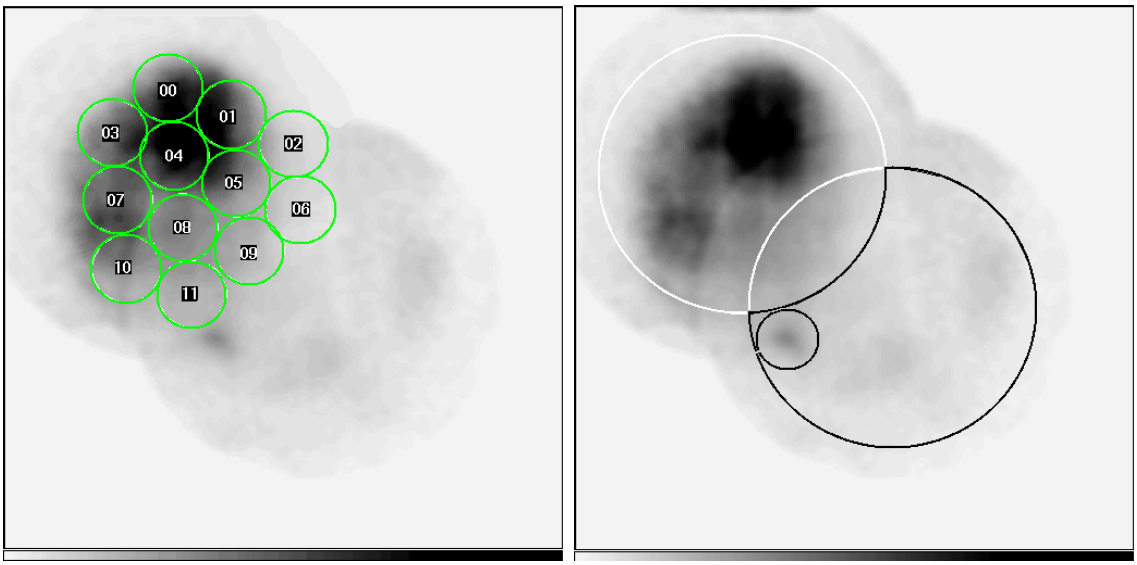

PV data AO1 data

Figure 8.6: The regions where the NEI fittings were performed.

Table 8.4: The best-fit parameters of the abundance-linked NEI fittings for IC 443 PV soft components. As the reduced-χ^2 values show, this model is rejected in bright regions.

Region	kT [keV]	$n_e t$ [logcm^{-3}s]	abundance [relative to solar]	N_H [cm^{-2}]	red-χ^2 (d.o.f.)
00	$1.24^{+0.09}_{-0.07}$	$9.95^{+0.03}_{-0.03}$	$0.66^{+0.1}_{-0.09}$	$0.37^{+0.02}_{-0.03}$	1.219 (164)
01	$1.06^{+0.04}_{-0.03}$	$10.60^{+0.02}_{-0.04}$	$0.45^{+0.04}_{-0.05}$	$0.62^{+0.02}_{-0.03}$	1.495 (205)
02	$1.00^{+0.1}_{-0.09}$	$9.89^{+0.05}_{-0.06}$	$0.55^{+0.15}_{-0.13}$	$0.50^{+0.05}_{-0.04}$	0.9554 (128)
03	$0.87^{+0.06}_{-0.05}$	$9.96^{+0.04}_{-0.04}$	$0.52^{+0.11}_{-0.08}$	$0.42^{+0.04}_{-0.03}$	1.030 (143)
04	$1.06^{+0.04}_{-0.02}$	$9.95^{+0.02}_{-0.02}$	$0.58^{+0.05}_{-0.05}$	$0.56^{+0.02}_{-0.02}$	1.857 (218)
05	$1.14^{+0.03}_{-0.04}$	$9.92^{+0.02}_{-0.02}$	$0.57^{+0.06}_{-0.06}$	$0.64^{+0.02}_{-0.03}$	1.683 (215)
06	$1.11^{+0.14}_{-0.11}$	$9.89^{+0.06}_{-0.06}$	$0.48^{+0.16}_{-0.13}$	$0.52^{+0.06}_{-0.06}$	0.8323 (119)
07	$0.92^{+0.05}_{-0.05}$	$9.89^{+0.03}_{-0.03}$	$0.57^{+0.1}_{-0.09}$	$0.47^{+0.02}_{-0.03}$	1.241 (157)
08	$1.04^{+0.04}_{-0.04}$	$9.88^{+0.02}_{-0.03}$	$0.51^{+0.07}_{-0.06}$	$0.55^{+0.03}_{-0.03}$	1.388 (191)
09	$1.03^{+0.07}_{-0.05}$	$9.81^{+0.03}_{-0.05}$	$0.60^{+0.13}_{-0.1}$	$0.64^{+0.04}_{-0.04}$	1.008 (157)
10	$1.09^{+0.09}_{-0.08}$	$9.81^{+0.04}_{-0.04}$	$0.68^{+0.15}_{-0.12}$	$0.47^{+0.04}_{-0.04}$	1.247 (148)
11	$1.20^{+0.11}_{-0.08}$	$9.78^{+0.04}_{-0.04}$	$0.65^{+0.14}_{-0.12}$	$0.54^{+0.04}_{-0.04}$	1.148 (153)

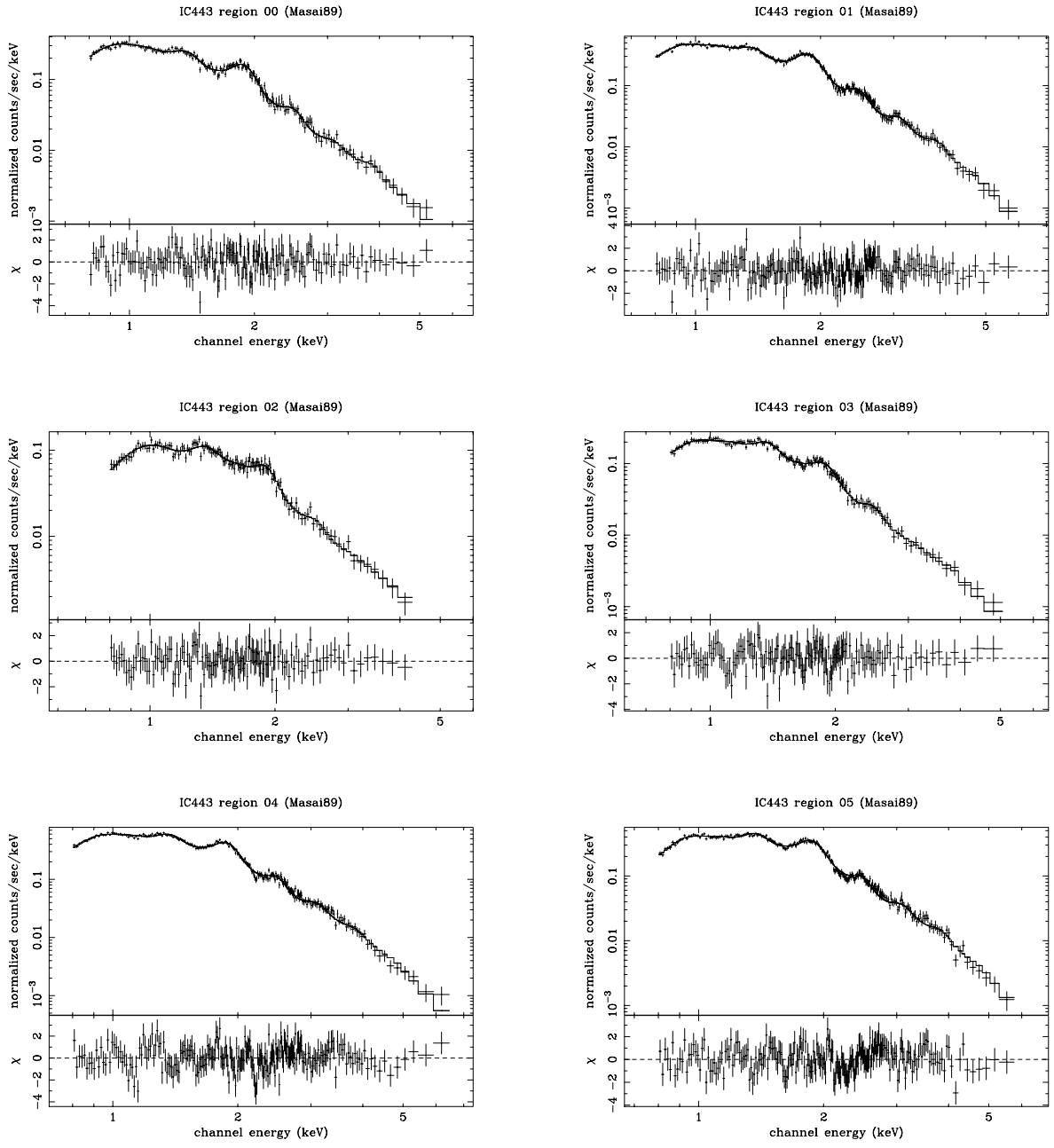

Figure 8.7: The data and the best-fit models of PV-region fittings.

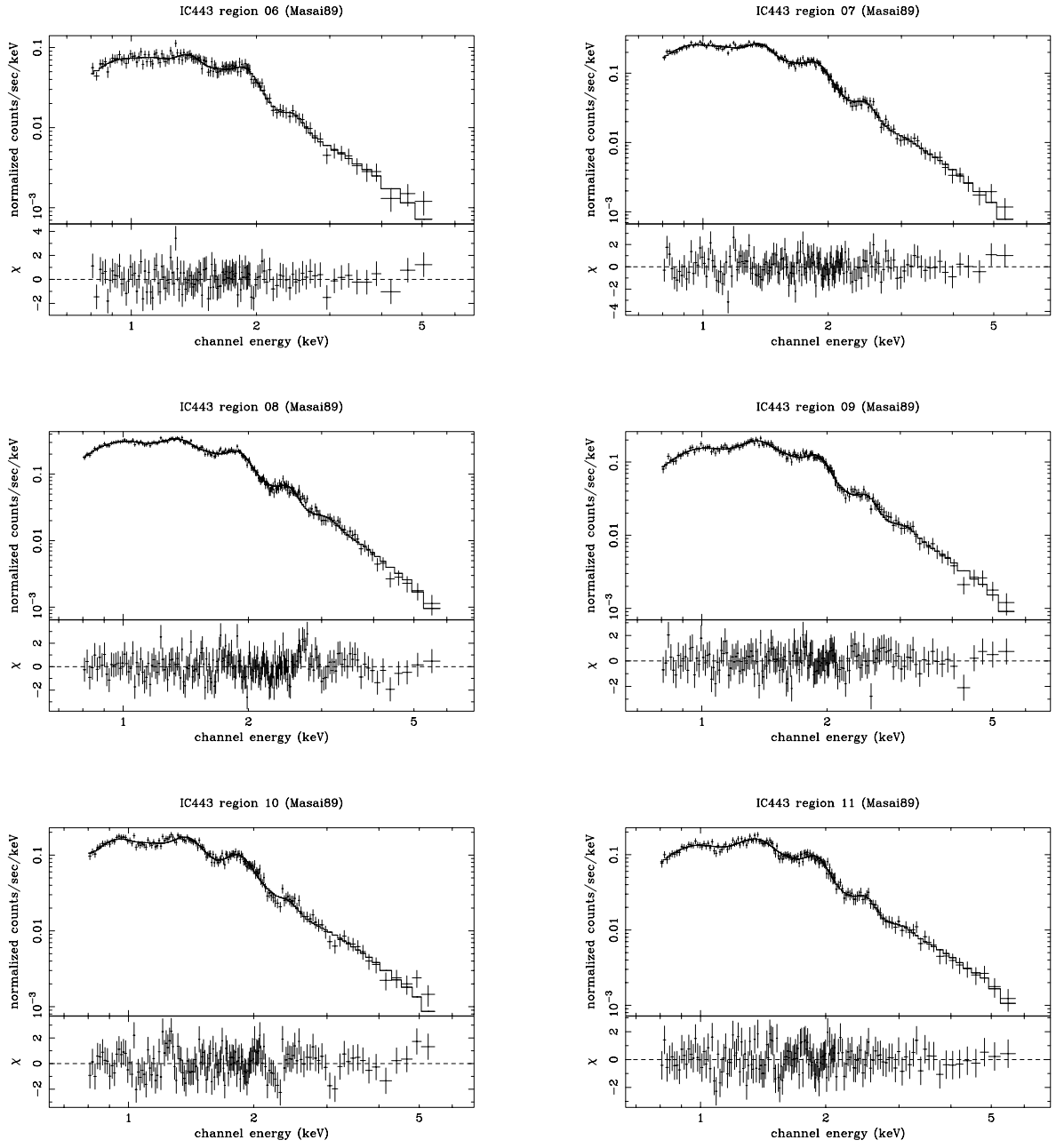

Figure 8.7: (continued) The data and the best-fit models of PV-region fittings.

Table 8.5: The best-fit parameters of the NEI fittings for IC 443 soft components.

Region	$N_{\rm H}$	kT	$\log n_{\rm e}t$	Ne	Na	Mg	Al	Si	S	Ar	Ca	Fe	reduced-χ^2
	$[10^{21}{\rm cm}^{-2}]$	[keV]	[s cm^{-3}]					[solar abundance]					(d.o.f.)
00	4.2	1.22	10.26	0.80	<3.16	0.77	1.25	0.55	0.81	0.68	5.56	0.33	1.076
	$^{+0.4}_{-1.1}$	$^{+0.19}_{-0.14}$	$^{+0.41}_{-0.20}$	$^{+0.21}_{-0.52}$		$^{+0.19}_{-0.17}$	$^{+1.37}_{-0.66}$	$^{+0.14}_{-0.10}$	$^{+0.54}_{-0.36}$	$^{+1.23}_{-0.68}$	$^{+11.30}_{-5.56}$	$^{+0.31}_{-0.16}$	(156)
01	5.5	1.10	10.10	0.82	<2.03	0.63	1.03	0.66	1.53	2.43	12.30	0.38	0.8937
	$^{+0.4}_{-0.6}$	$^{+0.08}_{-0.07}$	$^{+0.10}_{-0.11}$	$^{+0.16}_{-0.13}$		$^{+3.11}_{-0.09}$	$^{+0.47}_{-0.42}$	$^{+0.14}_{-0.10}$	$^{+0.51}_{-0.37}$	$^{+1.20}_{-0.97}$	$^{+10.52}_{-8.47}$	$^{+0.27}_{-0.15}$	(197)
02	4.5	1.29	10.54	0.74	2.06	0.75	2.88	0.41	0.39	<1.11	<11.1	0.22	0.8036
	$^{+2.6}_{-4.0}$	$^{+0.48}_{-0.31}$	$^{+0.27}_{-0.34}$	$^{+0.92}_{-0.63}$	$^{+5.46}_{-2.06}$	$^{+0.50}_{-0.37}$	$^{+2.06}_{-1.59}$	$^{+0.19}_{-0.15}$	$^{+0.32}_{-0.21}$			$^{+0.37}_{-0.22}$	(120)
03	4.9	1.01	10.13	0.77	<4.04	0.84	1.46	0.46	1.05	<1.47	6.50	0.43	0.7949
	$^{+0.7}_{-0.7}$	$^{+0.27}_{-0.13}$	$^{+0.28}_{-0.32}$	$^{+0.26}_{-0.77}$		$^{+0.32}_{-0.21}$	$^{+0.81}_{-0.77}$	$^{+0.44}_{-0.14}$	$^{+1.04}_{-0.52}$		$^{+27.60}_{-6.50}$	$^{+2.90}_{-0.24}$	(135)
04	6.0	1.03	10.22	0.77	<1.07	0.64	1.27	0.52	1.08	1.67	5.21	0.24	1.205
	$^{+0.4}_{-0.4}$	$^{+0.06}_{-0.05}$	$^{+0.11}_{-0.10}$	$^{+0.14}_{-0.12}$		$^{+0.09}_{-0.08}$	$^{+0.39}_{-0.36}$	$^{+0.08}_{-0.06}$	$^{+0.32}_{-0.24}$	$^{+0.80}_{-0.66}$	$^{+6.39}_{-5.21}$	$^{+0.09}_{-0.07}$	(210)
05	7.4	1.07	10.11	1.01	<4.48	0.64	1.15	0.53	1.24	1.87	9.71	0.23	1.104
	$^{+0.6}_{-2.3}$	$^{+0.07}_{-0.06}$	$^{+0.13}_{-0.11}$	$^{+0.23}_{-0.39}$		$^{+0.09}_{-0.18}$	$^{+0.37}_{-0.45}$	$^{+0.11}_{-0.10}$	$^{+0.38}_{-0.34}$	$^{+0.97}_{-0.83}$	$^{+8.75}_{-7.12}$	$^{+0.17}_{-0.23}$	(207)
06	5.4	1.45	10.01	0.68	<7.76	0.82	2.72	0.57	1.14	<1.63	1.52	0.53	0.7757
	$^{+1.2}_{-4.0}$	$^{+0.38}_{-0.32}$	$^{+0.63}_{-0.33}$	$^{+0.46}_{-0.68}$		$^{+0.41}_{-0.36}$	$^{+2.33}_{-1.37}$	$^{+0.51}_{-0.23}$	$^{+0.95}_{-0.68}$		$^{+28.21}_{-1.52}$	$^{+5.48}_{-0.53}$	(111)
07	4.7	1.18	10.07	0.78	<4.91	1.02	2.26	0.56	1.36	<1.26	<9.43	0.46	0.8691
	$^{+0.6}_{-0.6}$	$^{+0.14}_{-0.12}$	$^{+0.30}_{-0.27}$	$^{+0.22}_{-0.78}$		$^{+0.25}_{-0.19}$	$^{+0.92}_{-0.86}$	$^{+0.37}_{-0.15}$	$^{+0.96}_{-0.68}$			$^{+2.06}_{-0.46}$	(149)
08	4.3	1.15	10.69	0.25	<1.11	0.58	1.99	0.42	0.67	0.40	<1.64	0.30	0.9692
	$^{+1.4}_{-1.5}$	$^{+0.09}_{-0.08}$	$^{+0.09}_{-0.15}$	$^{+0.27}_{-0.21}$		$^{+0.16}_{-0.12}$	$^{+0.68}_{-0.57}$	$^{+0.08}_{-0.07}$	$^{+0.13}_{-0.12}$	$^{+0.32}_{-0.29}$		$^{+0.10}_{-0.09}$	(183)
09	3.1	1.41	10.70	0.07	<2.63	0.74	2.71	0.46	0.63	0.31	<2.37	0.34	0.7517
	$^{+2.6}_{-1.6}$	$^{+0.23}_{-0.18}$	$^{+0.08}_{-0.16}$	$^{+0.45}_{-0.07}$		$^{+0.25}_{-0.17}$	$^{+1.19}_{-0.92}$	$^{+0.13}_{-0.10}$	$^{+0.20}_{-0.17}$	$^{+0.40}_{-0.31}$		$^{+0.18}_{-0.18}$	(149)
10	0.9	1.40	9.57	0.30	4.04	0.90	0.86	1.07	1.52	<0.78	<17.1	<20.2	1.069
	$^{+4.0}_{-0.9}$	$^{+0.29}_{-0.19}$	$^{+0.50}_{-0.17}$	$^{+0.67}_{-0.09}$	$^{+1.83}_{-1.48}$	$^{+0.37}_{-0.18}$	$^{+1.37}_{-0.86}$	$^{+0.24}_{-0.60}$	$^{+0.68}_{-0.71}$				(140)
11	2.5	1.93	10.57	<0.35	<1.88	0.96	2.62	0.53	0.63	0.19	<1.95	0.51	0.8144
	$^{+1.6}_{-1.1}$	$^{+0.44}_{-0.29}$	$^{+0.06}_{-0.09}$			$^{+0.31}_{-0.22}$	$^{+1.48}_{-1.10}$	$^{+0.16}_{-0.14}$	$^{+0.24}_{-0.19}$	$^{+0.47}_{-0.19}$		$^{+0.25}_{-0.18}$	(145)
12	3.5	1.09	10.77	0.22	<0.96	0.78	2.31	0.36	0.40	<0.13	<2.13	0.39	0.9384
(AO1)	$^{+1.4}_{-1.5}$	$^{+0.13}_{-0.11}$	$^{+0.09}_{-0.12}$	$^{+0.29}_{-0.22}$		$^{+0.20}_{-0.15}$	$^{+0.86}_{-0.69}$	$^{+0.09}_{-0.07}$	$^{+0.12}_{-0.11}$			$^{+0.14}_{-0.12}$	(132)

The definition of the solar abundances is from Allen (1973).

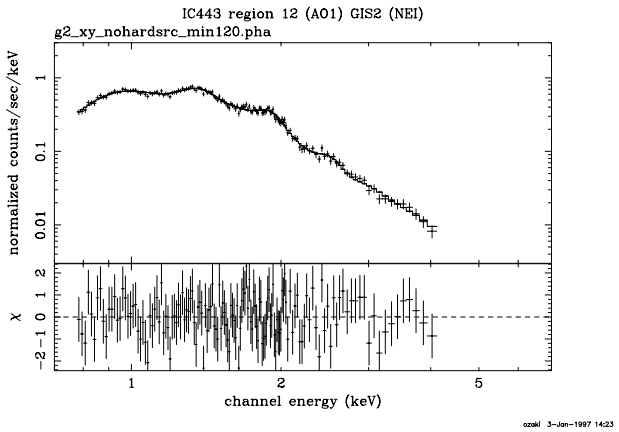

Figure 8.8: The data and the best-fit models of AO1-region fitting.

the systematic change of the absorption which had been seen in Petre et al. (1988) and Asaoka and Aschenback (1994), χ^2 values show that these models are unacceptable in bright regions. Thus, we considered the abundance as a free parameter and performed the fits again for all regions. This time, we got acceptable results; table 8.5 gives the best-fit parameters and figure 8.7 and 8.8 shows the best-fit models with data sets. In contrast to the previous fittings, absorptions show no significant variation.

The flux of the AO1 diffuse component is 5.8×10^{-12} ergs $s^{-1}cm^{-2}$. In particular, a good fit is obtained below 3 keV. In the > 3 keV energy band, however, the model could not represent the data well: undulating residuals remain. No additional hard-tail component can improve the fitting.

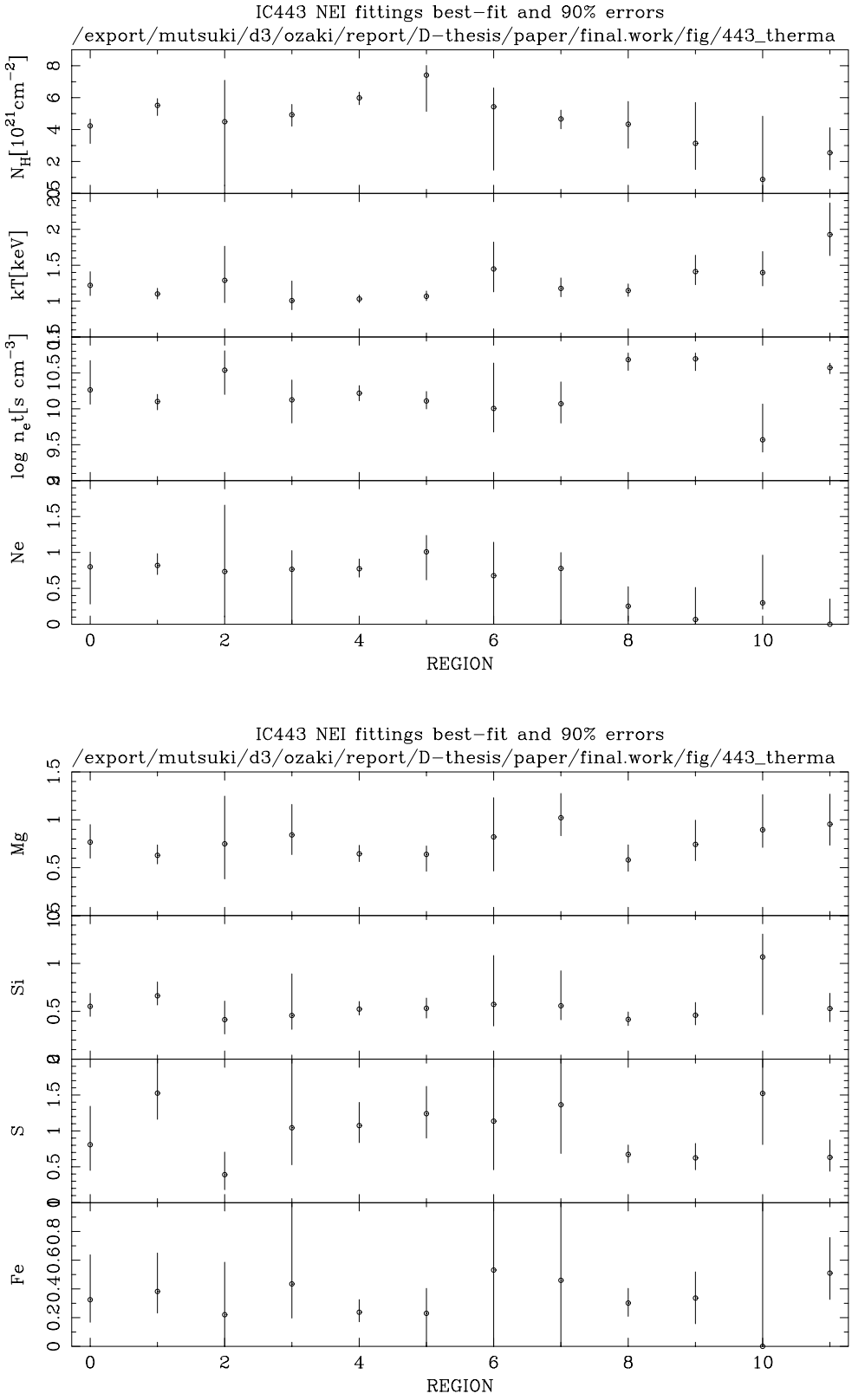

Figure 8.9: The best-fit parameters of the NEI fittings for IC 443 soft components.

Chapter 9

Discussion

9.1 SN 1006

In the present analysis, we succeeded in separating the SN 1006 emission into two qualitatively different parts; one is the weak and uniform soft emission which contains strong fluorescent lines from highly ionized atoms, and the other is the strong power-law emissions without the line confined in two distinct rims which is bright in the radio band as well. The lines in the uniform emission show that the emission is of thermal plasma origin, which is commonly seen in shell-like SNRs. Among the lines, OVII and OVIII have been reported previously, but the others, Ne, Mg, Si and S, are first detected in the present analysis.

The strong power-law reveals a photon index $\simeq 3$, which is steeper than most of the previous observations, up to 20 keV. The difference seems to come from the high temperature plasma of the Lupus region, which is spread more widely than the Lupus Loop so that the major component at the higher energy with large FOV of the previous non-imaging instruments. In the present, on the other hand, the local background contributes little to the SN1006 data because of the small FOV.

In summary, the geometry of SN 1006 can be described as follows: the optically-thin NEI thermal plasma exists in the whole region of the remnant, and, confined strong power-law regions exist in the NE and SW rims of whose shape can be described by a uniform thin disk on the first order approximation (figure 9.1).

9.1.1 Interior emission

Reliability of the background estimation

Since the Interior region is contaminated by various complex backgrounds, we tried to estimate the whole background with two methods; one is to re-construct an *ad hoc* model from the GIS and

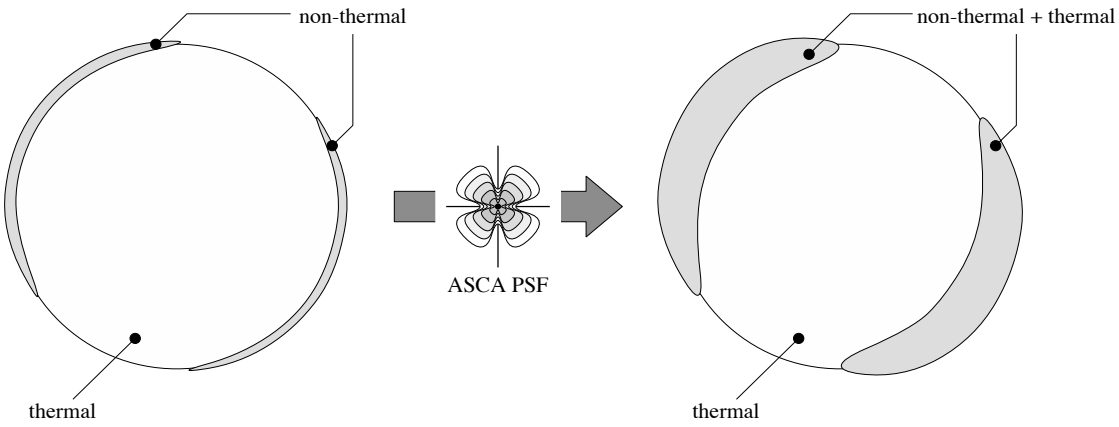

Figure 9.1: Schematic structure of the SN 1006 emission components.

SIS data of SIS-BG region outside the remnant, and the other is to de-compose the background into the known components, standard blank sky, the local diffuse emission and the Rim component leakage coming from the loose XRT PSF, estimate them separately and recompose the background. The former has the advantage that the model is constructed from the real data, while has the disadvantage that the included Rim leakage spectrum may be different from that in the Interior region. The latter has the advantage that each component of the model has the legitimate origin, while it has the disadvantage that the XRT PSF has not been calibrated precisely for such a leakage estimation and there may be components other than those listed above. In fact, we showed that we couldn't use the latter due to the PSF uncertainty. Since the Rim emission leakage is found to be the dominant background in the present analysis, the disadvantages relating to the leakage can affect the strength and the shape of the background model, which immediately affect the source analysis because the estimated backgrounds occupy a considerable ratio of the whole data. The essential solution for the background problem is to carry out further observations with the mirror of a much sharper PSF, which should be available in future missions.

The uncertainty of the background causes some difficulties in the analysis; as the background level above 1.5 keV is close to the continuum level from SN1006, even a little change of the background largely affects the continuum level, and the equivalent widths of lines above 1.5 keV, i.e. Si and S, differ depending significantly on the background model we used.

Plasma condition

In the present analysis, we found that we cannot describe the interior spectra by single-component NEI plasma; neither the center energy of each line nor the width could be described. This implies that at least some of these elements have multi-ionization-temperature structure. The fact that

lines+continuum fittings require not only highly ionized (*i.e.* H- and He-like) Si but also low-ionized (B-like) one supports this. Consequently, we tried two-component NEI as the next step; however, fittings did not converged due to the limitation of the data quality so we had to give up pursuing more complicated model.

The abundances found in single-component fittings are extremely larger than any other SNRs observed so far with ASCA; other SNRs abundances are reported typically as < 0.3 cosmic value (Miyata et al. 1994 for Cygnus loop, Hayashi et al. 1994 for E0102–72), while the present fittings show one – a few tens cosmic abundance for each element. While the fittings could not describe the line profiles precisely, we think that this large abundance is qualitatively correct because the best-fit model should represents the typical component of the plasma.

In contrast to other elements, Fe abundance is much lower than that expected from the type I SNR nucleosynthesis theory. If Fe is synthesized at the core of the exploding white dwarf, it may be considered that Fe stays at the central part of the remnant and are yet not swept-up by the reverse shock. The *ad-hoc* model fitting for IN2 region suggests a large Fe abundance, but we should not trust it easily: Fe-L fitting for ASCA data has strong connection with O and Ne ionization condition, which we ignored in the *ad-hoc* fittings.

We cannot determine the emission measure of the whole thermal component precisely with ASCA because the thermal component is strongly contaminated with the hard component and a certain part of the thermal region is covered with the non-thermal rim. Instead, we discuss it using the limited information of IN1 and IN2 regions.

Since each emission measure shows similar values with each other and we have not enough information to discuss the spectral variation of the remnant, we consider here that shocked electrons inside the remnant have uniform temperature and density distribution. Hereafter, we mainly use the IN1 emission-measure $8.2 \times 10^{52} \times \left(\frac{D}{1\ \mathrm{kpc}}\right)^2\ \mathrm{cm}^{-3}\mathrm{arcmin}^{-2}$ as the typical value because it does not include the limb-brightening effect. Assuming that the shocked plasma forms a uniform shell of 15 arcmin radius, we obtain the whole emission measure as $1.2 \times 10^{56} \times \left(\frac{D}{1\ \mathrm{kpc}}\right)^2\ \mathrm{cm}^{-3}$, and the shocked mass becomes

$$M_{\mathrm{sh}} \simeq 0.13 n_{\mathrm{e}}^{-1} \left(\frac{D}{1\ \mathrm{kpc}}\right)^2 M_{\odot}. \tag{9.1}$$

If we assume D as 1.7 kpc or 3.1 kpc (Long, Blair and van den Bergh 1988), M_{sh} becomes $0.4 n_{\mathrm{e}}^{-1}$ or $1.2 n_{\mathrm{e}}^{-1} M_{\odot}$, respectively.

On the other hand, we can estimate the total mass inside the remnant as

$$M_{\mathrm{all}} \simeq 0.3 n_{\mathrm{e}} \left(\frac{D}{1\ \mathrm{kpc}}\right)^3 M_{\odot} \tag{9.2}$$

where n_{e} is the the density of *shocked* electrons, assuming the strong shock condition. If we assume

D as 1.7 kpc or 3.1 kpc, $M_{\rm all}$ becomes $1.5 n_{\rm e}^{-1}$ or $8.9 n_{\rm e}^{-1} M_{\odot}$, respectively.

If the remnant is in the adiabatic phase, almost all matter inside the shell are shocked so $M_{\rm sh} \simeq M_{\rm all}$. In contrast, if the remnant is still in the free-expansion phase, there is much unshocked matter inside the remnant, so $M_{\rm sh} < M_{\rm all}$. Using $M_{\rm sh}$ and $M_{\rm all}$ obtained for reasonable D as above, we obtain $n_{\rm e} \simeq 0.5$ cm^{-3} as the upper-limit for the adiabatic-phase condition. Since the remnant is at such a high galactic-latitude that $n_{\rm e}$ could satisfy this low-density condition, we could not exclude the adiabatic phase. The free-expansion cannot be exclude either, because $n_{\rm e} > 0.5$ cm^{-3} can still satisfy the constraint of the white-dwarf mass limit $M_{\rm all} < 1.2 M_{\odot}$.

Therefore, it is possible that large amounts of unshocked matter remain inside the remnant. It is consistent with the fact of weak detection of iron line together with the existence of the strong low-ionized Fe absorption in the UV band, which suggests that the remnant contains much unshocked iron inside (Wu et al. 1993).

The discussion above suggests that X-rays come primarily from the ejecta which consists of the synthesized heavy elements in the supernova explosion. Accordingly, we infer that SN1006 is still in the free-expansion or in the early adiabatic phase.

9.1.2 Power-law emission

Emission mechanism

Thermal and non-thermal have been suggested as the dominant emission mechanism of SN 1006. With the present Ginga observation, we were able to clearly reject the possibility of the simple thermal spectrum and showed that the emission can be described by a power-law up to 20 keV. With the present ASCA observation, which has enough capability to distinguish emission lines from the continuum with high accuracy, we made clear that the lines, including the previously reported oxygen lines, in the strong rims can all be explained by the uniformly-distributed thermal component.

If the emission comes from the complex of thermal plasmas of various temperatures, each component should have a temperature of a few keV to construct a steep power-law (see the emitting spectral form, equation (2.37), of which shoulder energy is near the plasma temperature), thus there should be much stronger lines because the stronger thermal-bremsstrahlung continuum means higher density or higher temperature which makes the plasma produce more effective line emission.

Thus we strongly suggest that the power-law component is non-thermal in origin. The photon indices of Ginga and ASCA observations do not agree with each other; Ginga showed a steeper slope than ASCA. This can be attributed to the difference in the energy range; Ginga band is 2–20 keV,

while ASCA is 0.5–10 keV. This difference and the fact that the ASCA power-law component needs significantly larger absorption than the Interior region suggest that the slope becomes gradually steeper in higher energy.

In the X-ray band, there are three candidates for the non-thermal emission mechanism; bremsstrahlung, inverse-Compton scattering and synchrotron radiation. In each mechanism, the emitting electrons have power-law energy distribution formed by the shock acceleration. We will discuss the possibility of each mechanism below.

Bremsstrahlung The bremsstrahlung spectrum from the nonrelativistic and monochromatic energy of electron becomes

$$F(E) \propto \ln\left(\frac{\sqrt{\varepsilon}-\sqrt{\varepsilon-E}}{E}\right) \tag{9.3}$$

for $E < \varepsilon$, where ε is the electron energy (Asvarov et al. 1990). In case of the relativistic electron, the spectrum becomes $F(E) \propto \ln(E^{-1})$ for the low energy limit, $E \ll \varepsilon$ (Rybicki and Lightman 1979). This function is almost flat (i.e. spectral index $\simeq 0$) below $\sim 0.1\varepsilon$ and becomes 0 at ε. Therefore, X-rays come mainly from electrons with energy similar to the emitted photons. Accordingly, if the electrons have a steep power-law distribution in the 100 eV–100 keV range, the X-ray emission also shows a steep power-law, as in the case for SN 1006. In such a case, the ionization should progress like a thin-thermal plasma of a few keV; thus, strong emission lines should be present as the Interior thermal region. However, such a line is not present. Thus, we can reject the bremsstrahlung model.

Inverse Compton The frequency and the relative strength of the synchrotron emission to the inverse Compton depend only on the magnetic field strength. The slope of the synchrotron emission from power-law electrons is equal to that of the inverse Compton scattering. Based on these facts, we can examine the inverse Compton assumption by comparing the synchrotron radio spectrum and the calculated spectrum of the synchrotron emission from the X-ray electrons; the calculated one should explain the radio spectrum, or at least be connected smoothly to the radio observation.

Since the Rim emission from the SN 1006 is the only radio power-law for which photon densities are much smaller than the 3 K microwave background, the dominant source for the inverse-Compton scattering is the 3 K microwave background. Since the mean output photon energy by the inverse-Compton process is $\sim \gamma^2 E_{\rm i}$, where γ and $E_{\rm i}$ are the electron's Lorentz factor and the initial energy of the photon, the Lorentz factor of electrons which can kick up the 3 K photon to a few keV (10^7–10^8 K) X-ray is $\gamma \sim 10^{3.5}$.

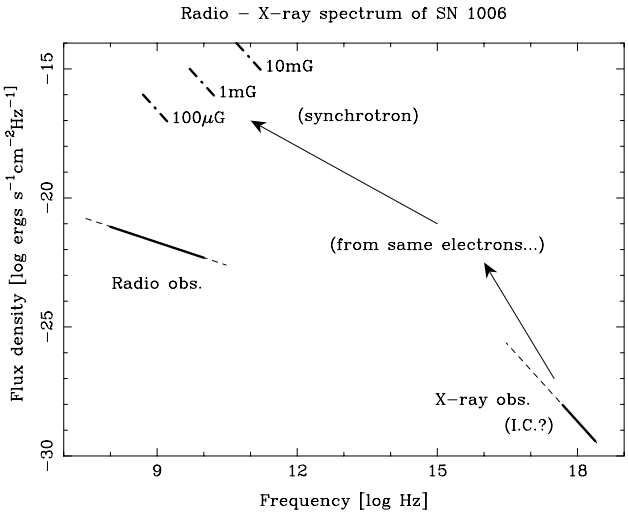

Figure 9.2: If the rim X-rays were inverse Compton origin, the predicted corresponding synchrotron emission is inconsistent with radio observations or requires unnatural spectral jump.

Since the slope of the synchrotron emission spectrum is equal to the inverse Compton scattering spectrum, the synchrotron emission from X-ray electrons can not be in the radio band that has already been observed; therefore, the emission should in the sub-millimeter, < 800 MHz or IR band. At the same time, we can calculate the strength of the synchrotron emission when the inverse Compton component and the magnetic field strength are given. Figure 9.2 is a schematic diagram of the relation between the observed and calculated spectra. While these calculations are only for order-estimation, we can easily see that the stronger magnetic field pushes the emission away from the observed band, and the emission becomes much stronger than the natural extension of the radio observation. Thus, the inverse Compton mechanism is very unlikely.

Synchrotron emission If the emission is synchrotron origin, the X-ray spectrum should be smoothly connected to the radio spectrum of the same origin. Figure 9.3 shows the whole SN 1006 spectrum from radio to X-ray frequencies; the two spectra cross at the frequency of $\simeq 8 \times 10^{17}$ Hz, or $\simeq 250$ eV. In fact, as we already pointed out, the ASCA and Ginga spectra suggest that the power-law index becomes smaller (flatter) in the lower energy than in higher energies. ROSAT results (Willingale et al. 1996) also support it. These support the assumption that the radio and X-ray spectra have the same origin, synchrotron emission.

If X-rays are of the synchrotron emission origin, we can calculate the loss time using the break frequency. Using the fact that the crossing energy of X-ray and radio spectra is $\simeq 250$ eV, the lifetime of the synchrotron electrons τ becomes larger than 1000 yr for $B < 20\mu$G, which

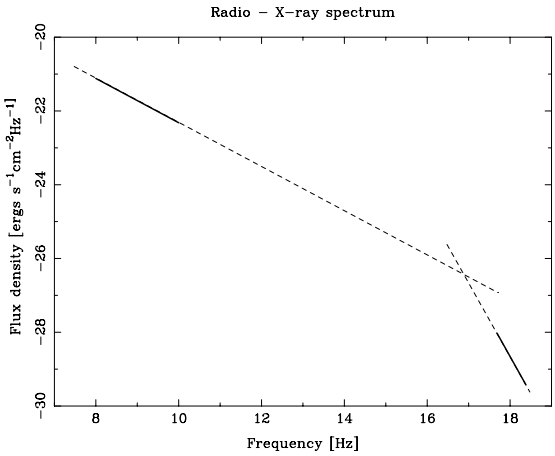

Figure 9.3: The spectra of SN 1006 from radio to X-ray frequencies. The radio data are cited from Reynolds and Ellison (1992).

can set the upper-limit of the magnetic field strength.

Energetics

If the emission is synchrotron origin, we can estimate the electron energy which produce the synchrotron photon from equation (2.49) if the magnetic field strength is given. While there is no measurement of the strength for any type Ia SNR, the best estimate is thought to be 6–10μG (Reynolds and Ellison 1991). Since the power-law continuum extends up to $\simeq$ 20 keV, the electron energy becomes $\geq$ 200 TeV.

The total energy of the synchrotron-emitting electrons becomes 3×10^{47} erg, which is about 0.1% of the kinetic energy released by the explosion. This value changes little when X-ray observation parameters vary, because the spectral slope is so steep that most of the energies are held by low-energy electrons that emit mainly in radio band.

Acceleration source

As the traditional source of synchrotron electrons in the X-ray band, pulsars (rotating neutron stars) have been discussed. If the energetic electrons are supplied from a pulsar, it should be near the center of the remnant because the two power-law regions are located symmetrically at opposite sides of the remnant. While pulsars usually have center-filled morphology which is thought to comes from the positronic pulsar wind, no corresponding point-like source has been discovered in SN 1006 from the radio to gamma-ray band. This suggests that the power-law electrons are non-pulsar in origin.

Even if the neutron star is invisible for some reason, some problems remain; the power-law shells are much thinner than that of W 50, in which the central source SS 433 is thought to supply the accelerated electrons (Yamauchi, Kawai and Aoki 1994). In addition, there seems to be no significant emission originating from the electron flows inside the remnant. To create such geometry, the matter density and the magnetic field strength both on the inside and the outside of the remnant should be much lower than the shell. It is unnatural to assume that only the shell has far stronger magnetic field than elsewhere. Thus as far as the energetic electrons in SN1006 are concerned, the pulsar origin is unlikely.

A more likely mechanism, considering the fact that the X-ray shells well coincide with the radio, is the first-order Fermi acceleration in the shock. If this is correct, it is the first observational evidence that this mechanism can accelerate particles to such a high energy ($\geq$ 200 TeV). In this case, not only electrons but also the protons should be accelerated up to the same energy because ultrarelativistic electron and proton, except for their charges, are essentially identical in the acceleration mechanism. Therefore, the power-law component can be interpreted to support the cosmic-ray (proton) acceleration in SNR up to $\geq$ 200 TeV.

The efficiency of the first-order Fermi acceleration should change from position to position depending on the reflecting angle between the shock-propagating direction and the magnetic field. It is generally thought that a larger angle makes the efficiency larger because the mean free path of charged particle whose flight direction is perpendicular to the magnetic field is expected to be much shorter than for that parallel to the field. Therefore, the strong emission is expected to be distributed near the great circle of the shock shell if the remnant is in a nearly uniform magnetic field. However, the emission is confined to two polar regions, where the radio polarization implies that the magnetic fields cross the shock front with small incident angle (Reynolds and Gilmore, 1993). There are two possible explanations: one is that the acceleration efficiency is higher in the parallel shock than the perpendicular one, contrary to the generally believed theory. The other is that the magnetic field strength is not uniform due to the magnetic field structure of the progenitor. In the latter, the emission must be determined by the balance between the acceleration efficiency and the synchrotron energy loss. More study should be done for deep understanding.

Possibility of the Gamma-ray observation

If the emission is of synchrotron, the X-ray emitting electrons should kick up the 3 K background to a few TeV by the inverse-Compton process. If such a emission is detected by EGRET aboard the Compton Gamma-Ray Observatory (30 MeV–10 GeV) or CANGAROO air Čerenkov experiment ($\simeq$ 100 GeV), we can determine the magnetic field strength at the rims by comparing it to the X-ray

synchrotron flux. The X-ray flux is determined by the number of the electrons and the magnetic field strength, because the inverse-Compton photon flux is determined only by the number of the scattering electrons and the source photon density.

9.2 IC 443

In the present analysis, we first obtained the large-scale structure of IC 443 with high energy and moderate spatial resolutions up to 10 keV. With these features, we discovered an incomplete semi-circular structure in the high-energy band which is seen in other wavelengths, and analyzed the previously-known thermal components under the condition that the continuum shape and the line profiles, from which we can determine the absorption column density and the abundances, respectively, can be distinguished from each other.

9.2.1 Soft component

We analyzed the large-scale spectral trend over the bright part of IC 443. This is the first time that such a analysis is done with enough high energy resolution and good statistics to distinguish each abundance up to $\simeq 5$ keV.

In previous observations, X-ray spectra displayed systematic variation in the absorption column density for each position, and the correlation between the X-ray spectra and the CO line-emission structure has been suggested. In the present analysis, this variation was seen with single-component NEI models whose abundance of each element has been linked to one another, but the fitting itself should be rejected at least for data with good statistics. In contrast, the variation disappeared when we made all the major abundances free, and we obtained statistically acceptable results. This implies that the variation of the absorption column seen in previous observations should be interpreted as the variation of abundances. This variation could, however, not be seen directly in the present analysis due to the limitation of the GIS spectral resolution and insufficient statistics of data sets.

Most of the parameters, however, do not differ largely from position to position. In particular, the absorptions do not show the systematic change which was suggested with Einstein IPC (Petre et al. 1988) and ROSAT PSPC (Asaoka and Aschenbach 1994); though the previous observation suggested that the southern parts of the PV FOV (region 05–09) have higher absorption than the northern parts, the present analysis did not show such tendency.

The ionization time $n_{\rm e}t$, however, seems to change systematically; in the region 08, 09 and 11, they are significantly higher than for other regions. For the region 09 and 11, this can be attributed

to the molecular clouds seen in IRAS 60μm band and H_2 1-0 S(1) line. Since the molecular clouds and the surrounding regions have higher density, ionization near the clouds should proceeds faster than the other regions. The region 08, however, has no active counterpart, suggesting no interaction between the molecular cloud and the shock in radio or IR band. In this region, the density would not be high enough to form the molecular cloud.

Abundances of most of the elements do not largely differ largely from solar values, except for silicon and iron that have significantly smaller values than the solar values. This suggests that the X-ray emitting materials are mainly interstellar gas which is heated by the shock in the adiabatic phase.

9.2.2 Hard component

With the present analysis, we found that the hard component has an incomplete semi-circular form, which lie along the previously known molecular clouds. Within the region, there are two especially bright spots which are near to but do not totally coincide with the known CO molecular could clumps.

The photon indices of the hard components found with ASCA agree with that of the Ginga result within the 90% error. However, the 7 keV flux of the total ASCA hard component of $\simeq 9.6 \times 10^{-5}$ photons $s^{-1}keV^{-1}cm^{-2}$ can account for only 30% of the Ginga flux at 7 keV of $\simeq 2 \times 10^{-4}$ photons $s^{-1}keV^{-1}cm^{-2}$ (figure 2 of Wang et al. 1992). This suggests that a further extended emission outside the present ASCA FOV may be present. The hard-bar at the southern edge of the PV FOV may possibly be extending to the south, where radio emission is certainly extending.

While SNR spectra are usually described by one or a few component NEI plasma, we fitted the hard region by the Raymond-Smith model, which describes collisional equilibrium ionization plasma, in the present analysis to examine Fe-K line strength. It is because most of the emission lines of the SNR, including Fe, are strong enough for Raymond-Smith model to discuss the presence of line emissions. We wanted to examine whether the hard components have significant line emission. Since the R-S model could set only the upper-limit for the Fe abundance, we think that the emission is probably non-thermal in origin.

Nevertheless, we will first discuss the thermal origin briefly. If the emission is thermal, the high temperature plasma would be due to molecular clouds, because the hard components coincide with them. Since the molecular clouds would have higher density $n_{H_2} \geq 10^5$ cm^{-3} (Dickman et al. 1992) than the usual interstellar density $n_H \sim 1$ cm^{-3}, the energy transfer from atoms to electrons in the clouds should progress more rapidly than for outside the clouds. Since the transfer speed scales as

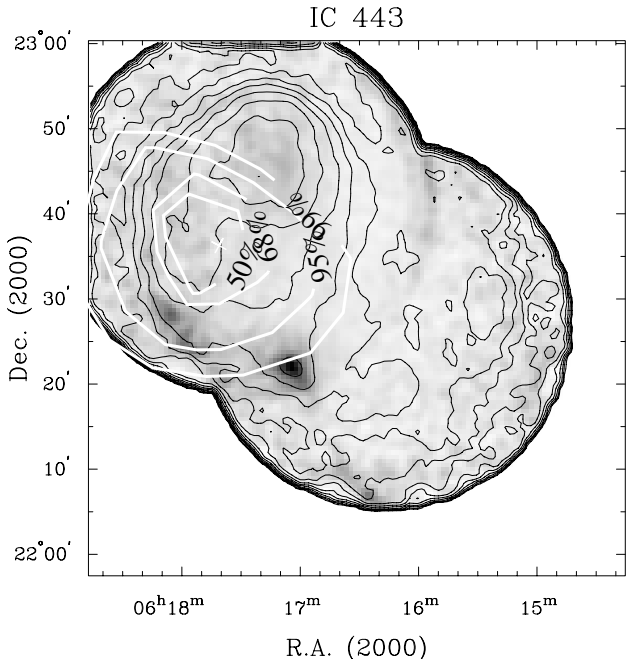

Figure 9.4: The ASCA soft and hard components (the black contour and the grayscale, respectively) and the EGRET point-source confidence contour (white).

$n_e^{2/5}$ (equation (2.32)), it is possible that the electron temperature near the molecular cloud is a few times larger than outside, which is exactly what we found.

As for the non-thermal emission, same candidates as discussed for SN 1006 are conceivable. Among them, the inverse Compton process and bremsstrahlung should be rejected for the same reason as in the case of the SN 1006. As another support for the synchrotron origin, we can discuss the relation between the hard component and the GeV gamma-ray emission found with EGRET on Compton Gamma-Ray Observatory (Thompson et al. 1995, Esposito et al. 1996). The semi-circular shape overlaps the EGRET point-source error contour, with 95% confidence level at about 20 arcmin diameter (figure 9.4) and covers the hard-bar. In the center of the circular shape, we found no significant hard spot. However, it is possible that the gamma rays come from the diffuse source because the PSF of EGRET is larger than the spatial extent of IC 443, and the position and the contour were determined under the assumption that the gamma rays come from a point source (Esposito et al. 1996).

The photon indices of the hard-spot and the hard-bar agree with each other within 90% error, and also agree with the EGRET point source. It implies that the two different-band spectra are closely related. As the emission mechanism, we can consider that the X-rays are emitted by the synchrotron radiation, and the gamma ray by the inverse-Compton mechanism from the same electrons. In this case, we can estimate the magnetic field strength of the synchrotron region using

the relative strength of the two regions.

Since IC 443 has strong infrared (IR) emission, the inverse-Compton photon flux should be larger than in the case where the source photon is only 3 K microwave background. Since we do not know the IR photon density at the inverse-Compton region, we can only estimate the lower-limit of the magnetic field at the scattering region as follows.

For a power-law distribution of relativistic electrons of which the number density with energies between γ and $\gamma + d\gamma$ is expressed in the form

$$N(\gamma)d\gamma = C\gamma^{-p}\,d\gamma, \tag{9.4}$$

where C is the constant, the inverse-Compton spectrum from the black-body radiation becomes

$$I(E) = \frac{C8\pi^2 r_e^2}{h^3c^2}(kT)^{\frac{p+5}{2}}F(p)E^{-\frac{p+1}{2}}\ [\text{photon s}^{-1}\text{erg}^{-1}] \tag{9.5}$$

$$F(p) = A(p)\Gamma\left(\frac{p+5}{2}\right)\zeta\left(\frac{p+5}{2}\right)$$

$$A(p) = 2^{p+3}\frac{p^2+4p+11}{(p+3)^2(p+5)(p+1)},$$

where r_e is the classical electron radius (Rybicki and Lightman 1979).

Substituting the EGRET observational value (Esposito et al. 1996), we can set the upper-limit to the number of the inverse-Compton electrons C as

$$\frac{C}{D^2} \leq 1.1 \times 10^{17}\ [\text{cm}^{-2}], \tag{9.6}$$

where D is the distance toward the IC 443. With this condition, we can set the lower-limit of the synchrotron magnetic field strength B as

$$B \geq 1.0\ [\mu\text{G}] \tag{9.7}$$

using equation (2.52). Since the hard X-ray region is thought to be inside or near the molecular cloud, the magnetic field is expected to be larger than the interstellar average $B \simeq 3\mu$G. Therefore, it is reasonable to assume that the X-rays and gamma rays are emitted from the same electrons with the synchrotron emission and the inverse-Compton mechanism, respectively.

If the X- and gamma rays are emitted with the processes above, the upper-limit of the field strength can also be calculated as follows. The extrapolation of the EGRET emission at X-ray band is clearly stronger than the observed value; accordingly, the spectrum should become flatter at some break point between X- and gamma-ray bands. This point should correspond to the break of the synchrotron component between radio and X-ray bands. To make the flatter inverse-Compton component weaker than the X-ray observation, the point has to be higher than a certain energy;

therefore, the magnetic field should be weaker than a certain value. Since there is no published data to set the radio flux of the X-ray emitting region with which we can determine the synchrotron-break frequency, we have to assume the flux. Assuming that 1/10 of the whole-remnant emission is of the X-ray region origin, we obtain the upper-limit of the field strength as $B \simeq 20\mu$G. This shifts higher if the radio-flux decreases.

Chapter 10

Conclusions

In the present work, we observed two shell-like supernova remnants, SN 1006 and IC 443, with Ginga and ASCA, and found that each has two qualitatively different emissions, the diffuse soft NEI plasma emission and the edge-confined hard component.

We made clear that the hard component of SN 1006, which has been known as the dominant X-rays and has been discussed as the origin, is not a thermal emission, but non-thermal. The spatial distribution of the hard component is completely different from that of the soft, but similar to the radio. The X-ray spectrum can also be smoothly connected to the radio slope. Therefore, both the hard X-ray and radio emissions originate from the same process, most probably from synchrotron radiation of high-energy electrons accelerated at the shock front. The highest energy of the source electrons is suggested to be as large as $\sim$ 100 TeV. We infer that protons are also accelerated up to the same energy, and suggest that the shell-like SNRs are, even if not all, major cosmic X-ray sources.

The X-ray spectrum of the hard components in IC 443 can be described either by a power-law or thermal bremsstrahlung. From radio results together with the GeV gamma with GRO, we propose that the likely scenario is that in which the X-rays are synchrotron emission from high energy electrons up to $\sim$ 100 TeV, although a thermal plasma emission of higher electron temperature than the soft component due to higher density is also possible. To judge the origin, we need further observations. Since the present hard component is weaker than that detected by Ginga, the component should have a more extensive distribution than the ASCA FOV.

The soft component of SN 1006 showed large abundance of heavy elements. This suggests that SN 1006 is still in the free expansion or early adiabatic phase, in which X-rays comes mainly from the heavy-element rich ejecta. Further precise study with improved spatial resolution should be done to separate the thermal emission from the strong non-thermal emission.

For IC 443 soft component, we first carried out the systematic analysis with better energy resolution than before. We found no significant variation of the absorption column across the whole remnant, contrary to previous observations. The abundances are roughly solar with no variation over the whole SNR region, hence the soft X-rays from most region of the remnant are likely to be from the interstellar gas rather than the ejecta. We therefore infer that IC443 is in a typical phase of adiabatic expansion.

The detection of the hard (and probably synchrotron) emission from both free-expansion and adiabatic phase SNRs suggests that the cosmic rays up to ~ 100 TeV are accelerated in various stages of SNRs. To confirm this possibility, further studies on hard X-rays from other shell-like SNRs of various ages are required.

Acknowledgments

I would like to thank Prof. K. Koyama for his continuous guidance and encouragement throughout the 5 years of my graduate course. Also, I thank Drs. S. Yamauchi, T. Tsuru and H. Awaki for their guidance and encouragement. I thank Dr. S. Ueno, Mr. I. Hayashi, Y. Maeda, H. Matsumoto, H. Tomida, M. Sakano, K. Hamaguchi, Ms. Y. Tsuboi and M. Nishiuchi for their encouragement, technical advise and discussions. I thank Ms. Rieko Tsurudome for proofreading the manuscript.

Dr. K. Iwasawa kindly supplied us with the BG 2 data of the Ginga observation.

All observational data were obtained by the members of the Ginga team and the ASCA team.

The Ginga data analysis was performed with the FACOM M340 computer of The High Energy Physics Laboratory of Kyoto University.

This research made use of the HEASARC database, SkyView service (NASA/Goddard), the NASA Astrophysics Data System abstract service and the NASA/IPAC extragalactic database (NED).

This study was supported by the grants for JSPS Research Fellowships for Young Scientists.

References

Allen, C. W. 1973, Astrophysical Quantities, 3rd. ed. (The Athlone Press, London)

Asaoka, I. and Aschenbach, B., 1994, AA, 284, 573

Asvarov, A. I., Dogiel, V. A., Guseinov, O. H. and Kasumov, F. K., 1990, AA, 229, 196

Awaki, H., Koyama, K., Kunieda, H., Takano, S., Tawara, Y. and Ohashi, T., 1991, ApJ, 366, 88

Baade, W., 1943, ApJ, 97, 119

Becker, R. H., Szymkowiak, A. E., Boldt, E. A., Holt, S. S., and Serlemitsos, P. J., 1980, ApJL, 240, L33

Bell, A. R., 1978, MNRAS, 182, 147

Bolton, J. G., Gardner, F. F. and Mackey, M. B., 1964, AJP, 17, 340

Braun, R. and Strom, R. G., 1986, AA, 164, 193

Cadonau, R., Sandage, A., Tammann, G. A., 1985, in Supernovae as Distance Indicators, ed. N. Bartel (Berlin: Springer), p.151.

Chevalier, R. A., 1982, ApJ, 258, 790

Chevalier, R. A., Kirshner, R. P. and Raymond, J. C., 1980, ApJ, 235, 186

Clark, D. H. and Caswell, J. L., 1976, MNRAS, 174, 267

Cornett, R. H., Chin, G. and Knapp, G. R., 1977, AA, 54, 889

Cox, D., 1972, ApJ, 178, 159

Davelaar, J., Bleeker, J. A. M., Deerenberg, A. J. M., Tanaka, Y., Hayakawa, S., and Yamashita, K., 1979, ApJ, 230, 428

DeNoyer, L. K., 1978, MNRAS, 183, 187

DeNoyer, L. K., 1979a, ApJL, 228, L41

DeNoyer, L. K., 1979b, ApJL, 232, L165

Dickman, R. L., Snell, R. L., Ziurys, L. M. and Huang, Y. -L., 1992, ApJ, 400, 203

Dwek, E., Petre, R., Szymkowiak, A. and Rice, W., 1987, ApJ, 320, L27

Erickson, W. C. and Mahoney, M. J., 1985, ApJ, 290, 596

Esposito, J. A., Hunter, S. D., Kanbach, G. and Sreekumar, P., 1996, ApJ, 461, 820

Gardner, F. F. and Milne, D. K., 1965, AJ, 70, 754

Goldstein, B. R. and Yoke, H. P., 1965, AJ, 70, 748

Goldstein, B. R., 1965, AJ, 70, 105

Gorenstein, P., Harnden Jr, F. R. and Tucker, W. H., 1974, ApJ, 192, 661

Green, D. A., 1996, http://www.mrao.cam.ac.uk/surveys/snrs/

Hamilton, A. J. S., Sarazin, C. L. and Szymkowiak, A. E., 1986, ApJ, 300, 698

Hamilton, A. J. S., Sarazin, C. L., 1984, ApJ, 281, 682

Hayashi, I., Koyama, K., Ozaki, M., Miyata, E., Tsunemi, H., Hughes, J.P. and, Petre, R., 1994, PASJ, 46, L121

Hughes, J. P., 1991, in supernovae, ed S. E. Woosley (Springer-Verlag, new york) p661

Hughes, J. P., and Helfand, 1985, ApJ, 291, 544

Janesick, J., Elliott, T., and Garmire, G., 1985, Proc. X-ray Instrumentation in Astronomy, SPIE 597, 364

Kennel, C. F., and Coroniti, F. V., 1984, ApJ, 283, 694

Kirshner, R. P., Winkler, P. F. and Chevalier, R. A., 1987, ApJ, 315, L135

Koyama, K., 1989, PASJ, 41, 665

Koyama, K., Tsunemi, H., Becker, R. h. and Hughes, J. P., 1987, PASJ, 39, 437

Landau, L. D. and Lifshitz, E. M., 1959, Fluid Mechanics, London Pergamon

Lasker, B. M. 1981, ApJ, 244, 517

Leahy, D. A., Nousek, J. and hamilton, A. J. S., 1991, ApJ, 374, 218

Long, K. S., Blair, W. P. and van den Bergh, S., 1988, ApJ, 333, 749

Masai, K., 1984, Ap&SS, 98, 367

Masai, K., 1994, ApJ, 437, 770

McKee, C. F., 1974, ApJ, 188, 335

Mills, B. Y., Slee, O. B. and Hill, E. R., 1960, AJP, 13, 676

Milne, D. K., 1970, AJP, 93, 425

Milne, D. K., 1971, AJP, 24, 757

Minkowski, R., 1963, Annual Review of Astronomy and Astrophysics, 2, 247

Minkowski, R., 1966, AJ, 71, 371

Miyata, E., Tsunemi, H., Pisarski, R. and, Kissel, S. E., 1994, PASJ, 46, L101

Moffett, D. A., Goss, W. M., and Reynolds, S. P., 1993, AJ, 106, 1566

Mufson, S. L., McCullough, M. L., Dickel, J. R., Petre, R., White, R. and Chevalier, R., 1986, AJ, 92, 1349

Murakami, T., Fujii, M., Hayashida, K., Itoh, M., Nishimura, J., Yamagami, T., Yoshida, A.,

Conner, J. P., Evans, W. D., Fenimore, E. E., Klevesadel, R. W., Spencer, K. M., Murakami, H., Kawai, N., Kondo, I. and katoh, M., 1989, PASJ, 41,405

Ohashi, T., Ebisawa, K., Fukazawa, Y., Hiyoshi, K., Horii, M., Ikebe, Y., Ikeda, H., Inoue, H., Ishida, M., Ishisaki, Y, Ishizuka, T., Kamijo, S., Kaneda, H., Kohmura, Y., Makishima, K., Mihara, T., Tashiro, M., Murakami, T., Shoumura, R., Tanaka, Y., Ueda, Y., Taguchi, K., Tsuru, T. and, Takeshima, T., 1996, PASJ, 48, 157

Palmieri, T. M., Burginyon, G. A., Hill, R. W., Scudder, J. K., and Seward, F. D., 1972, ApJ, 177, 387

Petre, R., Szymkowiak, A. E., Seward, F. D. and Willingale, R., 1988, ApJ, 335, 215

Pye, J. P., Pounds, K. A., Rolf, D. P., Seward, F. D., Smith, A. and Willingale, R., 1981, MNRAS, 194, 569

Raymond, J. C., Blair, W. P. and Long, K. S., 1995, ApJ, 454, L31

Reynolds, S. P. and Chevalier, R. A., 1981, ApJ, 245, 912

Reynolds, S. P. and Ellison, D. C., 1992, ApJ, 399, L75

Reynolds, S. P. and Ellison, D. C., Proc. 22nd International Cosmic Ray Conference (Dublin Institute for Advanced Studies, Dublin, 1991), vol.2, pp.404–407

Reynolds, S. P. and Gilmore, D. M., 1986, AJ, 92, 1138

Reynolds, S. P. and Gilmore, D. M., 1993, AJ, 106, 272

Roger, R. S., Milne, D. K., Kesteven, M. J., Wellington, K. J. and Haynes, R. F., 1988, ApJ, 332, 940

Rybicki, G. B. and Lightman, A. P., 1979, Radiative Processes in Astrophysics (A Wiley-Interscience publication)

Schweizer, F. and Lasker, B. M., 1978, ApJ, 226, 167

Schweizer, F. and Middleditch, J., 1980, ApJ, 241, 1039

Sedov, L. I., 1959, Similarity and Dimensional Methods in Mechanics, 10th ed. (New York: Academic Press)

Serlemitsos, P. J., Jalota, L., Soong, Y., Kunieda, H., Tawara, Y., Tsusaka, Y., Suzuki, H., Sakima, Y., Yamazaki, T., Yoshioka, H., Furuzawa, A., Yamashita, K., Awaki, H., Itoh, M., Ogasaka, Y., Honda, H. and Uchibori, Y., 1995, PASJ, 47, 105

Sharov, A. S., 1964, Soviet Astronomy —A.J., 7, 698

Spitzer, L., 1962, Physics of Fully Ionized Gases (New York: Wiley Interscience)

Thompson, D. J., Bertsch, D. L., Dingus, B. L., Esposito, J. A., Etienne, A., Fichtel, C. E., Friedlander, D. P., Hartman, R. C., Hunter, S. D., Kendig, D. J., Mattox, J. R. ,McDonald, L. M., von Montigny, C., Mukherjee, R., Ramanamurthy, P. V., Sreekumar, P., Fierro, J. M., Lin, Y. C., Michelson, P. F., Nolan, P. L., Shriver, S. K., Willis, T. D., Kanbach, G., Mayer-Hasselwander, H.

A., Merck, M., Radecke, H. D, Kniffen, D. A. and Schneid, E. J., 1995, ApJS, 101, 259

Toor, A., 1980, AA, 85, 184

Tsunemi, H., Kitamoto, S., Manabe, M., Miyamoto, S. and Yamashita, K., 1989, PASJ, 41, 391

Turner, M. J. L., Thomas, h. D., Patchett, B. E., Reading, D. H., Makishima, K., Ohashi, T., Dotani, T., Hayashida, K., Inoue, H., Kondo, H., Koyama, K., Mitsuda, K., Ogawara, Y., Takano, S., Awaki, H., Tawara, Y. and Nakamura, N., 1989, PASJ, 41, 345

Vartanian, M. H., Lum, K. S. K. and Ku, W. H. -M, 1985, ApJ, 288, L5

Wang, Z. R., Asaoka, I., Hayakawa, S. and Koyama, K., 1992, PASJ, 44, 303

Willingale, R., West, R. G., Pye, J. P. and Stewart, G. C., 1996, MNRAS, 278, 749

Winkler, P. F. Jr, Hearn, D. R., Richardson, J. A. and Behnken, J. M., 1979, ApJ, 229, L123

Wu, C-C., Crenshaw, D. M., Fesen, R. A., Hamilton, A. J. S. and Sarazin, C. L., 1993, ApJ, 416, 247

Yamauchi, S., Kawai, N. and Aoki, T., 1994, PASJ, 46, L109

van Dishoeck, E. F., Jansen, D. J., and Phillips, T. G., 1993, AA, 279, 541

van den Bergh, S., 1976, ApJ, 208, L17